Master's thesis

2019

Abel Tenu Mekonnen

NTNU
Norwegian University of
Science and Technology
Faculty of Engineering
Department of Energy and Process Engineering

Abel Tenu Mekonnen

Modeling and numerical simulation of gas explosions for industrial safety analyses

June 2019

NTNU
Norwegian University of
Science and Technology

NTNU
Norwegian University of
Science and Technology

NTNU
Norwegian University of
Science and Technology

Modeling and numerical simulation of gas explosions for industrial safety analyses

Abel Tenu Mekonnen

Master of Science in Natural Gas Technology
Submission date: June 2019
Supervisor: Ivar Ståle Ertesvåg, EPT
Co-supervisor: Kjell Erik Rian, DNV GL - plant CFD solution AS

Norwegian University of Science and Technology
Department of Energy and Process Engineering

Master thesis work
Abel T. Mekonnen
spring 2019

Title:
Modeling and numerical simulation of gas explosions for industrial safety analyses

Project specification:

Background and objective

Mathematical modeling and numerical simulation of turbulent flow and combustion has for several decades been an important field of research at the Department of Energy and Process Engineering at NTNU. The methods and models developed through this activity are today used in industrial fire and explosion safety analyses all over the world.

A thorough understanding of the complex and coupled physical and chemical processes involved in gas explosions in realistic industrial environments is necessary to model and predict potential consequences of such events. DNV GL - CFD Solutions (formerly ComputIT) and the Department of Energy and Process Engineering at NTNU have for a long time cooperated on safety related R&D within turbulent flow and combustion. In the present project, we would like to study mathematical modeling and numerical simulation of industry relevant gas explosions.

The following tasks are to be considered:

- Perform a literature study on gas explosions with emphasis on governing mechanisms for flame acceleration and pressure build-up.
- Explore and make use of a CFD tool like KFX™-EXSIM for simulation of gas explosions in complex geometries.
- Select suitable cases in cooperation with supervisors. Perform numerical simulations of gas explosions, and discuss the results.
- Discuss potential improvements of the selected CFD tool with respect to mathematical modeling of gas explosions in industrial environments.

Address
N-7034 Trondheim
Norway

Location
K. Hejes vei 1b

Tel. +47 73 59 38 60
Fax +47 73 59 35 80
Org. no. NO 974 767 880

Abstract

Gas explosions occurring in chemical process industries, onshore and offshore modules of gas and oil industries, inside buildings, inside process equipment, can have catastrophic consequences such as loss of lives, property damage, environmental contamination, and so on. Consequently, achieving an acceptable level of safety regarding gas explosion related accidents is a major concern of all chemical process, and oil and gas industries. Gas explosion hazard assessment is therefore very important to prevent or reduce gas explosion accidents. Since reliable predictive computational tools are needed to provide consistent and accurate estimates of gas explosion hazard assessment using numerical simulations, this master thesis focused on the study and use of the computational fluid dynamics (CFD) tool `KFX-EXSIM` for modeling gas explosions in small to realistic geometries. In addition, the `XiFoam` solver of the `OpenFOAM` toolbox was also studied and used to simulate a small scale gas explosion with and without the presence of an obstacle. Three experiments of the gas explosion of stoichiometric hydrogen- and methane-air, and near stoichiometric natural gas-air mixtures in small, large vented, and realistic geometries were simulated for validation of both codes to experimental data.

Several simulations were performed for the three gas explosion experimental scenarios, and the main investigation of the experiments, such as peak overpressure, occurrence time of the peak overpressure, and flame speed were compared to results from both `KFX-EXSIM` and `XiFoam`.

For a small scale stoichiometric hydrogen-air explosion scenario, a reasonably good agreement between experiment and both `KFX-EXSIM` and `XiFoam` simulations was found in terms of the peak overpressure with an average error of 51 and 26%, respectively, for all configurations. Results of the simulations obtained from `XiFoam` show good agreement with the experimental results for flame speeds. The `XiFoam` simulations also show a good agreement with the experimental data with respect to the occurrence time of the peak overpressure. In `KFX-EXSIM`, the occurrence times of the predicated overpressures were delayed by more than 1.5 ms. As a result, it was concluded that the quasi-laminar combustion model used in the `KFX-EXSIM` explosion model gave a slow initial acceleration of flame.

For a large scale stoichiometric methane-air vented explosion experimental scenario, the numerical results obtained from the `KFX-EXSIM` simulation were in good agreement with the experimental data in terms of the first larger overpressure peak associated with both the Helmholtz oscillation and external pressure. However, the acoustically derived second larger overpressure peaks were completely damped by the simulations. Regarding the flame speed, the simulations show good agreement with the experimental data.

For the realistic scale near stoichiometric natural gas-air gas explosion scenarios, the simulations were in relatively good agreement with the experimental data in terms of peak overpressures. Most of the overpressure predictions fall within the band factor of 2.

The results from all simulations show that the `KFX-EXSIM` explosion model is capable of predicting the influence of the ignition point location, vent size, and different geometries. However, to increase the accuracy of the code, modifications on some of the values of the constant in the Porosity/Distributed Resistance (PDR) concept, and improvement in the quasi-laminar combustion model are recommended.

Acknowledgements

This master thesis was carried out at the Department of Energy and Process Engineering, at the Norwegian University of Science and Technology, NTNU, in cooperation with DNV GL - plant CFD solution (formerly computational Industry Technologies (ComputIT) AS).

I would first like to thank my supervisors, Ivar Ståle Ertesvåg and Kjell Erik Rian, for their immense support, mentoring and especially for giving me the opportunity to work on this thesis. I undertake this thesis with a little previous experience or knowledge of KFX-EXSIM and gas explosions, however through your guidance and patience I was able to pull through. I would also like to thank all the staffs at DNV GL - plant CFD solution for their support and advice.

Finally, I would like to express my deep appreciation to my wife and kids for offering me with unfailing support and continuous encouragement starting from the first year of study until the end. Without them, this achievement would not have been feasible. Thank you.

Trondheim, June 2019
Abel Tenu

Table of Contents

List of Figures

Nomenclature

Abbreviations

CFD Computational Fluid Dynamics

ComputIT Computational Industry Technologies AS

DNS Direct numerical simulation

EDC Eddy Dissipation Concept

EDM Eddy Dissipation Combustion Model

FVM Finite volume method

LES Large eddy simulation

OpenFOAM Open source Field Operation And Manipulation

PDR Porosity/Distributed Resistance

RANS Reynolds averaged Navier-stokes

SIMPLE Semi-Implicit Method for Pressure-Linked Equations

TDMA Tri-Diagonal Matrix Algorithm

Latin Symbols

A_f	Flame area	$[\mathrm{m}^2]$
A_i	Obstacle frontal area per unit volume	$[\mathrm{m}^{-1}]$
A_t	Model constant, =30	[-]
A_w	Obstacle wetted area per unit volume	$[\mathrm{m}^{-1}]$
A_{fx}	Surface area for fluid flow in x direction	$[\mathrm{m}^2]$
A_{sx}	Surface area of the obstacle in x direction	$[\mathrm{m}^2]$
c	Progress variable, Eq. (2.53)	[-]

C_μ	Constant in the $k-\varepsilon$ model, Eq. (2.33)	[-]
C_l	Dynamic rate modeling constant	[s^{-1}]
C_R	Drag coefficient of the single obstacle	[-]
$C_{\varepsilon 1}, C_{\varepsilon 2}$	Constants in the model equation for ε, Eq. (2.35)	[-]
D_h	Obstacle hydraulic diameter	[m]
D_{ie}	Damköhler number	[-]
E	Activation energy	[$\mathrm{J\,mol^{-1}}$]
E_l	Laminar reaction enhancement factor	[-]
E_t	Turbulence reaction enhancement factor	[-]
e_t	Total internal energy	[$\mathrm{J\,kg^{-1}}$=$\mathrm{m^2\,s^{-2}}$]
f	Mixture fraction	[-]
f_i	Friction factor	[-]
G	Turbulent generation rate term	[$\mathrm{kg\,m^{-1}\,s^{-3}}$]
G_R	Turbulent generation rate term from PDR formulation	[$\mathrm{kg\,m^{-1}\,s^{3}}$]
G_S	Turbulent generation rate term from shear stresses	[$\mathrm{kg\,m^{-1}\,s^{-3}}$]
h	Static specific enthalpy	[$\mathrm{J\,kg^{-1}}$ = $\mathrm{m^2\,s^{-2}}$]
h_t	Total specific enthalpy	[$\mathrm{J\,kg^{-1}}$ = $\mathrm{m^2\,s^{-2}}$]
$J_{h,j}$	Enthalpy diffusion flux	[$\mathrm{kg\,s^{-3}}$]
$J_{k,j}$	Mass diffusion of species Y_k in x_j direction	[$\mathrm{(kg)_k\,s^{-1}\,m^{-2}}$]
k	Turbulence kinetic energy	[$\mathrm{m^2\,s^{-2}}$]
L, ℓ	Characteristics length scale for turbulence	[m]
m	Mass of the fluid element	[kg]
p	Pressure	[$\mathrm{N\,m^{-2}}$]
Q	Heat produced due to external sources	[$\mathrm{W\,m^{-3}}$]
q_j	Heat flux per area in x_j direction	[$\mathrm{W\,m^{-2}}$]
R	Gas constant	[$\mathrm{J\,mol^{-1}\,K^{-1}}$]
R_k	Reaction rate of the chemical species k	[$\mathrm{(kg)_k\,m^{-3}\,s^{-1}}$]
S_L	Laminar flame speed	[$\mathrm{m\,s^{-1}}$]

T	Absolute temperature	[K]
u_i	Velocity component in x_i direction	$[\mathrm{m\,s^{-1}}]$
V_f	Volume available for fluid flow	$[\mathrm{m^3}]$
V_s	Volume occupied by the obstacle	$[\mathrm{m^3}]$
Y_k	Mass fraction of species k	$[(\mathrm{kg})_\mathrm{k}\,\mathrm{kg^{-1}}]$
Y_{lim}	= $\min[Y_{fu}, Y_{air}/r, Y_{fu,b}]$; Limiting mass fraction	[-]
Greek Symbols		
β_a	Area occupied by the obstacle	[-]
β_v	Volume fraction occupied by the obstacle	[-]
β_x	Area porosity occupied by the obstacle in the x direction	[-]
δ_{ij}	Kronecker function, = 1 if i = j and = 0 if i $\neq$ j	[-]
λ	The second viscosity coefficient	$[\mathrm{N\,s\,m^{-2}}]$
μ	Dynamic viscosity	$[\mathrm{N\,s\,m^{-2}}]$
μ_B	Bulk viscosity	$[\mathrm{N\,s\,m^{-2}}]$
μ_{eff}	Effective viscosity	$[\mathrm{N\,s\,m^{-2}}]$
ν	=μ/ρ; Kinematic viscosity	$[\mathrm{m^2\,s^{-1}}]$
ϕ	Equivalence ratio	[-]
ϕ	General flow property	
ρ	Density	$[\mathrm{kg\,m^{-3}}]$
σ_ε	Turbulence Prandtl/Schmidt number for dissipation ε	[-]
σ_h	Effective Prandtl number	[-]
σ_k	Turbulence Prandtl/Schmidt number for turbulence energy k	[-]
σ_{ij}	Turbulence stress tensor	$[\mathrm{N\,m^{-2}}]$
σ_{Yk}	Effective Schmidt number	[-]
τ_L	=$\nu/(S_L)^2$; chemical timescale of the laminar flame, Eq. (2.41)	[s]
τ_{ch}	Chemical time scale	[s]
τ_e	Turbulent eddy mixing time scale	[s]
τ_{ij}	Viscous stress tensor	$[\mathrm{N\,m^{-2}}]$

θ	Kolmogorov micro length scale	$[\mathrm{m}]$
ε	Dissipation rate of turbulence energy	$[\mathrm{m^2\,s^{-3}}]$
Ξ	Subgrid flame wrinkling	[-]
ξ	Conserved variable	[-]
ξ_0	Value of ξ at fuel rich reference point	[-]
ξ_∞	Value of ξ at oxidant rich reference point	[-]

Superscripts

$'$, $''$	Characteristic scale for turbulence
$-$	mean value
$\cdot$	time derivative
$\sim$	mass-weighted average

Subscripts

b	Burned
eff	Effective
fu	Fuel
l	laminar
pr	Product
t	Turbulence
u	Unburned

Other Symbols

ℓ_L	$=\nu/S_L$; laminar flame thickness, Eq. (2.41)	$[\mathrm{m}]$
$\mathcal{D}$	Diffusion coefficient	$[\mathrm{m^2\,s^{-1}}]$
$\mathcal{K}$	Thermal conductivity coefficient	$[\mathrm{W\,m^{-1}\,K^{-1}}]$
$\mathcal{R}_i$	Additional flow resistance due to the obstacle in the x_i direction	$[\mathrm{kg\,m^{-2}\,s^{-2}}]$
$\mathfrak{R}$	Flame propagation radius	$[\mathrm{m}]$
$f_{k,i}$	Body force acting on species k in x_i direction	$[\mathrm{m\,s^{-2}}]$

Chapter 1

Introduction

An accidental release of flammable gases can easily occur in most gas and oil and chemical process industries. If these gases are mixed with air and form a premixed gas cloud and ignite by some ignition source, a gas explosion can occur which can cause several damages to human beings and properties. However, the strength of the gas explosions varies depending on the geometry layout and congestion, the type and stoichiometry of the fuel-air mixture. The level of the gas explosion pressures is highly dependent on the level of the turbulence of the flow in addition to the fuel-air mixture type and stoichiometry. The turbulence can be produced due to the presence of obstacles in the direction of the flame propagation path, Rayleigh-Taylor instability, and buoyancy. However, the effect of the Rayleigh-Taylor instability and buoyancy on turbulence generation is less compared to the presence of obstacles in the explosion flow path [1]. The degree of flame acceleration and pressure load depends on several parameters such as the level of the confinement, the position, and size of the obstacle, vent position and size, fuel type, and so on. The effect of the obstacles on flame acceleration and pressure load in the gas explosions has been studied experimentally by various workers [1–6]. According to their work, the ignition of ”accidental” gas releases in the congested regions shows the distortions and turbulence generation in the upstream flow due to the interaction of the unburnt gas with an obstacle that leads to an increase in the flame surface area. It, therefore, increases the rate of combustion and can result in disastrous gas explosions pressures.

1.1 Motivation

Obtaining an acceptable level of safety regarding gas explosion is a major concern of all chemical, gas, and oil industries. Gas explosion hazard assessment is therefore very important to prevent or reduce accidents related to gas explosions. This assessment can be performed either experimentally or using numerical simulations. The later can be much faster and cheaper than the former, and in the numerical simulation of a gas explosion, it is also possible to easily change the input parameters. However, to perform a numerical simulation of gas explosions a reliable predictive computational tool is needed. To be confident of this tool, it is necessary to validate the predictions against experiments. Some known advanced computational fluid dynamics (CFD) based gas explosion simulation tools that are being used in the industries and research institutions were available since the 1980s. Among those, `KFX-EXSIM` is one of the industrial CFD technology in the oil and gas industries. There are also open source solvers used to simulate gas explosions numerically, e.g. `XiFoam`, which is a part of `OpenFOAM`. Both

CFD tools, i.e KFX-EXSIM and XiFoam, were used in this project to numerically reproduce gas explosion experiments.

KFX-EXSIM is an integration of the industrial fire simulation code KAMELEON FIREEX (KFX) [7,8] and the industrial explosion simulation code EXPLOSION SIMULATOR (EXSIM) [9–11]. It is a finite-volume CFD code with Porosity/Distributed Resistance (PDR) concept, see Section 3.2. The Eddy Dissipation Combustion Model (EDM), see Section 2.3.5, and an extended version of the $k - \varepsilon$ turbulence model, see Section 3.4, are used to represent the combustion and turbulence, respectively. The initial laminar flame propagation is modeled using a Van Den Berg quasi-laminar combustion model, see Section 3.5.1.

XiFoam is a solver for the premixed and partial premixed combustion with turbulence modeling. It is a part of OpenFOAM (open source Field Operation And Manipulation) toolbox, which is a free open source software package used to resolve CFD problems using Finite-volume discretization. Combustion and turbulence are modeled with the flame wrinkling combustion model using a reaction progress variable, see Section 2.3.4, and the standard $k - \varepsilon$ turbulence model, see Section 2.2.5, respectively. The "power law" formula with the empirical expression proposed by Gülder, see Section 2.3.1, is used to model the laminar flame speed.

1.2 Objective of the thesis

The aims of this thesis are literature study on gas explosions with emphasis on governing mechanisms for flame acceleration and pressure build-up, the study on the underlying mathematical modeling implemented in the CFD tool KFX-EXSIM and XiFoam for simulating gas explosions in complex geometries, and numerical simulations of gas explosions using both CFD codes mentioned above. For the latter task, three gas explosion experiments were reproduced numerically using KFX-EXSIM and XiFoam (used only for small scale explosion scenario). These are:

- A premixed hydrogen-air explosion in a small-scale vertical rectangular tube: effect of obstacle position on overpressure [12],
- Effect of ignition position and vent size on overpressure and flame speed: large scale premixed methane-air explosion [13], and
- A premixed natural gas-air explosion in a test rig representing an offshore process module at a realistic scale [14]

All the XiFoam simulations were performed in parallel on a distributed processor on a supercomputer called 'Vilje' using a total of 64 processors.

1.3 Outline of the report

The thesis report is structured as follows:

Chapter 2 describes the general conservation equations needed for the reacting turbulent flows and gives an overview of the turbulent and combustion models. Introduction about a gas explosion and the mechanism of flame propagation and pressure build-up due to the presence of

obstacles are also discussed here.
Chapter 3 describes the underlying mathematical modeling implemented in the KFX-EXSIM code to modeling gas explosions in complex geometries.
Chapter 4 gives a brief overview of the small scale gas explosion experimental scenario and the simulation setup used in both KFX-EXSIM and XiFoam to numerically reproduce the experiment mentioned earlier, which includes the generation of the geometry and mesh of the computational domain, defining initial and boundary conditions. The numerical results obtained from both codes and brief discussions on the results are also present in this chapter.
Chapter 5 presents both experimental and numerical procedure descriptions for the large scale vented gas explosion scenario. The numerical results and discussions on the results also present here.
Chapter 6 provides the realistic scale gas explosion case descriptions and the numerical setup used in KFX-EXSIM to reproduced the experiment numerically. In addition, the numerical results obtained from various simulation and discussion are presents.
Finally, Chapter 7 conclude the findings of the thesis.

Chapter 2

Theoretical formulation

2.1 Conservation equations for reacting flows

The conservation of mass, momentum, energy, and individual species concentration are the fundamental principles that describe the dynamic and thermodynamic behavior of chemically reacting flows. These principles are mathematically represented by equations for the conservation of mass, momentum, energy, and species mass fraction. The brief overview of these equations can be found in the following subsections.

2.1.1 Continuity equation

The total mass conservation equation is the same in reacting and non-reacting flow, since reactions do not generate or consume mass - mass is always preserved. The total mass conservation equation, also called continuity equation, in partial differential form in Cartesian tensor notation, for single-phase flow, can be written as [15, p. 55]

$$\frac{\partial \rho}{\partial t} + \frac{\partial}{\partial x_i}(\rho u_i) = 0 \ . \tag{2.1}$$

where ρ is the total mass density, and u_i is the mean mass velocity component in the x_i direction.

2.1.2 Momentum equation

Newton's second law is applied to derive the equation of the conservation of momentum. Momentum is defined as the product of the mass and velocity of an object. For a closed system, momentum is also conserved. However, it changes due to the effect of forces as Newton's second law stated that force is equal to the change in momentum per change in time. The momentum equation is the same in reacting and non-reacting flows and can be defined as follows [16, p. 13]

$$\frac{\partial}{\partial t}(\rho u_i) + \frac{\partial}{\partial x_j}(\rho u_i u_j) = -\frac{\partial p}{\partial x_i} + \frac{\partial \tau_{ij}}{\partial x_j} + \rho \underbrace{\sum_{k=1}^{N} Y_k f_{k,i}}_{=f_i} \ , \tag{2.2}$$

where p is pressure (surface force), τ_{ij} is the viscous stress tensor, $f_{k,i}$ is the body force (e.g., gravitation) acting on species k in the x_i direction, Y_k is the mass fraction of species k, and N is the number of species in the reacting mixture.

The first and second term on the left-hand side of Eq. (2.2), respectively, are the time rate of momentum increment (per unit volume) within the control volume and the rate of momentum lost by convection per unit volume through the control surface. While on the right-hand side of Eq. (2.2) the first and second terms are the surface forces per unit volume (pressure and viscous stress, respectively), the third term is the acceleration of the reacting mixture due to the body force $f_{k,i}$ acting on species k.

For Newtonian fluids, the viscous stress tensor τ_{ij} is proportional to the time rate of strain (i.e. velocity gradients) [17]:

$$\tau_{ij} = \mu\left(\frac{\partial u_i}{\partial x_j} + \frac{\partial u_j}{\partial x_i}\right) + \underbrace{(\mu_B - \frac{2}{3}\mu)}_{=\lambda}\frac{\partial u_k}{\partial x_k}\delta_{ij} \ , \tag{2.3}$$

where the quantity δ_{ij} is called the Kronecker function which has a value of 1 and 0, when i=j and i$\neq$ j, respectively, λ is called the second viscosity coefficient, μ_B is the bulk viscosity, and μ is the dynamic viscosity coefficient. The Stokes' hypothesis gives $\lambda = -\frac{2}{3}\mu$, or $\mu_B = 0$.

2.1.3 Energy equation

The energy equation is derived on the basis of the first law of thermodynamics, which stated that the change in energy in the system is equal to the difference between the heat added to the system and the amount of work done by the system on its surroundings. By applying this law to a fluid element moving through an infinitesimally small control volume fixed in space, the conservation for total energy can be expressed as follows [18, p. 206]:

$$\frac{\partial}{\partial t}(\rho e_t) + \frac{\partial}{\partial x_j}(\rho e_t u_j) = -\frac{\partial q_j}{\partial x_j} + \dot{Q} - \frac{\partial}{\partial x_j}(p u_j) + \frac{\partial}{\partial x_j}(\tau_{ij} u_i) + \rho \sum_{k=1}^{N} Y_k f_{k,i}(u_i + V_{k,i}) \ . \tag{2.4}$$

Where e_t is the total energy which is the sum of internal energy and kinetic energy

$$e_t = e + \frac{1}{2}u_i u_i \ , \tag{2.5}$$

$\dot{Q}$ is the rate of heat produced due to external sources. The heat flux q_i can be expressed as

$$q_j = -\mathcal{K}\frac{\partial T}{\partial x_j} + \rho \sum_{k=1}^{N} h_k Y_k V_{k,i} \ , \tag{2.6}$$

where $\mathcal{K}$ is the thermal conductivity coefficient, T is the temperature, and h_k is the enthalpy of the species k. The first term on the right-hand side of Eq. (2.6) represents the heat diffusion term defined by Fourier's law, while the second term corresponding to the diffusion of species with different enthalpies. In addition, there is a heat flux associated with the heat transfer due to concentration gradients, known as Dufour effect. However, it has a small influence on the combustion process and is neglected in the combustion processes [19].

The conservation equation for the total enthalpy can be obtained by adding $\frac{\partial p}{\partial t} + \frac{\partial}{\partial x_j}(p u_j)$ to Eq. (2.4) on both side. It can be written as [18, p. 206]

$$\frac{\partial}{\partial t}(\rho h_t) + \frac{\partial}{\partial x_j}(\rho h_t u_j) = \frac{\partial p}{\partial t} - \frac{\partial q_j}{\partial x_j} + \frac{\partial}{\partial x_j}(\tau_{ij} u_i) + \dot{Q} + \rho \sum_{k=1}^{N} Y_k f_{k,i}(u_i + V_{k,i}) \ , \tag{2.7}$$

where h_t is the total specific enthalpy and can be defined as $h_t = e_t + p/\rho$. All other variables in Eq. (2.7) are the same as in Eq. (2.4). An equation for mechanical energy, $\frac{1}{2}u_i u_i$, can be found by multiplying the momentum equation, Eq. (2.2), with u_i, and can be written as [18, p. 205]

$$\frac{\partial}{\partial t}(\rho\frac{1}{2}u_i u_i) + \frac{\partial}{\partial x_j}(\rho\frac{1}{2}u_i u_i u_j) = -u_i\frac{\partial p}{\partial x_i} + u_i\frac{\partial \tau_{ij}}{\partial x_j} + \rho\sum_{k=1}^{N} Y_k f_{k,i} u_i \ . \tag{2.8}$$

The conservation equation for static enthalpy, h, can be obtained by subtracting mechanical energy equation, Eq. (2.8), from the equation for the total enthalpy, Eq. (2.7), and can be written as [18, p. 206]

$$\rho\frac{Dh}{Dt} = \frac{Dp}{Dt} - \frac{\partial q_j}{\partial x_j} + \tau_{ij}\frac{\partial u_i}{\partial x_j} + \dot{Q} + \sum_{k=1}^{N} Y_k f_{k,i} V_{k,i} \ , \tag{2.9}$$

where

$$\rho\frac{Dh}{Dt} = \frac{\partial}{\partial t}(\rho h) + \frac{\partial}{\partial x_j}(\rho u_j h) \ , \tag{2.10}$$

$$\frac{Dp}{Dt} = \frac{\partial p}{\partial t} + u_i\frac{\partial p}{\partial x_i} \ , \tag{2.11}$$

and $\phi = \tau_{ij}\frac{\partial u_i}{\partial x_j}$ represents the viscous heating source term.

2.1.4 Chemical species conservation equation

In reacting flows, each individual species is produced or consumed at a certain rate, varying the mass balance for each, though the total mass of the reacting mixture is always conserved. For a mixture of N species, the equation of chemical species conservation can be written as follows [18, p. 200]

$$\frac{\partial}{\partial t}(\rho Y_k) + \frac{\partial}{\partial x_j}(\rho Y_k u_j) = \frac{\partial(-J_{k,j})}{\partial x_j} + R_k \ , k = 1, ..., N, \tag{2.12}$$

where Y_k is the mass fraction of species k, $J_{k,j}$ represents the mass flux of species k in x_j direction, and R_k is the reaction rate. The mass flux $J_{k,j}$ mainly associated with the mass diffusion due to the concentration gradient, obtained using Fick's law, Eq. (2.13). Additionally, the mass flux also associated with the mass diffusion caused by the temperature gradient, known as thermal diffusion or Soret effect, and the mass diffusion due to a pressure gradient. However, in the most simulation of the combustion process, the Soret effect and the pressure diffusion are neglected [19].

Neglecting the Soret effect and the pressure diffusion, the mass flux $J_{k,j}$ can be expressed using Fick's law [18, p. 200]

$$-J_{k,j} = -\rho\mathcal{D}_k\frac{\partial Y_k}{\partial x_j} \ , \tag{2.13}$$

where $\mathcal{D}_k$ is the diffusion coefficient of species k. By inserting Eq. (2.13) into Eq. (2.12), the equation of species conservation can be written as follows:

$$\frac{\partial}{\partial t}(\rho Y_k) + \frac{\partial}{\partial x_j}(\rho Y_k u_j) = \frac{\partial}{\partial x_j}(\rho\mathcal{D}_k\frac{\partial Y_k}{\partial x_j}) + R_k \ , k = 1, ..., N, \tag{2.14}$$

2.2 Turbulent Flows

The turbulent flow is the most encountered flow behavior in most practical engineering devices that involve flowing fluid and is mainly true for combustion devices [20]. Turbulent flow is a random and chaotic flow phenomenon that occurs when viscous forces are unable to sufficiently dampen the instabilities in a flow. Turbulence flows are characterized by random velocity fluctuation, which can generate fluctuations in scalar quantities such as density, temperature, and mixture composition. This random velocity and then scalar quantities are an effect of the presence of eddies of different strength and dimensions that are produced by shear within the flow. The dimensionless parameter, Reynolds number $Re = \rho u l/\mu$, defined as the ratio of inertial force to viscous forces, can be used to categorize different flow regimes. Here, ρ is the density of the fluid, u represents the characteristic velocity, l is the characteristic length, and μ is the dynamic viscosity of the fluid. For a low Reynolds number (i.e the viscous force is sufficiently larger than the inertial force), the viscous force is strong enough to damp the instabilities in a flow, so the flow regime is a laminar flow. While, for a sufficiently high Reynolds number (above critical Reynolds number, Re_{crit}), the flow regime/behavior changes from laminar to turbulent flow. For turbulent flow, solving the governing equations using computational fluid dynamics (CFD) can be done using three levels of computations:

- Reynolds averaged Navier-Stokes (RANS): all the dependent variables in the governing equations will decompose into a mean value (averaged) and a fluctuating component, and then solve for the mean values. The Reynolds averaged equations are derived by decomposing the dependent variables in the governing equations into a steady time-mean value and a fluctuating component and then time averaging the entire equation. There are two kinds of averaging, the classical Reynolds averaging (time averaging, see Section 2.2.2) and Favre averaging (mass-weighted averaging, see Section 2.2.3). The two averaging techniques become the same for flows with constant density. The averaged version of the conservation equations contain additional terms, for example, Reynolds stresses in Eq. (2.24). Therefore, a turbulent model is needed to model the additional terms in the averaged equations in order to get a closed system of mean (averaged) equations. The overview of the turbulence models is presented in Section 2.2.5.

- Large-eddy simulation (LES): the balance equation for large eddy simulations are obtained by low-pass filtering of the Navier-Stokes equations, which the larger eddies are allowed to pass and the smaller eddies are rejected. The effect of the mean flow and the large eddies are resolved, while the effect of the small eddies are modeled using sub-grid scale model.

- Direct numerical simulation (DNS): the full equation of motions are computed directly without the use of any model of the turbulent motions. The Navier-stokes equations are computed using a sufficiently fine grid that they can resolve the smallest eddies. It is also required a sufficiently small time step to resolve the period of fastest fluctuations.

The Large-eddy simulation (LES) and Direct numerical simulation (DNS) are very expensive and time demanding in terms of computing resources. In this project, the turbulence flow computations had been done using the Reynolds averaged Navier-Stokes (RANS) equations in both the CFD tools, `KFX-EXSIM` and `XiFoam`.

2.2.1 Characteristic scales of turbulent flows

Turbulent flows can be characterized by the presence of eddies over a wide range of length and time scales. The largest eddies in the flow are corresponding to the largest length scales, known as integral length scales L. The maximum length of these scales is set by the dimension of the apparatus. For example, In the pipe flow, the maximum integral length scale would be equal to the pipe diameter. Eddies at the integral length scale are called the energy production eddies which contain most of the turbulent kinetic energy, which obtains from the mean flow. They also account for most of the transport of momentum and energy. The kinetic energy contained in the eddies of the integral scale is continuously transferred to smaller and smaller eddies until it reaches the smallest eddies in the flow. These smallest eddies are corresponding to the minimum length scale in the flow, is known as the Kolmogorov microscales η. In this length scale, the effect of viscosity becomes more important and the kinetic energy is dissipated by viscosity into thermal energy. According to energy conservation, the overall kinetic energy production rate must be equals to the dissipation rate of kinetic energy in the smallest eddies. Thus, based on the dissipation rate ε and the characteristic kinematic viscosity ν the Kolmogorov length, time, and velocity are formed as [21]

$$\eta \approx \left(\frac{\nu^3}{\varepsilon}\right)^{1/4}, \qquad \tau_\eta \approx \left(\frac{\nu}{\varepsilon}\right)^{1/2}, \qquad u_\eta \approx \left(\nu\varepsilon\right)^{1/4}. \tag{2.15}$$

The dissipation rate ε in terms of the large scale flow can be defined as [21, p. 481]

$$\varepsilon \approx \frac{u'_L u'_L}{L/u'_L} \approx \frac{{u'_L}^3}{L}, \tag{2.16}$$

where u'_L is the characteristic fluctuation velocity in the integral length scale L.
Inserting the definition of ε, Eq. (2.16), into Eq. (2.15), the Kolmogorov length scale can be written as

$$\eta \approx \left(\frac{\nu^3 L}{u'_L}\right)^{1/4}. \tag{2.17}$$

The Kolmogorov length scale is related to the integral length scale through the ratio of the largest to smallest length scales in the flow:

$$\frac{L}{\eta} \approx \left(\frac{u'_L L}{\nu}\right)^{3/4} \approx Re_L^{3/4}, \tag{2.18}$$

where Re_L is the Reynolds number based on the integral length scale. Eq. (2.18) shows that as the Reynolds number increased the separation between the integral and Kolmogorov scales also increases.

There are many other length scales encountered in the turbulence flow. For example, Taylor scale, λ, is an intermediate length scale between the integral and Kolmogorov length scales.

2.2.2 Reynolds-decomposition and averaging

Reynolds decomposes a quantity ϕ into a mean value, $\overline{\phi}$, and a fluctuation, ϕ:

$$\phi(t) = \overline{\phi} + \phi'(t), \tag{2.19}$$

where the mean value of fluctuation is zero, i.e $\overline{\phi'}(t) = 0$.

The mean values can be defined as a time average of ϕ as follows [18, p. 34]

$$\overline{\phi}(t) = \frac{1}{\Delta t} \int_{t-\frac{1}{2}\Delta t}^{t+\frac{1}{2}\Delta t} \phi(t) dt \,, \tag{2.20}$$

where Δt is the average time interval which is required to be large enough compared to a random fluctuation period, but small enough in respect of the time constant for any slow variations in the flow field related to ordinary unsteady flows [10, 22, p. 272].

2.2.3 Favre-decomposition and averaging

In combustion, where the density is varied, to simplified the averaging procedure, the mass-weighted averaging (Favre-averaging) is used to certain variables in the conservation equations described in Section 2.1 [17]. Favre divides the quantity ϕ into a mean value, $\tilde{\phi}$, and a fluctuation, ϕ'', and can be written as

$$\phi = \tilde{\phi} + \phi'' \,, \tag{2.21}$$

where

$$\tilde{\phi} = \frac{\overline{\rho\phi}}{\bar{\rho}} \,. \tag{2.22}$$

The mass-weighted averaged value of fluctuations in Eq. (2.21) is zero, $\overline{\rho\phi''} = 0$, while they have non-zero mean value, $\overline{\phi''} \neq 0$. The mean quantities $\overline{\phi}$ and $\tilde{\phi}$ in Eq. (2.19) and Eq. (2.22) are the Reynolds and Favre averaged quantity ϕ, respectively.

2.2.4 Favre-Averaged equations

Introducing the Reynolds averaging procedure to density and pressure, and Favre averaging to the remaining flow variables in the conservation equations yielding the Favre-averaged equations. By introducing the Favre and Reynolds averaging into the continuity equation, Eq. (2.1), the Favre-averaged equation for the conservation of mass can be written as [22, p. 274]

$$\frac{\partial \bar{\rho}}{\partial t} + \frac{\partial}{\partial x_i}\left(\bar{\rho}\tilde{u}_i\right) = 0 \,. \tag{2.23}$$

Similarly, by applying the Favre- and Reynolds- averaging procedure for the momentum equation, Eq. (2.2), the Favre-averaged equation for conservation of momentum can be written as [22, p. 275]

$$\frac{\partial}{\partial t}(\bar{\rho}\tilde{u}_i) + \frac{\partial}{\partial x_j}(\bar{\rho}\tilde{u}_i\tilde{u}_j) = -\frac{\partial \bar{p}}{\partial x_i} + \frac{\partial}{\partial x_j}(\bar{\tau}_{ij} - \overline{\rho u_i'' u_j''}) + \overline{\rho f_i} \,, \tag{2.24}$$

where neglecting viscosity fluctuations, $\bar{\tau}_{ij}$ can be expressed as [22, p. 275]

$$\bar{\tau}_{ij} = \underbrace{\mu\left[\left(\frac{\partial \tilde{u}_i}{\partial x_j} + \frac{\partial \tilde{u}_j}{\partial x_i}\right) - \frac{2}{3}\delta_{ij}\frac{\partial \tilde{u}_k}{\partial x_k}\right]}_{(I)} + \underbrace{\mu\left[\left(\frac{\partial \overline{u_i''}}{\partial x_j} + \frac{\partial \overline{u_j''}}{\partial x_i}\right) - \frac{2}{3}\delta_{ij}\frac{\partial \overline{u_k''}}{\partial x_k}\right]}_{(II)} \,. \tag{2.25}$$

In the most practical scenarios, the second term on the right-hand side of Eq. (2.25), (II), is much smaller than -$\overline{\rho u_i'' u_j''}$, and is most probable to be neglected [22]. The new term in Eq. (2.24), $\overline{\rho u_i'' u_j''}$, is the mass-weighted Reynolds stresses or Favre stresses, and it can be written $\overline{\rho u_i'' u_j''} = \bar{\rho}\widetilde{u_i'' u_j''}$. On the right-hand side of Eq. (2.24), the last term can be expressed as $\overline{\rho f_i} = \bar{\rho} f_i$.

The Favre-averaged equation of conservation of enthalpy can be expressed as follows [16, p. 164]

$$\frac{\partial}{\partial t}(\overline{\rho}\tilde{h}) + \frac{\partial}{\partial x_j}(\overline{\rho}\tilde{h}\tilde{u}_j) = \frac{\overline{Dp}}{Dt} + \frac{\partial}{\partial x_j}\left(\overline{\rho}\overline{\mathcal{D}_k}\frac{\partial \tilde{h}}{\partial x_j} - \overline{\rho}\widetilde{u_j'' h''}\right) + \overline{\dot{Q}} + \overline{S}_h \,, \tag{2.26}$$

where

$$\frac{\overline{Dp}}{Dt} = \frac{\partial \overline{p}}{\partial t} + \overline{u_j \frac{\partial p}{\partial x_j}} \,. \tag{2.27}$$

In Eq. (2.26), S_h is the source term, which accounted for the losses due to friction in the fluid inside the control volume, chemical and potential energy, $\overline{\rho}\widetilde{u_j'' h''}$ is the unresolved enthalpy fluxes, and Q is the heat produced due to external sources. The second term in the right-hand side of Eq. (2.27) is approximated as $\tilde{u_j}(\partial\overline{p}/\partial x_j)$ in most RANS codes [16].

The Favre-averaged equation for chemical species conservation (equation for the mass fraction of a chemical species k) can be obtained by applying the Favre- and Reynolds procedure to Eq. (2.14). After rearranging, it can be expressed as

$$\frac{\partial}{\partial t}(\overline{\rho}\tilde{Y_k}) + \frac{\partial}{\partial x_j}(\overline{\rho}\tilde{u_j}\tilde{Y_k}) = \frac{\partial}{\partial x_j}\left(\overline{\rho}\overline{\mathcal{D}_k}\frac{\partial \tilde{Y_k}}{\partial x_j}\right) - \frac{\partial}{\partial x_j}(\overline{\rho}\widetilde{u_j'' Y_k''}) + \overline{R}_k \,, \tag{2.28}$$

where R_k is the rate of production or consumption of the chemical species k either by chemical reaction or by another mechanism inside the control volume.

The mass-weighted Reynolds stresses $\overline{\rho}\widetilde{u_i'' u_j''}$ in Eq. (2.24), the unresolved enthalpy fluxes $\overline{\rho}\widetilde{u_j'' h''}$ in Eq. (2.26), and species fluxes $\overline{\rho}\widetilde{u_j'' Y_k''}$ in Eq. (2.28) are unknown. These quantities must be supplied or modeled in order to close the Favre-averaged equations. Hence, turbulence models are needed. The overview of the turbulence models is present in the next subsection.

2.2.5 Turbulence Models

The use of turbulence models are very necessary to model the Reynolds stresses and the unresolved enthalpy and species turbulent fluxes to close the system of the Favre equations and, to able to compute turbulent flows using the RANS equations. The turbulent species and enthalpy fluxes can be closed using a gradient-diffusion hypothesis:

$$\overline{\rho}\widetilde{u_j'' Y_k''} = -\frac{\mu_t}{Sc_{tk}}\frac{\partial \tilde{Y_k}}{\partial x_j} \,, \tag{2.29}$$

and

$$\overline{\rho}\widetilde{u_j'' h''} = -\frac{\mu_t}{Pr_t}\frac{\partial \tilde{h}}{\partial x_j} \,, \tag{2.30}$$

respectively. Where μ_t is the turbulent viscosity, Sc_{tk} is the turbulent Schmidt number for species k, and Pr_t is the turbulent Prandtl number.

According to the Boussinesq hypothesis, the turbulent Reynolds stresses, $\overline{\rho}\widetilde{u_i''u_j''}$, can be expressed as [16, p. 143]

$$\overline{\rho u_i'' u_j''} = \overline{\rho}\widetilde{u_i''u_j''} = -\mu_t\left(\frac{\partial \tilde{u}_i}{\partial x_j} + \frac{\partial \tilde{u}_j}{\partial x_i} - \frac{2}{3}\delta_{ij}\frac{\partial \tilde{u}_l}{x_l}\right) + \frac{2}{3}\overline{\rho}k \ , \tag{2.31}$$

where k is the turbulence kinetic energy. The mean turbulence kinetic energy in three coordinate directions can be expressed as:

$$k = \frac{1}{2}\sum_{i=1}^{3}\widetilde{u_i''u_i''} = \frac{1}{2}(\widetilde{u_1''^2} + \widetilde{u_2''^2} + \widetilde{u_3''^3}) \ . \tag{2.32}$$

The turbulent viscosity, μ_t, in the Equations (2.29)–(2.31) is estimated using the turbulence model. This can be done using different approaches, for example:

- Zero-equation model, for example, Prandtl mixing length model: In this model, no additional transport equation is needed. The stresses are described using a simple algebraic relation for the turbulence or eddy viscosity as a function of position, which required the field of mixing length.
- One-equation model, for example, Spalart-Allmaras turbulence model: Here, the transport equation for the Spalart-Allmaras variable, is also known as a viscosity-like variable, is needed to be solved alongside the RANS equations. The turbulent viscosity is then calculated using the value of the viscosity-like variable.
- Two-equation model: the $k-\varepsilon$ is the most popular two-equation turbulence model, which two transport equations, one for the turbulence energy k and one for the dissipation of the turbulence energy ε, are solved together with the RANS equations. The turbulence length scale is calculated using the value of k and ε.

The standard k - ε Model

In this turbulence model, the turbulence viscosity, μ_t, can be expressed using the turbulence velocity, $u_t = (2/3k)^{1/2}$, length scale, l, as [23]

$$\mu_t = \overline{\rho}u_t l = C_\mu \overline{\rho}\frac{k^2}{\varepsilon} \ , \tag{2.33}$$

where the turbulence energy, k, and the dissipation of the turbulence energy, ε, can be expressed as follows

$$\frac{\partial}{\partial t}(\overline{\rho}k) + \frac{\partial}{\partial x_j}(\overline{\rho}\tilde{u}_j k) = \frac{\partial}{\partial x_j}\left[\left(\mu + \frac{\mu_t}{\sigma_k}\right)\frac{\partial k}{\partial x_j}\right] + P_k - \overline{\rho}\varepsilon \ , \tag{2.34}$$

and,

$$\frac{\partial}{\partial t}(\overline{\rho}\varepsilon) + \frac{\partial}{\partial x_j}(\overline{\rho}\tilde{u}_j \varepsilon) = \frac{\partial}{\partial x_j}\left[\left(\mu + \frac{\mu_t}{\sigma_\varepsilon}\right)\frac{\partial \varepsilon}{\partial x_j}\right] + C_{\varepsilon 1}\frac{\varepsilon}{k}P_k - C_{\varepsilon 2}\overline{\rho}\frac{\varepsilon^2}{k} \ , \tag{2.35}$$

respectively, where σ_k is the turbulent Prandtl numbers for k and σ_ε is the Prandtl numbers for ε. The source term, P_k, can be expressed as

$$P_k = -\overline{\rho}\widetilde{u_i''u_j''}\frac{\partial \tilde{u}_i}{\partial x_j} \ , \tag{2.36}$$

where the Reynolds stresses, $\overline{\rho}\widetilde{u_i'' u_j''}$, can be determined using the Boussinesq approximation, Eq. (2.31).

The standard values for the model constants are [24]:

$$C_\mu = 0.09; \quad C_\varepsilon 1 = 1.44; \quad C_\varepsilon 2 = 1.92; \quad \sigma_k = 1.0; \quad \sigma_\varepsilon = 1.3 \ . \tag{2.37}$$

The $k-\varepsilon$ model also provides some turbulence characteristics scales estimates, such as integral time scale ($\tau = k/\varepsilon$), integral length scale ($L = k^{2/3}/\varepsilon$), and velocity scale (length divided by time, = $k^{1/2}$).

2.3 Combustion

Combustion is a highly exothermic redox reaction between a fuel and an oxidizer (in most cases atmospheric oxygen). As the definition indicates, energy is released in the combustion process, usually in the form of heat, but also in the form of light or both light and heat. In order to combustion to take place three necessary requirements must be fulfilled: i) mixing of the reactant at the molecular level, ii) sufficiently high temperature, and iii) sufficient time for the reactant to react. The combustion of a gaseous fuel can occur in two different modes [20, 25]: If the reactants are perfectly mixed at the molecular level before the occurrence of the chemical reaction, the flames are categorized as premixed flames. While, when the reactants are supplied separately, and mixing and reaction both take place in the flame, non-premixed (diffusion) flames result. Based on the fluid flow regimes, whether laminar or turbulent, each of the flames types further subdivided into laminar premixed flames, turbulent premixed flames, laminar non-premixed flames, and turbulent non-premixed flames. A gas explosion is one of the examples of the premixed combustion which involves turbulent flame propagation. In order to study turbulent premixed flame, it is necessary to understand the laminar premixed flame theories. In this section, the essential characteristics quantities of both laminar and turbulent premixed flames are discussed.

2.3.1 Laminar premixed flames

In laminar premixed flames, the reactants are perfectly mixed before the chemical reaction and the flow is laminar. One of the characteristic quantities of laminar premixed flames is the laminar flame speed, S_L, which is defined as the velocity at which the unburned mixture, i.e reactants, moving into the flame in a direction normal to the flame sheet. Considering a stationary flame in one-dimensional tube geometry, see Fig. 2.1, the laminar flame speed is expressed as follows [20]:

$$S_L = U_u \tag{2.38}$$

where U_u is the velocity of the unburned mixture.

This definition of laminar flame speed does not consider the expansion of the flame, hence the laminar flame speed is the same as the laminar burning velocity. As mentioned previously, when a combustible gas cloud ignites with a weak ignition source, e.g spark, the flame begins in a laminar or in a quasi-laminar propagation mode and it becomes turbulent when the flame reaches obstructed areas. In some CFD codes, for example, "`FLACS`" [26] and "`XiFoam`" solver in the `OpenFOAM`, the turbulent burning velocities have been modeled as functions of the laminar flame speed of the fuel mixture. Therefore, an analytical correlation for modeling

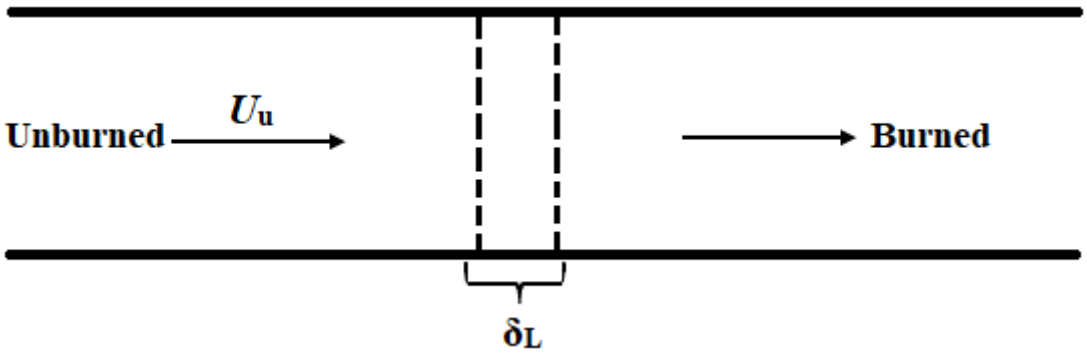

Figure 2.1: Schematic diagram of one-dimensional stationary flame. U_u is the velocity of the unburned mixture and δ_L is the laminar flame thickness.

the laminar flame speed is needed. The laminar flame speed can be modeled as a function of fuel mixture, equivalence ratio, pressure, and temperature of the unburnt gas. Various forms of empirical and semi-empirical relationships have been proposed for the laminar flame speed by several workers [27,28]. Among many of the empirical correlations for the laminar flame speed, the "power law" formula is the simplest and adapted in the "XiFoam" turbulence combustion solver of the `OpenFOAM` toolbox:

$$S_L(\phi, T_u, p_u) = S_L^o \left(\frac{T_u}{T_o}\right)^{\alpha} \left(\frac{p}{p_o}\right)^{\beta} \ , \tag{2.39}$$

where S_L^o is the laminar flame speed, also known as unstrained laminar flame speed, measured at initial/room conditions, i.e. at $T_u = T_o$ and $p = p_o$, for a given equivalence ratio ϕ, and α and β are constants or mixture strength-dependent terms.

Gülder [28] proposed the empirical expression to represent the laminar flame speed at room conditions as a function of equivalence ratio:

$$S_L^o = ZW\phi^{\eta} exp[-\xi(\phi - 1.075)^2] \ , \tag{2.40}$$

where $Z = 1$ for single constituent fuels, and W, η, and ξ are constants specified for each fuel.

The characteristic length scale ℓ_L, also known as flame thickness, and chemical timescale τ_L of the laminar flame can be calculated as a function of laminar flame speed as follow [18, 21]:

$$\ell_L = \frac{\nu}{S_L} \ , \qquad \tau_L = \frac{\nu}{(S_L)^2} \ , \tag{2.41}$$

here, the viscosity and diffusivity assumed to be either approximately equal or they vary similar to each other.

2.3.2 Turbulent premixed flames

In most gas explosions, the flames begin in laminar propagation mode and the flame front propagates at a speed S_L^o. When these laminar flames interact with turbulence eddies, which are generated because of the flow instabilities and/or the presence of the obstacles in the flow direction, they become turbulent. This interaction may lead to a strong increase in the consumption rate of the reactants and of the overall flame surface area, as described in Section 2.4.1. As

discussed earlier, in laminar premixed flame, the flame propagation speed depends on the thermal and chemical properties of the fuel-oxidizer mixture. In a turbulent premixed flame, the turbulent propagation speed S_T, also known as the turbulent burning velocity, is, however, more dependent on the character of the flow in addition to the properties of the fuel-oxidizer mixture. There are various correlations for the ratio of the turbulent to the laminar flame speed corresponding to different regimes of turbulent premixed flames. The turbulent burning velocity was first theoretically expressed by Damköhler [29]. He identified two deference regimes based on the turbulence scale magnitude as compared to the laminar flame thickness. For large turbulence scale, i.e. the turbulence scale larger than the flame thickness, he assumed that the wrinkled flame front interaction with the turbulence flow field is purely kinematic and hence, independent of length scales. This corresponding to the corrugated flamelet regime, see Section 2.3.3. He expressed the mass flux $\dot{m}$ of the unburning gas through the turbulent flame surface area A_T to the mass flux through the area of the approach flow with the laminar and turbulent burning velocity:

$$\dot{m} = \rho_u S_L A_T = \rho_u S_T A \ , \tag{2.42}$$

where ρ_u is the unburned mixture density. From Eq. (2.42) the turbulent burning velocity can be defined as

$$\frac{S_T}{S_L} = \frac{A_T}{A} \ . \tag{2.43}$$

For large scale and week intensity turbulence, using the geometrical approximations with a Bunsen flame, Damköhler proposed that

$$\frac{A_T}{A} = \frac{S_L + u'}{S_L} \ , \tag{2.44}$$

where u' is the characteristics fluctuation velocity in the unburned gas. Inserting Eq. (2.44) into Eq. (2.43) gives

$$\frac{S_T}{S_L} = 1 + \frac{u'}{S_L} \ . \tag{2.45}$$

For strong turbulence, i.e. $u'/S_L >> 1$, Eq. (2.45) becomes

$$S_T \approx u' \ . \tag{2.46}$$

Many researchers were tried to modify Damköhler's analysis. For example, Clavin and Williams [30] expressed the ratio of turbulent and laminar flame speed as

$$\frac{S_T}{S_L} = 1 + \left(\frac{u'}{S_L}\right)^2 \ , \tag{2.47}$$

the expression proposed by Pope and Anand [31] is written as

$$\frac{S_T}{S_L} = 2.1\left(\frac{u'}{S_L}\right) \ , \tag{2.48}$$

and Gülder [32] also proposed an expression, which is written as

$$\frac{S_T}{S_L} = 1 + 0.62\left(\frac{u'}{S_L}\right)^{1/2} Re_\eta. \tag{2.49}$$

In Eq. (2.49), Re_η is the Reynolds number based on the Kolmogorov length scale. All the formulations of the ratio of turbulent to laminar flame speeds, Equations (2.45)–(2.49), are corresponding to the flamelets regimes.

2.3.3 Premixed turbulent combustion regimes

Different authors use different dimensionless groups to distinguish the different regimes of turbulent premixed flames. For example, Borghi [33] and Peters [34] was used the length and velocity scales, while Williams [35] was used the Reynolds and Damköhler number to make the diagrams defining turbulent combustion regimes. Here, the premixed turbulent combustion regimes diagram of Peters [36], shown in Fig. 2.2, is used to discuss some of the turbulent premixed flame types.

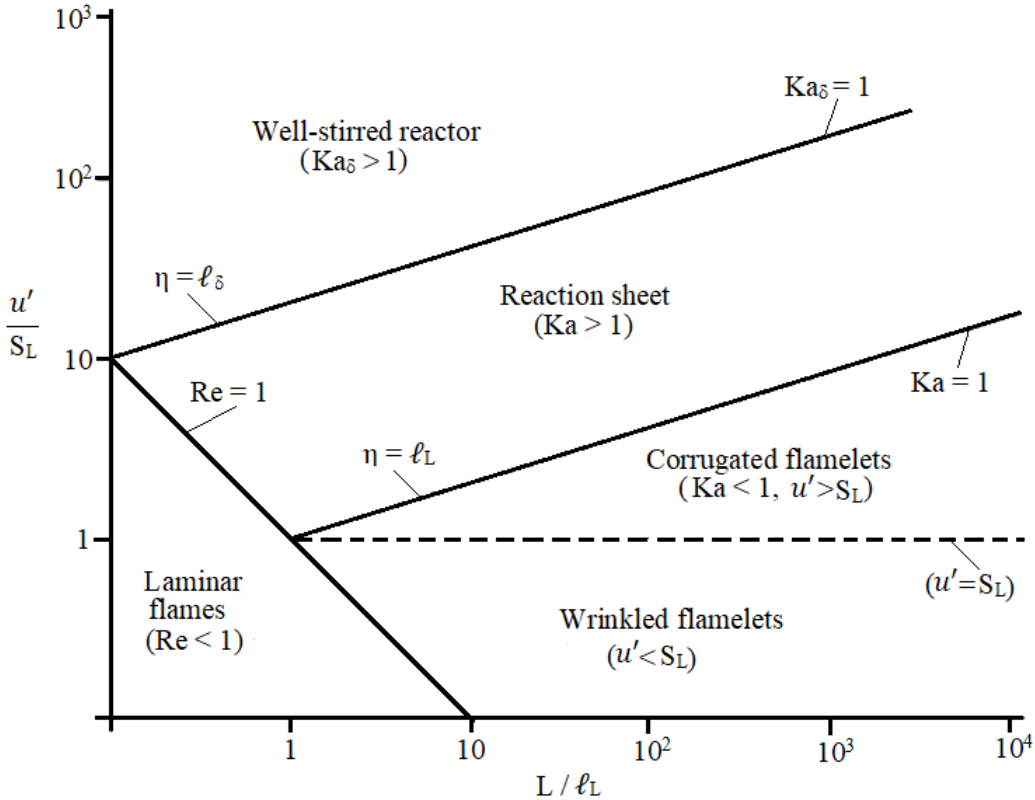

Figure 2.2: Diagram for different regimes of turbulent premixed combustion, after Peters [36].

In Fig. 2.2, three dimensionless groups are used: the turbulent Reynolds number based on the integral length scale, Re, is defined as

$$Re = \frac{u'L}{\nu} = \frac{u'}{S_L}\frac{L}{\ell_L} \ , \tag{2.50}$$

the turbulent Karlovitz number, Ka, is expressed as

$$Ka = \frac{\tau_L}{\tau_\eta} = \left(\frac{\ell_L}{\eta}\right)^2 = \left(\frac{u'\eta}{S_L}\right)^2 \ , \tag{2.51}$$

and the karlovitz number based on the inner layer thickness ℓ_δ, Ka_δ, which is defined as

$$Ka_\delta = \left(\frac{\ell_\delta}{\eta}\right)^2 = \delta^2 Ka \ , \tag{2.52}$$

where δ is the order of 0.1. Fig. 2.2 plots $\log(u'/S_L)$ versus $\log(L/\ell_L)$ and the lines $Re = 1$, $Ka = 1$, and $Ka_\delta = 1$ represent transition boundaries between the different premixed turbulent

combustion regimes. A boundary for $u' = S_L$ separates the two flamelets regimes, namely the wrinkled and corrugated flamelets. The turbulent flame regimes are separated by a boundary $Re = 1$ from the laminar flame.

As shown in Fig. 2.2, Peters pointed out five regimes. The laminar flame regime is characterized by $Re < 1$, week turbulence intensity, and small turbulence scale. The flow is laminar and the flame front propagated at a speed of S_L. The wrinkled flamelet regime is characterized by $Re > 1$, $Ka < 1$, and $u'/S_L < 1$. Here, the flame thickness is much smaller than the Kolmogorov length scale. Since $Ka < 1$, the flame element holds its laminar flame structure and the turbulence only slightly wrinkles the flamelet surface. Above the line $u' = S_L$, the corrugated flamelet regime is found. Since this regime also characterized by $Ka < 1$, the flame element still holds its laminar flame structure. However, due to larger fluctuations (since $u'/S_L > 1$), the flamelet becomes folded, which can lead to pockets or islands of unburned and burned mixtures. Above the line $Ka = 1$, the reaction sheet regime is found. This regime is characterized by $Re > 1$, $Ka > 1$, and $Ka_\delta < 1$. Since it has a lower boundary of $Ra = 1$, which implies $\eta \approx \ell_L$, for larger eddies the flames still behave as flamelet eddies. While the smallest eddies can penetrate into the flame structure and increases the rate of the heat and mass transfers since $Ka > 1$ (implies $\eta < \ell_L$). Above the boundary $Ka_\delta = 1$, the well-stirred reactor regime appears, which is characterized by $Re > 1$ and $Ka_\delta > 1$. Here, the smallest eddies are smaller than the inner layer thickness. Hence, the Kolmogorov eddies can now enter the structure of the reaction zone and the turbulence can have a strong effect on the chemistry. This enhanced diffusion, and hence, the rate of heat transfer from the inner layer to the preheat zone, which can lead to local flame extinction.

2.3.4 Flame wrinkling combustion model

This flamelet combustion model was proposed by Weller [37]. He assumed that the combustion took place in the flamelet regime, a relatively thin layer separating the unburned and burned gases. The effect of the turbulence is that only wrinkles and stretches the flame front, which propagates locally in laminar mode at unstretched laminar speed. Hence, increases the flame front area, which in turn increases the effective flame speed. In premixed combustion, the flame propagates from the burned to unburned gases and this flame propagation denoted by the progress variable, c. This progress variable taking values 0 and 1 in fresh and fully burned gas regions, respectively, and between 0 and 1 across the flame which describes the progress of the reaction. A progress variable, c, can be defined using temperature, reactant mass fraction, and so on. It can be calculated in terms of temperature as follows

$$c = \frac{T - T_u}{T_b - T_u} \ . \tag{2.53}$$

Here, T is the temperature, and the subscripts u and b represent the unburned and burned gases.

The thermophysical process of flame propagation is represented by the transport equation for the density-weighted mean regress variable b, $b = 1 - c$, and can be expressed as

$$\frac{\partial}{\partial t}(\overline{\rho}\tilde{b}) + \boldsymbol{\nabla} \cdot (\overline{\rho}\tilde{u}\tilde{b}) - \boldsymbol{\nabla} \cdot \left(\frac{\mu_t}{Sc_t}\boldsymbol{\nabla}\tilde{b}\right) = -\overline{\rho}S_c \ , \tag{2.54}$$

Where Sc_t is the turbulent Schmidt number and can be expressed as $Sc_t = \frac{\mu}{\rho\mathcal{D}}$, $\mathcal{D}$ is the diffusion coefficient.

The reaction regress source term on the right-hand side of Eq. (2.54), S_c, can be modeled as

$$\overline{\rho} S_c = \overline{\rho_u} S_L \Xi \left| \boldsymbol{\nabla} \tilde{b} \right| \ , \tag{2.55}$$

where ρ_u is the unburned mixture density, S_L is the laminar flame speed, and Ξ represents the sub-grid flame wrinkling, which can be defined as the ratio of turbulent and laminar flame speed.

Inserting Eq. (2.55) into Eq. (2.54) gives

$$\frac{\partial}{\partial t}(\overline{\rho}\tilde{b}) + \boldsymbol{\nabla} \cdot (\overline{\rho}\tilde{u}\tilde{b}) - \boldsymbol{\nabla} \cdot \left(\frac{\mu_t}{Sc_t} \boldsymbol{\nabla} \tilde{b} \right) = -\overline{\rho_u} S_L \Xi \left| \boldsymbol{\nabla} \tilde{b} \right| \ . \tag{2.56}$$

The sub-grid flame surface wrinkling factor Ξ can be computed using the transport equation, which can be written as [28]

$$\frac{\partial \Xi}{\partial t} + U_s \cdot \boldsymbol{\nabla} \Xi = G\Xi - R(\Xi - 1) + (\sigma_s - \sigma_t)\Xi \ , \tag{2.57}$$

where U_s is the average velocity of the flame surface, σ is the resolved strain rate. The first and second terms on the right-hand side of Eq. (2.57), respectively, are the sub-grid turbulent generation and removal rates. The rate coefficients G and R, respectively, are modeled as

$$G = R \frac{\Xi_{eq} - 1}{\Xi eq} \ , \qquad R = \frac{0.28}{\tau_\eta} \frac{\Xi^*_{eq}}{\Xi^*_{eq} - 1} \ , \tag{2.58}$$

where τ_η is the Kolmogorov time scale and Ξ_{eq} is the equilibrium Ξ given by the following simple algebraic expression

$$\Xi_{eq} = 1 + 2(1 - b)(\Xi^*_{eq} - 1) \ . \tag{2.59}$$

The equilibrium wrinkling at the Kolmogorov turbulence length scale, Ξ^*_{eq}, can be expressed by the algebraic equation of the sub-grid flame wrinkling proposed by Gülder, Eq. (2.49) see Section 2.3.2.

2.3.5 Eddy Dissipation Combustion Model (EDM)

In order to compute combustion, the expression for the mean reaction rate, which is the source term in the equation for the mean mass fraction, Eq. (2.28), is needed. The Eddy Dissipation Combustion Model (EDM) proposed by Magnussen and Hjertager [38] is widely used in many commercial CFD codes to model the mean reaction rate directly.

In this model, the assumption of very fast chemical kinetics of the system was used. Hence, the overall rate of combustion is controlled by the rate of the intermixing of the fuel and oxidizer eddies at a molecular level. The model is developed using the features of both the diffusion and premixed flame. In diffusion flame, the fuel and oxidizer located in separate eddies and they are mixed slowly due to turbulence prior to the occurrence of the reaction. In a premixed flame, the fuel and oxidizer occur in the same eddies and separated by the hot combustion product containing eddies. The propagation of the flame is dependent on the diffusion of radical and the mixing of the hot products with the unburned mixture. The reaction occurs in the mixture is controlled by the chemical kinetics. Thus, the combustion depends on both mixing and chemical kinetics, but when the chemical reaction is much faster than the mixing, the combustion becomes mixing-controlled. In this case, the chemical kinetics can be neglected.

In turbulence flow, the mixing process is mostly dependent on the characteristics of the turbulence. As discussed earlier, in turbulent flow, the kinetic energy is transferred from the mean flow into the larger eddies and continuously transfer to smaller and smaller eddies until finally dissipated by viscosity into heat at the smallest eddies (i.e. eddies at the Kolmogorov microscales). The entire process is known as the kinetic energy cascade [39]. Hence, the mixing of fuel and oxidizer eddies at the molecular level is closely related to the rate of the dissipation of the kinetic energy. The mean concentration of species is related to the fluctuations since fuel and oxidizer occur as fluctuating intermittent quantities. As a result, the mean concentration or mass fraction of the reacting species are used to define the rate of dissipation. Thus, the rate of reaction of fuel can be expressed by the turbulence dissipation of reactant and product eddies as [38]

$$\overline{R}_{fu} = A\overline{\rho}\frac{\varepsilon}{k}\min(\tilde{Y}_{fu}, \tilde{Y}_{ox}/r, B\tilde{Y}_p/(1+r)) \ , \tag{2.60}$$

where A and B are the model constants, ρ is the mixture density, $\tilde{Y}_{fu}$ is the mass fraction of fuel, $\tilde{Y}_{ox}$ is the mass fraction of oxidizer, $\tilde{Y}_p$ is the mass fraction of the reaction product, and r is the stoichiometric amount of oxidizer required to burn 1 kg of fuel. As seen from Eq. (2.60), reactions are controlled and determined by the least available species.

2.4 Gas explosions

A gas explosion can occur when the premixed hydrocarbon-air cloud ignites by some ignition source and results in a rapid increase of pressure. When the premixed gas cloud is ignited, the flame can propagates from the burned to unburned gases in two different modes: (i) deflagration: in this mode, the flame propagates at a subsonic speed relatively to the unburned gas with the typical flame speeds ranging from 1 - 1000 $\mathrm{m\,s^{-1}}$ [40]. This flame propagation mode is the most common in the gas explosions. (ii) detonation: in this propagation mode, the combustion wave propagates at a supersonic speed relative to the speed of sound in the unburned gas in front of the wave with the velocity of 1500-2000 $\mathrm{m\,s^{-1}}$ [40]. The peak overpressure can be typically around 15 -20 bar [40]. In this mode, the shock wave and the combustion wave are strongly coupled.

The pressure generated in explosions can be different depending on the environment in which the explosion occurred. If the cloud is confined, following ignition, the combustion products are producing due to the flame propagation through the gas cloud. Because these combustion products are at a high temperature and the gases within the volume cannot freely expand to occupy a larger volume, the pressure within the confined volume rises.

Gas explosions occur within a building or a room which is partially open is called partially confined explosions. Here, the pressure can be relieved only through the opening/vent areas. The vent can be designed as fully open area in the wall or light relief walls that can open or break quickly at low overpressure. In this kind of explosion, the pressure generated by the flame and pressure relief through the vent determines the pressure build-up during a gas explosions. Hence, the results overpressures will depends on, size, location and type of explosions vent areas.

In an unconfined, i.e fully open, and unobstructed situations, the flame is not likely to accelerates to the flame speed more than 25 $\mathrm{m\,s^{-1}}$ and the overpressures will be insignificant. The flame instabilities, turbulence generated due to the wind in the atmosphere and the interaction

of the flame with the ground surface are the main reasons for the acceleration of the flame.

In the presence of the obstacles in any of the gas explosions types discussed above, the flame may accelerate to several hundred meters per second and resulting in the generation of damaging overpressures. This is because of the turbulence generated when the unburnt gas mixture interacts with the obstacles, which in turn increases the combustion rate, see Section 2.4.1. In general, the degree of pressure generation in explosions is dependent on various factors [1, 2]:

- Fuel-air type and stoichiometry
- Size and location of the fuel-air cloud
- Ignition location and strength
- Degree of confinement
- Vent position and size
- Obstacle number, layout, and size

2.4.1 The mechanism of flame propagation and pressure build-up

If there is an explosive gas cloud, following ignition with a weak ignition source (e.g. spark), the flame will start out as a slow laminar flame with typical flame speeds in the range between 3.5 and 25 $\mathrm{m\,s^{-1}}$ [40].

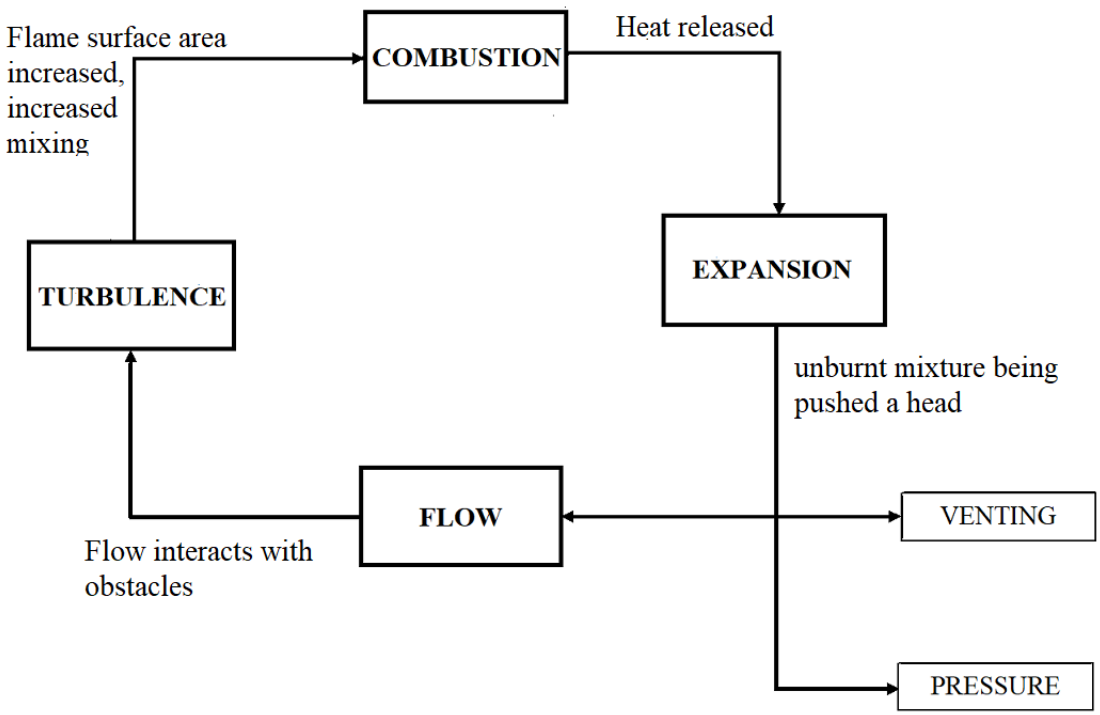

Figure 2.3: Mechanism of flame propagation due to turbulence, adapted from [11]

The resulting combustion products expanded and pushed the unburned mixture ahead of the flame. If there is no obstacle in front of the flame, the flame will remain in a laminar or in a

quasi-laminar propagation mode. However, if freely propagating flames encounters obstacles in the path of the expansion, the flame can accelerate to high speeds. The mechanism of flame acceleration due to the presence of repeated obstacles is governed by a Schelkin mechanism, see Fig. 2.3.

As Fig. 2.3 shows, the unburned mixture being pushed ahead of the flame when interacts the obstacles, it will become turbulent in the wake of obstruction. When the flame front reaches this turbulence region, the flame is distorted increasing the flame surface area which in turn, increases the rate of heat release. As a consequence, the combustion rate is enhanced and also increases the rate of expansion. The expansion gives more flow of the unburned gas, and the flow produces more turbulence and the turbulence accelerating the combustion rate further. Therefore, this strong feedback mechanism is causing rapid flame acceleration and resulting in higher overpressure. If there is venting, the resulting overpressure will decreases since some of the kinetic energy is vented.

Chapter 3

Modelling of a gas explosion in complex geometry using KFX-EXSIM

This chapter will present the introduction to KFX-EXSIM, and some of the mathematical models and numerical simulation method used in KFX-EXSIM code to model and simulate gas explosions in complex geometries. Most of the information found from the KFX-EXSIM user manual [41], the work of sæter [11], and the previous work [42].

3.1 Introduction about KFX-EXSIM

KFX-EXSIM is an integration of the industrial fire simulation code **KAMELEON FIREEX** (KFX) and an industrial explosion simulation code **EXPLOSION SIMULATOR** (EXSIM). KFX was developed and tested by Professor Bjørn F. Magnussen and co-workers at ComputIT and NTNU/Sintef through a period of 40 years. In close cooperation with a gas and oil company Shell, professor Bjørn H. Hjertager developed EXSIM, based on extensive R&D activities on turbulent reacting flow since 1980. KFX-EXSIM is primarily aimed at simulating gas explosions in the oil and gas platform and only handles the deflagration process.

KFX-EXSIM solves the compressible conservation equation for mass, momentum, enthalpy, and mass fraction of species on a 3D (3-dimensional) Cartesian grid using the Finite volume method (FVM). A Porosity/Distributed Resistance (PDR) concept is used to model the effect of sub-grid obstacles on the turbulent reacting flow in complex 3D geometries. The EDM [38] together with the ignition/extinction modification [43] and the extended version of $k - \varepsilon$ are used to model the turbulent fuel combustion rate and turbulence, respectively. The model of Van den Berg [44] is used to model the initial laminar flame propagation. A brief description of the Porosity/Distributed Resistance (PDR) concept, the extended version of $k - \varepsilon$ turbulence model, the Van den Berg quasi-laminar combustion model, and the EDM are presented in the following sections.

3.2 Porosity/Distributed Resistance (PDR) Concept

The KFX-EXSIM code uses a PDR concept that allows a detail representation of complex geometries (e.g. oil and gas platform may contain hundreds or thousands of objects) using a Cartesian grid. This concept was first proposed by Patankar and Spalding and implemented for

the study of heat exchangers, regenerators and nuclear reactors [45]. Sha et al. [46] and Sha and Launder [24] have extended the PDR method to include turbulence modeling. In this concept, large obstacles like walls, ground, and large objects are resolved on-grid; while smaller obstacles are represented sub-grid. In other words, large scales associated with large obstacles are resolved and small scales associated with small obstacles are modeled. This essentially means that flow resistance, turbulence generation, and flame enhancement due to sub-grid obstacles are represented as a source term in the respective equations.

The PDR approach first converts the geometrical details to cell-wise values of porosities, i.e volume and area porosity, so that only the unblocked part of the control volume/cell is available for flow. Then the additional flow resistance and turbulence generation due to sub-grid obstacles are modeled.
Considering the control volume shown in Fig. 3.1, the volume porosity or fraction occupied by the fluid can be expressed as [11]

$$\beta_v = \frac{V_s}{V_f + V_s} = \frac{V_f}{\Delta x \Delta y \Delta z}\,, \tag{3.1}$$

where V_s and V_f are the volume of the obstacle and fluid, respectively.

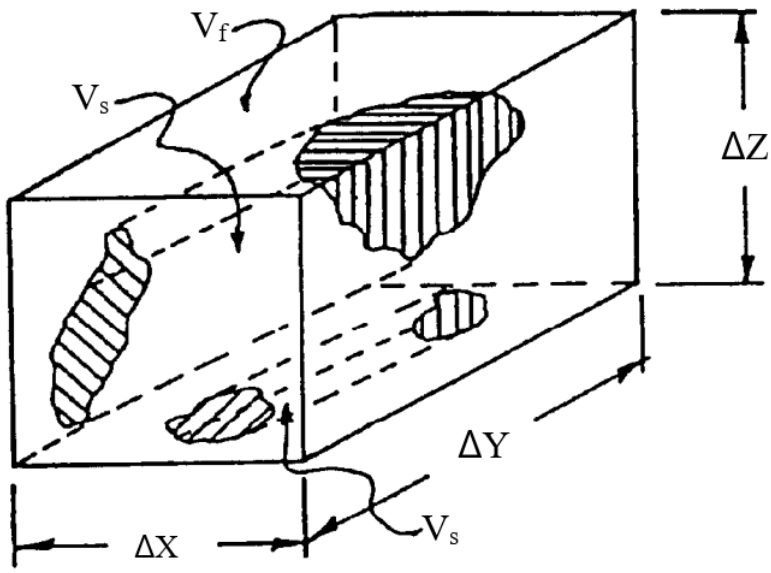

Figure 3.1: Control volume illustrating the part occupied by the obstacle, adapted from [47].

Fig. 3.2 illustrates the control volume with an area fraction occupied by the obstacle in the x_i direction. The area porosity or fraction available for the fluid flow in the x_i direction can be written as [11]

$$\beta_x = \frac{A_{sx}}{A_{fx} + A_{sx}}\,, \tag{3.2}$$

where A_{sx} and A_{fx}, respectively, are the surface area of a solid object (obstacle) and fluid. Similarly, equivalent expressions of area porosities can be found for the y and z directions. All the volume and area porosities have the value from 0.0, i.e completely blocked, to 1.0. i.e completely open. They are fixed in time for fixed grids but vary with changes in grid size.

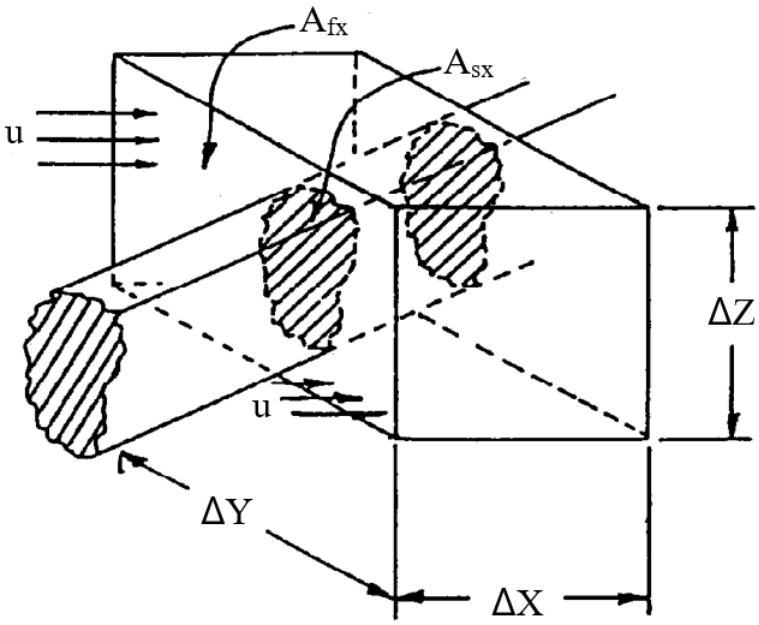

Figure 3.2: Control volume with a surface porosity in x_i direction, adapted from [47].

Section 3.3 describes the governing equations used in `KFX-EXSIM` and the modeling of the additional fluid flow resistance and generation of the turbulence due to the obstacles.

3.3 PDR formulation of the conservation equations

Applying the PDR concept, area porosities, see Eq. (3.2) for x_i direction, are integrated into the mass, diffusion fluxes, and the surface integral terms. Whereas the volume porosity, see Eq. (3.1), is integrated into the appropriate source and transient terms of the Favre-averaged equations, Eq. (2.24), Eq. (2.26), and Eq. (2.28). The additional flow resistance due to small scale obstacles is modeled as a source term in the Favre-averaged momentum equation, Eq. (2.24). Hence, the PDR formulation of the Favre-averaged conservation equations can be rewritten as [11]

$$\frac{\partial}{\partial t}\left(\beta_v\bar{\rho}\right) + \frac{\partial}{\partial x_i}\left(\beta_a\bar{\rho}\tilde{u}_i\right) = 0\,, \tag{3.3}$$

$$\frac{\partial}{\partial t}(\beta_v\bar{\rho}\tilde{u}_i) + \frac{\partial}{\partial x_j}(\beta_a\bar{\rho}\tilde{u}_j\tilde{u}_i) = -\beta_v\frac{\partial\bar{p}}{\partial x_i} + \frac{\partial}{\partial x_j}(\beta_a\bar{\tau}_{ij} - \beta_a\overline{\rho u_i'' u_j''}) + \beta_v\bar{\rho}g_i + \overline{\mathcal{R}}_i\,, \tag{3.4}$$

$$\frac{\partial}{\partial t}\left(\beta_v\bar{\rho}\tilde{h}\right) + \frac{\partial}{\partial x_j}\left(\beta_a\bar{\rho}\tilde{u}_j\tilde{h}\right) = \frac{\partial}{\partial x_j}(\beta_a\frac{\mu_{eff}}{\sigma_h}\frac{\partial\tilde{h}}{\partial x_j}) + \beta_v\frac{D\bar{p}}{Dt} + \frac{\partial\overline{Q}}{\partial t} + \beta_v\overline{S}_h\,, \tag{3.5}$$

and

$$\frac{\partial}{\partial t}\left(\beta_v\bar{\rho}\tilde{Y}_k\right) + \frac{\partial}{\partial x_j}\left(\beta_a\bar{\rho}\tilde{u}_j\tilde{Y}_k\right) = \frac{\partial}{\partial x_i}(\beta_a\frac{\mu_{eff}}{\sigma_{Yk}}\frac{\partial\tilde{Y}_k}{\partial x_j}) + \overline{R}_k\,, \tag{3.6}$$

where σ_h is an effective Prandtl number and σ_{Yk} is an effective Schmidt number. The turbulence Reynolds stress, $\overline{\rho u_i'' u_j''}$, in Eq. (3.4) is modeled using Boussinesq approximation, Eq. (2.31) (see Section 2.2.5). The effective viscosity, μ_{eff}, can be expressed as the sum of the molecular viscosity, μ_l, and turbulence viscosity, Eq. (2.33) (see Section 2.2.5).

In Eq. (3.4), the additional resistance to fluid flow in the x_i direction due to unresolved (sub-grid) obstacles located within the control volume is represented by $\mathcal{R}_i$ and can be expressed as [47]

$$\mathcal{R}_i = -f_i A_w \frac{1}{2}\bar{\rho}|\tilde{U}_i|\tilde{U}_i \,. \tag{3.7}$$

Here, A_w and f_i are the wetted area of the obstructions per unit volume and the friction factor, respectively. The friction factor f_i may depend on various parameters, such as porosity, velocity, the distance between obstacles (pitch), typical dimension or hydraulic diameter, obstacles orientation and shape [10, 11].

3.3.1 Resistance due to single object

Additional resistance to fluid flow, $\mathcal{R}_i$, due to a single solid object can be modeled as

$$\mathcal{R}_i = -C_R A_i \left(\frac{1}{\beta_i} - 1\right)^2 \frac{1}{2}\bar{\rho}|\tilde{U}_i|\tilde{U}_i \,, \tag{3.8}$$

where A_i represents the frontal area per unit volume of the solid object, and C_R is the drag coefficient of the single solid object. When the control volume is completely blocked, i.e. β_i goes to zero, Eq. (3.8) becomes infinity. The C_R depends on the shape and orientation of the solid object and may have different values. It is typically calibrated against various experiments. Hjertager et al. [47] and Sæter [11] were recommended some C_R values for typical flow types and shape of the obstacles, for example:

- sharp-edged obstacles : 1.2
- rounded obstacles, such as tube or sphere : 0.5
- cylinders : 1.2
- box-beams : 2.0
- cubes : 1.3
- beams : 1.0

These values of the drag coefficients were used in the `KFX-EXSIM` code.

3.3.2 Resistance through densely packed regions

In the presence of more than one obstacle within the control volume, flow resistance through densely packed regions can be modeled as [41]

$$\mathcal{R}_i = \frac{\Delta p}{\Delta x_i} = \frac{C_R}{D_h}\frac{(1-\beta_i)}{\beta_i}\frac{1}{2}\bar{\rho}|\tilde{U}_i|\tilde{U}_i \,. \tag{3.9}$$

Here, $\Delta p/\Delta x_i$ is the pressure drop per unit length and D_h is the typical obstacle dimension (hydraulic diameter) in the obstructed region. The model constant, C_R, is calibrated against explosion experiments [11] and the value of 0.25 is used in the `KFX-EXSIM` code.

3.4 Turbulence model

In KFX-EXSIM, the convection, diffusion, production, and dissipation of turbulence are modeled by the standard $k-\varepsilon$ turbulence model, see Section 2.2.5. However, it was extended in order to represent turbulence production from the unresolved/sub-grid obstacles. In the KFX-EXSIM code, molecular viscosity is assumed to be very smaller than turbulence viscosity, $\mu_l \ll \mu_t$, and can be neglected. Therefore, the transport equation for the turbulence energy, k, and the rate of dissipation of turbulence energy, ε, for the extended version of $k-\varepsilon$ model read as [11, p. 15]

$$\frac{\partial}{\partial t}(\beta_v \bar{\rho} k) + \frac{\partial}{\partial x_j}(\beta_a \bar{\rho} \tilde{u}_j k) = \frac{\partial}{\partial x_j}\left(\beta_a \frac{\mu_{eff}}{\sigma_k}\frac{\partial k}{\partial x_j}\right) + G - \beta_v \bar{\rho}\varepsilon\,, \tag{3.10}$$

$$\frac{\partial}{\partial t}(\beta_v \bar{\rho}\varepsilon) + \frac{\partial}{\partial x_j}(\beta_a \bar{\rho} \tilde{u}_j \varepsilon) = \frac{\partial}{\partial x_i}\left(\beta_a \frac{\mu_{eff}}{\sigma_\varepsilon}\frac{\partial \varepsilon}{\partial x_j}\right) + C_{\varepsilon 1}\frac{\varepsilon}{k}G - C_{\varepsilon 2}\beta_v \bar{\rho}\frac{\varepsilon^2}{k}\,. \tag{3.11}$$

Turbulence energy production rate, G, in Eq. (3.10) and Eq. (3.11) can be expressed as

$$G = G_S + G_R\,. \tag{3.12}$$

The production rate of turbulence due to shear and compression/expansion,G_S, in Eq. (3.12), can be expressed as [47]

$$G_S = \beta_v \bar{\sigma}_{ij}\frac{\partial \tilde{u}_j}{\partial x_j}\,, \tag{3.13}$$

where σ_{ij} is the turbulence stress tensor. Whereas the turbulence production rate due to internal frictional resistance from the sub-grid obstacles, G_R, can be written as [24]

$$G_R = C_B|\tilde{u}_i|\overline{\mathcal{R}}_i\,, \tag{3.14}$$

where $\mathcal{R}_i$ is additional resistance to fluid flow due to sub-grid obstacles, see Eq. (3.8) and Eq. (3.9). C_B is a model coefficient that indicates the degree of the obstacle flow resistance going into turbulence generation. It depends on the type of obstacle and its value is determined through calibration against explosion experiments. If the turbulence generation rate, G, is expressed by G_S only and applied Eq. (3.13) to Eq. (3.10) and Eq. (3.11), then the standard $k-\varepsilon$ turbulence model is obtained for resolved flows.

Some simple and complex simulations of gas explosions using the standard $k-\varepsilon$ model were conducted by Sæter [11]. The numerical results were compared to the experimental data and some of the results were not in good agreement with experiments. Therefore, the source term in the ε-equation, Eq. (3.11), is modified as [11]:

$$C_{\varepsilon 1}\frac{\varepsilon}{k}G = \frac{\varepsilon}{k}(C_{\varepsilon 1a}G_S + C_{\varepsilon 1b}G_R)\,, \tag{3.15}$$

where $C_{\varepsilon 1a}$ has the same value as $C_{\varepsilon 1}$, i.e = 1.44, whereas $C_{\varepsilon 1b}$ = 1.22.

3.5 Rate of combustion

The combustion is treated in the EXSIM explosion model as a single-step irreversible chemical reaction between fuel and oxidizer (air in the KFX-EXSIM explosion model). Hence, the reaction scheme can be written as:

$$\text{1 kg fuel} + \text{r kg air} \rightarrow \text{(1+r) kg products}\,, \tag{3.16}$$

where r is the stoichiometric air requirement to burn 1 kg of fuel. For this simple chemical reaction, the composition of the mixture is therefore determined by solving only two variables [10, 11]: namely the fuel mass fraction, $\tilde{Y_{fu}}$,

$$\frac{\partial}{\partial t}(\beta_v \bar{\rho} \tilde{Y}_{fu}) + \frac{\partial}{\partial x_j}(\beta_a \bar{\rho} \tilde{u_j} \tilde{Y}_{fu}) = \frac{\partial}{\partial x_j}\left(\beta_a \frac{\mu_{eff}}{\sigma_{Yfu}} \frac{\partial \tilde{Y}_{fu}}{\partial x_j}\right) + \overline{R}_{fu} \,, \tag{3.17}$$

and the mixture fraction, $\tilde{f}$,

$$\frac{\partial}{\partial t}(\beta_v \bar{\rho} \tilde{f}) + \frac{\partial}{\partial x_j}(\beta_a \bar{\rho} \tilde{u_j} \tilde{f}) = \frac{\partial}{\partial x_j}\left(\beta_a \frac{\mu_{eff}}{\sigma_f} \frac{\partial \tilde{f}}{\partial x_j}\right) . \tag{3.18}$$

where

$$\tilde{f} = \frac{\xi - \xi_\infty}{\xi_0 - \xi_\infty} \,. \tag{3.19}$$

Here, ξ is a conserved combined variable of, for example, the fuel mass fraction, $\tilde{Y}_{fu}$, and mass fraction of air, $\tilde{Y}_{air}$, ξ, expressed as

$$\xi = \tilde{Y}_{fu} - \frac{\tilde{Y}_{air}}{r} \,. \tag{3.20}$$

ξ_0 and ξ_∞ in Eq. (3.19), are the value of ξ at a fuel-rich and air-rich reference point, respectively. If a homogeneous premixed fuel-air mixture covers the entire computational domain, it yields a constant mixture fraction during the combustion process. Thus, only Eq. (3.17) is needed to be solved.

Fuel combustion rate, R_{fu}, in Eq. (3.17) is modeled as a laminar, $R_{fu,l}$, and a turbulent, $R_{fu,t}$, combustion rate. The models used in the `KFX-EXSIM` explosion model to modeling the laminar and turbulent combustion are described in the following and subsequent sub-sections.

3.5.1 Laminar combustion modeling

As described previously, if the explosive gas cloud is quiescent/non-turbulent initially and a week ignition happens, a relatively slow combustion result, which in turn gives a very thin reaction zone. For large scale/realistic explosion computations using fixed coarser grids (typically in the order of $1 \times 1 \times 1$ m), modeling such thin flames are not possible [11]. Hence, the quasi-laminar combustion models are applied to model the initial laminar flame propagation.

In `KFX-EXSIM`, the Van den Berg model [44] is applied:

$$\overline{R}_{fu,l} = \beta_v C_l \bar{\rho} \tilde{Y}_{lim} \,, \tag{3.21}$$

where Y_{lim} is the smallest of the three mass fractions, namely fuel mass fraction, Y_{fu}, mass fraction of air, Y_{air}/r, or mass fraction of fuel already burnt, $Y_{fu,b}$. C_l is a dynamic rate modeling constant, which is controlled to gives a correct burning velocity at any time for the laminar start of the flame propagation. It can be expressed as follows:

$$C_l = E_l \frac{\bar{\rho}_u u_l \tilde{Y}_{fu} A_f}{\int_v \bar{\rho} \tilde{Y}_{lim} dV} \,. \tag{3.22}$$

Here, u_l and A_f, respectively, are the laminar burning velocity and the flame area. The laminar enhancement factor, E_l, in Eq. (3.22) is included to take into account the increment of the

burning velocity as a result of wrinkling of the flame front. It can be expressed using the following relation:

$$E_l = \min[1.5 \ln(1 + \mathfrak{R}), 2.5] \,, \tag{3.23}$$

where $\mathfrak{R}$ is the radial distance of the flame front from the ignition source, is known as the flame propagation radius. The specified laminar burning velocity, u_l, can be calculated using the following relation [11, p. 62]:

$$u_l = u_{l,o} + d \times r; \;\; r \in [0 - 0.5]\mathrm{m} \,, \tag{3.24}$$

where r is the distance from the ignition, $u_{l,o}$ is initial laminar burning velocity in $\mathrm{m\,s^{-1}}$, and d is a constant value in $\mathrm{s^{-1}}$. The value of the initial laminar burning velocity and a constant d is different depending on the concentration and fuel-air mixture type. For example, for the stoichiometric methane-air mixture, the value of 0.38 $\mathrm{m\,s^{-1}}$ and 1.8 $\mathrm{s^{-1}}$ is used for $u_{l,o}$ and d, respectively.

3.5.2 Turbulent combustion modeling

`KFX-EXSIM` uses Eddy Dissipation Combustion Model (EDM) of Magnussen and Hjertager [38], see Section 2.3.5, together with the ignition/extinction modification proposed by Hjertager [43] to model turbulent combustion. The expression of the fuel reaction rate, Eq. (2.60), is modified to represent the flame enhancement due to sub-grid obstacles and is written as

$$\overline{R}_{fu,t} = \beta_v E_t A_t \frac{\varepsilon}{k} \overline{\rho} \tilde{Y}_{lim} \,. \tag{3.25}$$

Here, E_t is a turbulence enhancement factor to consider the break-up and acceleration of the flame due to the presence of various obstacles within the control volume and A_t is a model constant with a value of 30.

In order to Eq. (3.25) to be valid, the assumption of fast chemical kinetics of the system is applied, which is not true for most cases, e.g. in high-speed gas explosions [43]. Hence, Hjertager [43] made an ignition/extinction modification on the rate of combustion expression:

$$\begin{aligned} \overline{R}_{fu,t} &= \beta_v E_t A_t \frac{\varepsilon}{k} \overline{\rho} \tilde{Y}_{lim} && \text{when } \frac{\tau_{ch}}{\tau_e} \leq D_{ie} \\ \overline{R}_{fu,t} &= 0 && \text{when } \frac{\tau_{ch}}{\tau_e} \geq D_{ie} \end{aligned} \tag{3.26}$$

As seen from Eq. (3.26), two kinds of time scales are used to define the cold front quenching (ignition/extinction) criteria, D_{ie}, namely the turbulent eddy mixing time scale:

$$\tau_e = k/\varepsilon \;, \tag{3.27}$$

and the chemical time scale τ_{ch} which can be defined from the reaction rate. Considering the global one-step chemical reaction between fuel and air, see Eq. (3.16), the consumption rate of the fuel can be expressed as

$$\overline{R}_{fu} = -k_G(T) \cdot (\overline{\rho}\tilde{Y}_{fu})^a \cdot (\overline{\rho}\tilde{Y}_{air})^b, \tag{3.28}$$

where the global rate coefficient, K_G can be expressed by the empirical Arrhenius form,

$$k_G(T) = A \exp\left\{ \left(\frac{-E}{RT} \right) \right\}. \tag{3.29}$$

Here, A is a pre-exponential factor, E is activation energy, T is an absolute temperature, and R is a gas constant. The exponent a and b are the reaction order corresponding to fuel and air, respectively.

Assuming the chemical time is equal to the chemical induction time, the chemical time scale can be written as [43]

$$\tau_{ch} = A_{ch} \exp\left\{ \left(\frac{E}{RT} \right) \right\} . (\bar{\rho}\tilde{Y}_{fu})^a . (\bar{\rho}\tilde{Y}_{air})^b, \tag{3.30}$$

where A_{ch} is a constant, = 1/A.

3.6 Numerical solution method

The brief introduction to the numerical solution method that is applied in the `KFX-EXSIM` presents in this section. The main focus is on the Finite volume method (FVM), discretization of the transport equation, the solution algorithm used to solve the resulting non-algebraic equation, and boundary and initial conditions.

3.6.1 Finite volume method (FVM)

All the conservation equations mentioned in the previous sections can be written for the general variable ϕ as

$$\underbrace{\frac{\partial}{\partial t}(\rho\phi)}_{\text{transient}} + \underbrace{\frac{\partial}{\partial x_j}(\rho u\phi)}_{\text{convection}} = \underbrace{\frac{\partial}{\partial x_i}(\Gamma_\phi \boldsymbol{\nabla}\phi)}_{\text{diffusion}} + \underbrace{S_\phi}_{\text{source term}} . \tag{3.31}$$

Here, for simplicity, all the area porosities and the volume porosity are set equal to unity. In `KFX-EXSIM`, the solution of the general transport equation are performed by Finite volume method (FVM) with Cartesian coordinates. The term finite volume refers to the division of the physical domain into discrete control volumes of finite size, which surrounding each node point on a mesh. FVM starts with the integration of the governing transport equations on a control volume. This gives a set of discretized algebraic equations for a given grid nodal points, i.e a center point of the control volume [48].

`KFX-EXSIM` uses a staggered grid arrangement for the momentum equation. The reason for the implementation of a staggered grid is to avoid odd-even decoupling between the pressure and velocity, which can lead to ”checkerboard” problem. In the staggered grid, the velocity components are stored at the center-point nodes of skewed cells. Considering the configuration of a staggered grid in 2D with the center node p, see Fig. 3.3, the horizontal velocity component, u, is stored at the center-point node of the cell which skewed half a grid to the west, i.e red colored box in Fig. 3.3. While the vertical velocity component, v, is stored at the center point of the grid, which is skewed half a cell spacing to the south (the green colored control volume in Fig. 3.3). All scalar variables, for example, pressure, density, temperature, are stored and computed at the ordinary nodal points (•).

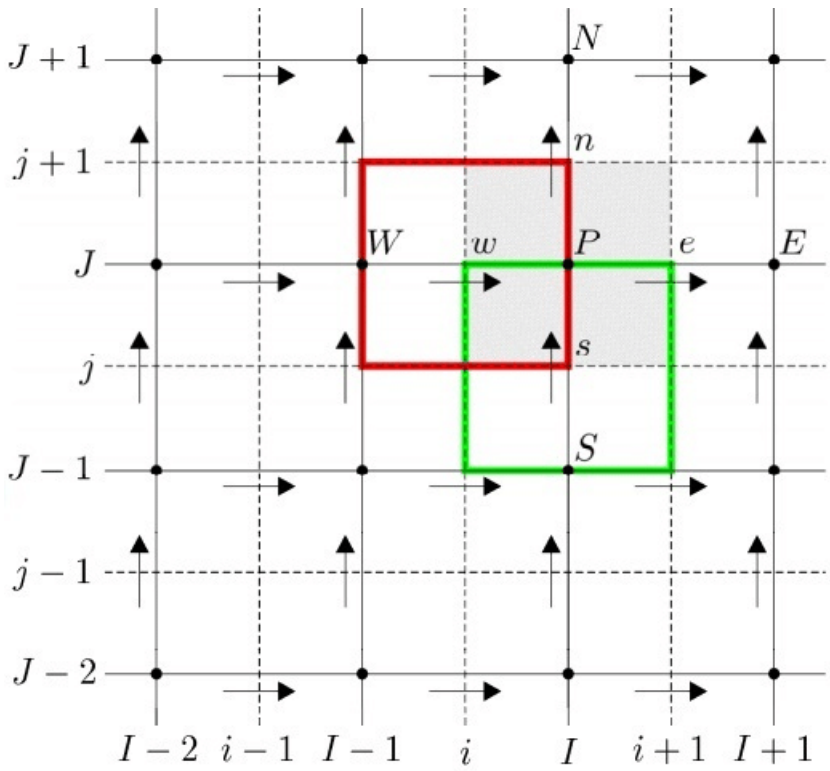

Figure 3.3: The Staggered grid for two-dimensional flow. The box with red color is the control volume for the u-velocity and β_x, the green colored box is the v-velocity and β_y control volume, and the grey box is the control volume for all the scalar variables.

3.6.2 The discretization of the transport equation

The general transport equation presented above, see Eq. (3.31), is integrated over a three-dimensional control volume. Using the Gauss' divergence theorem, the integrated form of Eq. (3.31) can be written as [48, p. 26]

$$\frac{\mathrm{d}}{\mathrm{d}t}\left(\int_{CV} \rho\phi dV\right) + \int_A (n.(\rho\phi u)dA = \int_A n.(\Gamma_\phi \boldsymbol{\nabla}\phi)dA + \int_{CV} S_\phi dV\,, \tag{3.32}$$

where n is the normal vector. Integrating Eq. (3.32) over a finite time step Δt and rearranging the order of integration in the rate of change term gives [48, p. 168]:

$$\int_{CV}\left(\int_t^{t+\Delta t} \frac{\partial}{\partial t}(\rho\phi)dt\right)dV + \int_t^{t+\Delta t}\left(\int_A n.(\rho u\phi)dA\right)dt = \int_t^{t+\Delta t}\left(\int_A n.(\Gamma\boldsymbol{\nabla}\phi)dA\right)dt + \int_t^{t+\Delta t}\int_{CV} S_\phi dV dt\,. \tag{3.33}$$

The fully implicit Euler scheme is used to perform the integration over a finite time step, Δt, in the `KFX-EXSIM` explosion model. The advantage of this scheme is that it is unconditionally stable for any time steps, however, it is only first-order accurate [22]. Using a 3D control volume, the result of the fully implicit formulation can be written as

$$a_P\phi_P = a_W\phi_W + a_E\phi_E + a_S\phi_S + a_N\phi_N + a_B\phi_B + a_T\phi_T + a_P^o\phi_P^o + S_u\,, \tag{3.34}$$

where a_P is the coefficient for the central node and can be expressed as

$$a_P = a_W + a_E + a_S + a_N + a_B + a_T + a_P^o - S_P \,,$$

where

$$a_P^o = \frac{\rho_P^o \Delta x \Delta y \Delta z}{\Delta t} \,.$$

Here, the superscript ^{o} represents the specific variable at the "old" time step.

Using the linear assumption, the source term S_ϕ can be linearized as follows

$$S_\phi = S_u + S_P \phi_P \,. \tag{3.35}$$

If the S_P term in Eq. (3.35) is sufficiently large, the coefficient of the central node a_P may become negative and makes the numerical scheme unstable. Hence, to maintain the stability of the numerical scheme, the value of S_P should keep less than or equal to zero.

In the `KFX-EXSIM`, the integration of the convective term is performed using upwind differencing scheme. This scheme has some advantages, such as the flow direction is considered when the value of the variable determined at the cell face, the coefficients in the discretized equation always has positive values, and the boundedness requirements are fulfilled. However, the scheme is only first-order accurate and has numerical diffusion [48]. Applied upwind-difference scheme, the neighboring points coefficients in Eq. (3.34) can be expressed as [48]

$$\begin{aligned}
a_S &= D_s + max(+F_s, 0) \,, \\
a_N &= D_n + max(-F_n, 0) \,, \\
a_W &= D_w + max(+F_w, 0) \,, \\
a_E &= D_e + max(-F_e, 0) \,, \\
a_B &= D_b + max(+F_b, 0) \,, \; and \\
a_T &= D_t + max(-F_t, 0) \,.
\end{aligned} \tag{3.36}$$

Where F and D are the convective mass and diffusive fluxes at the cell faces, respectively. They can generally be expressed as

$$F = (\rho u)\Delta A \quad and \quad D = \frac{\Gamma}{\delta_x}\Delta A \,. \tag{3.37}$$

Here, δ_x is the distance between the center-point node to the cell face and ΔA is the area of the cell face. For the eastern face of the control volume, for example, the convective mass and diffusive fluxes can be expressed as

$$F_e = (\rho u)_e \Delta y \Delta Z \quad and \quad D_e = \frac{\Gamma_e}{(\delta_x)_e}\Delta y \Delta z \,. \tag{3.38}$$

The diffusion term, Γ_ϕ, in Eq. (3.31) is stored in the nodal points (•) (see Fig. 3.3). In the `KFX-EXSIM` explosion model a harmonic mean is used to estimate the diffusion flux at the cell faces. Considering grid point W and P, see Fig. 3.3, the diffusion flux at cell face w is calculated as follows:

$$\Gamma_{\phi,w} = \frac{2\Gamma_{\phi,W}\Gamma_{\phi,P}}{\Gamma_{\phi,W}\Gamma_{\phi,P}} \tag{3.39}$$

3.6.3 Solution algorithm

The set of non-linear algebraic equations obtained from the discretization of the transport equation discussed previously are solved using the well know Thomas algorithm or the tri-diagonal matrix algorithm (TDMA). This algorithm is a direct method for 1D (one-dimensional) problems, while it can be applied iteratively in a line-by-line trend [48] for 2D and 3D problems. The SIMPLE (Semi-Implicit Method for Pressure-Linked Equations) algorithm is used to handle the pressure and velocity coupling of the three momentum and conservation of mass equations. The main idea of the SIMPLE algorithm is to correct a preliminary guessed (initial values for the first iterations) pressure and velocity such that the conservation of mass equation at the next time step is fulfilled. The decoupling of the pressure and the velocity components can be expressed as follows [48, p. 187]:

$$p = p^* + p' \,, \tag{3.40}$$

$$u = u^* + u' \,, \tag{3.41}$$

$$v = v^* + v' \,, \tag{3.42}$$

$$w = w^* + w' \,, \tag{3.43}$$

where * denotes the preliminary guess and $'$ represents the correction. Pressure and velocity correction can be obtained by subtracting the preliminary guess from the correct value.

The SIMPLE algorithm was developed by Patanker and Spalding [49] and was extended by Hjertager [50] to handle the density, pressure, and velocity coupling of the three momentum and continuity equations, i.e. to handle compressibility.

3.6.4 Boundary and initial conditions

- Boundary conditions: In the `EXSIM` gas explosion model, the fixed pressure boundary condition is used for open boundaries. This boundary allows both inflow and outflow. According to the work of Saeter [11] and the `KFX-EXSIM` manual [41], the boundary conditions must be defined as far from the combustible zone as possible to avoid the effect of the boundary solution, e.g. non-physical pressure reflection, on the solution of the domain of interest.

- Initial conditions: In the explosion model of `KFX-EXSIM`, the initial value of 10^{-3} is used for the turbulence quantities, k and ε [11], since initially both are assumed to be quiescent. All the velocity components also are initially assumed to be quiescent

- Ignition: A fraction of the product is used at the predefined ignition cells to initializing ignition. This product gives a temperature rise and decrements in density. Hence, the unburned gas start flows in front of the flame, and the laminar combustion process is initialized. The initial specified burning velocity is then provided by the laminar combustion model, see Section 3.5.1.

Chapter 4

Simulation Case 1 - A premixed hydrogen-air explosion in a vertical rectangular chamber : effect of obstacle position on overpressure

An experiment involving a premixed hydrogen-air explosion in a rectangular 5×10^{-3} m^3 duct containing an obstacle in a different position was conducted by Xianshu et al. [12]. The objective of the experiment was to investigate the effect of the obstacle position and equivalence ratio on overpressure. Hence, equivalence ratios of 0.6, 0.8, 1.0, 1.2, and 1.4 along with a single obstacle at the different positions were used. However, only the effect of the obstacle position on the overpressure of the stoichiometric premixed hydrogen-air mixture explosion was investigated in the simulations. The small scale gas explosion experiment mentioned above was simulated to evaluate the ability of `KFX-EXSIM` and `XiFoam` codes to simulate a gas explosion. The simulation results were compared to the experimental data with regard to the overpressure/gauge pressure profile, the peak overpressure, and the flame propagation speed. The experimental setup details and the simulation procedures used to reproduce the gas explosion experiment mentioned above are presented in Section 4.1 and Section 4.2, respectively. Section 4.3 presents simulation results in comparison with the experimental data. The brief discussion on the results obtained in Section 4.3 is presented in Section 4.4.

4.1 Experimental Details

The rectangular duct used to perform the gas explosion experiment had a cross-section of 0.1 $\times$ 0.1 m^2 and a height of 0.5 m. The bottom end of the tube was closed by a steel plate; and the pressure sensor, an ignition source, and a gas inlet located on it. The ignition was electronic type activated by 6V DC voltage and located at the center of the bottom end of the tube. The pressure sensor used to measure the explosion overpressure was a Kellet type PR-23 piezoresistive pressure sensor, which measured the static pressure with a range from -1.0 to 1.5 bar (with a total error $<$0.25%). It was located at 20 mm from the ignition position. The top end of the tube was sealed using a thin PVC membrane that ruptured at low pressure when the explosion occurred. The tube walls were constructed using a 20 mm thick `Perspex` material. Fig. 4.1 shows the schematic diagram of the experimental setup, including the data acquisition system.

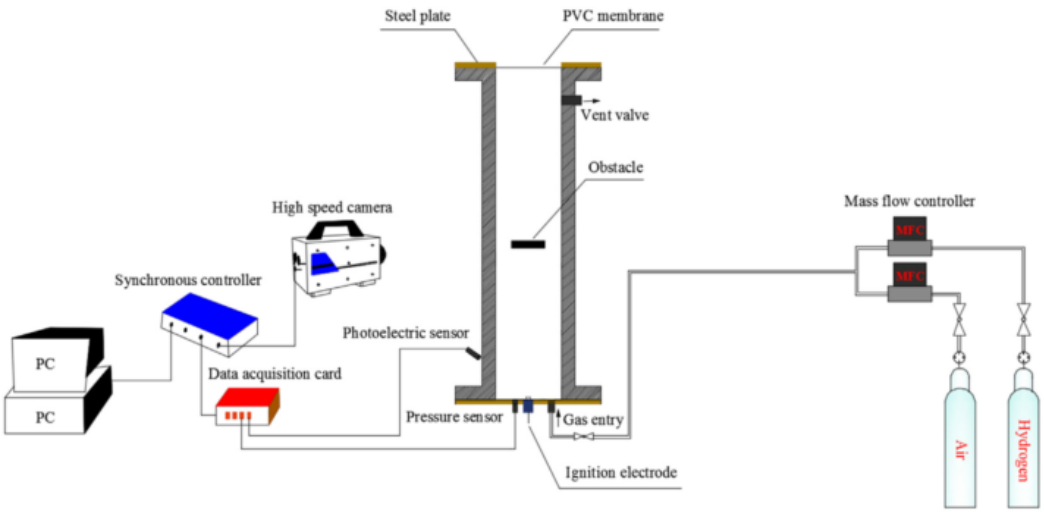

Figure 4.1: The schematic diagram of the experimental setup for the premixed hydrogen-air mixture explosion, adapted from [12].

The obstacle with a cross-section of $0.1 \times 0.05\ \mathrm{m}^2$, which gives a blockage ratio of 50%, and a height of $0.01\ \mathrm{m}$ was installed inside the tube at various positions. The experiments were performed for four experimental configurations in terms of the obstacle positions. The four experimental configurations of the tube are shown in Fig. 4.2. Configuration 1 represents the experimental configuration without an obstacle, while Configurations 2–4 represent the experimental configurations with an obstacle located at $0.1\ \mathrm{m}$, $0.2\ \mathrm{m}$, and $0.3\ \mathrm{m}$ from the bottom end of the duct, respectively.

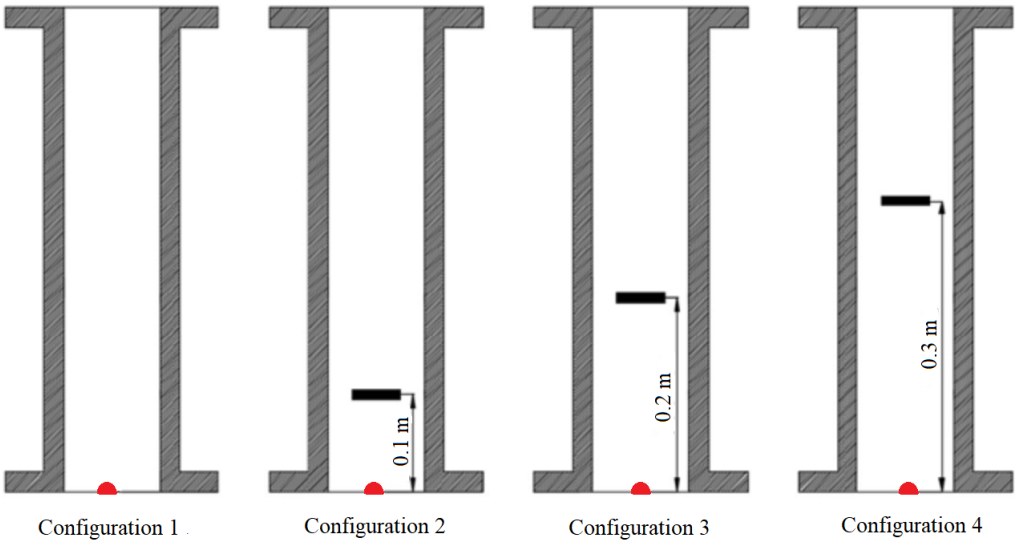

Figure 4.2: The 2D view of the four experimental configurations. The red dot at the bottom of the tube shows the location of the ignition source, adapted from [12].

In the experiment, a homogeneous hydrogen-air mixture with equivalence ratios ranging from 0.6–1.4 was used. However, only the stoichiometric hydrogen-air mixture used in the simulations. The experiments were conducted under ambient conditions, but the initial pressure

and temperature values were not given. Information about air humidity was not presented in the experiment [12]. The hydrogen-air mixture inside the duct was allowed to settle for 15 s before ignition. More information about the experimental setup can be found in [12].

4.2 Simulation setup

The experiment mentioned in Section 4.1 was reproduced numerically using KFX-EXSIM and XiFoam. The simulation setup used in both KFX-EXSIM and XiFoam is presented in the next two sub-sections.

4.2.1 KFX-EXSIM

In KFX-EXSIM code, the expansion outside the explosion duct was also considered. Therefore, the entire computational domain was subdivided into two domains, such as the explosion duct and the one enclosing the duct. The duct geometry was created using the 3D tools CAD package of KFX-EXSIM, called "Doozer" and is shown in Fig. 4.3. The wall is considered as smooth since no information was given in [12]. The domain of the explosion duct has dimensions of $0.1 \times 0.1 \times 0.5$ m. The use of the outside domain, i.e the volume that enclosed the explosion duct, has two main purposes, such as (i) capturing the venting of the burnt gas, (ii) capturing the expansion outside the explosion duct. The fixed pressure with the value of 1 bar is applied to the open boundaries (i.e. the boundaries of the outside domain). Hence, in order to reduce or eliminate the non-physical pressure reflections from the open boundaries into the domain of the explosion duct, the outside domain boundaries must be defined far away from the explosion duct, especially in the flow direction. Therefore, the open boundaries were located at 10 m away from the open end of the explosion duct, i.e in the z direction, and 2 m in both x and y directions. Therefore, the volume enclosing the explosion duct was $2 \times 2 \times 10$ m^3.

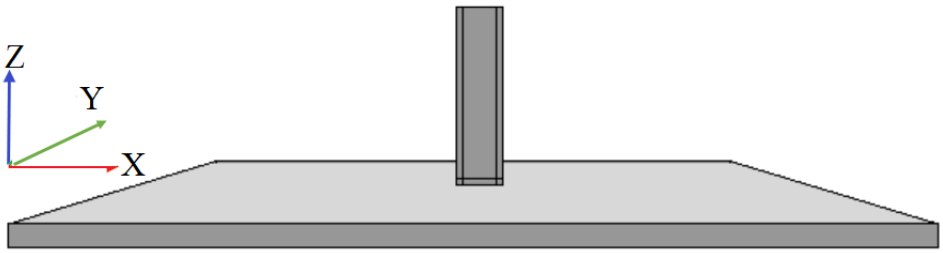

Figure 4.3: View of the duct geometry including the ground.

The automatic grid generation options of KFX-EXSIM was not used, since the size of the geometry of the explosion duct is too small for the automatic grid generation option of KFX-EXSIM. So, the number of cells in each direction of the interior of the explosion duct was defined manually based on the recommendation given in the KFX-EXSIM user manual [41]. The explosion domain consists of 10 cells in x and y directions and 50 cells in the z direction. They are distributed uniformly in the volume of the explosion chamber giving a Cartesian grid with a cell size of 10 mm. This grid size gave two and half cells at the openings around the obstacle, i.e. half of a cell is covered by the obstacle, however, this can handle properly using

a PDR concept, see Section 3.2. The grid was expanded from the explosion tube towards the open boundaries by 10%. The inner volume of the explosion tube had a total of 5000 cells, while the total computational cells were 415,152. Fig. 4.4 shows the mesh distribution within the explosion tube and the external domain.

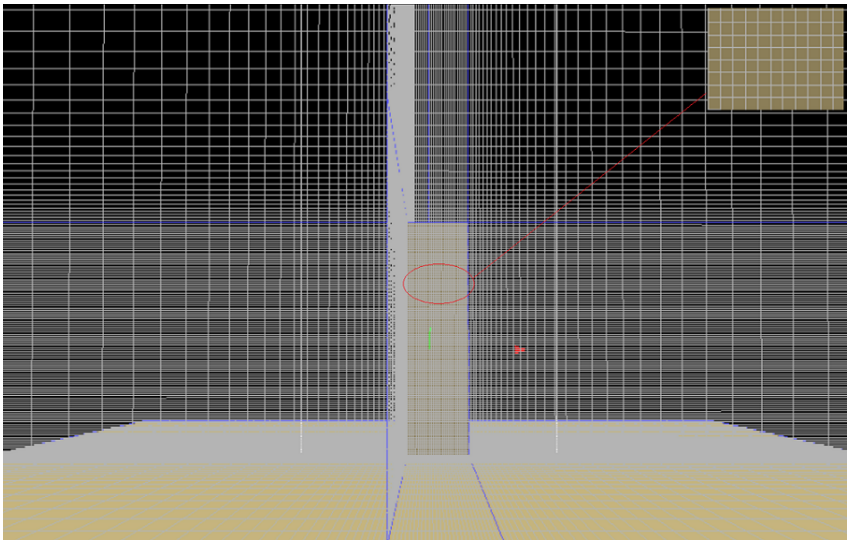

Figure 4.4: The distributions of the computational cells inside the explosion tube and the volume enclose the tube.

Table 4.1: Initial conditions of some variables

Variable	Unit	value
Velocities	$\mathrm{m\,s^{-1}}$	0
Pressure	bar	1
Temperature	K	293
Turbulence kinetic energy	$\mathrm{m^2\,s^{-2}}$	0.001
Dissipation of kinetic energy	$\mathrm{m^2\,s^{-3}}$	0.001
Initial laminar burning velocity	$\mathrm{m\,s^{-1}}$	3.5

The initial gas composition was a stoichiometric premixed hydrogen-air, in which the air was assumed to be composed of 21% oxygen and 79% nitrogen. The ignition was modeled as the ”single wall” type located in the middle of the bottom side of the explosion tube. The ruptured pressure of the PVC membrane (i.e. the top end of the tube) was assumed to be 0.1 mbar. The top end of the tube was modeled as a blast panel, where the whole cells open when the average pressure exceeds the minimum ruptured pressure. The maximum Courant number of 1, based on both the flow velocity and speed of sound, was used. The no-slip wall boundary condition was employed on the walls of the explosion tube and the bottom side of the volume enclosed the chamber, i.e the ground. The fixed pressure boundary condition with the value of 1 bar was applied to the open boundaries (i.e the boundaries of the outside domain). Table 4.1 shows the initial values of different variables used in the simulations. The value of

the ratio between activation energy E and universal gas constant R, E/R, was 9.13×10^3. The value of 2.25×10^{-11} was used for the inverse of the pre-exponential factor, A_{ch}. These values were used to calculate the chemical time scale, see Eq. (3.30). In addition, a logarithmic wall law [18, p. 72]

$$u_1^+ = \frac{1}{\kappa}\ln Ex_2^+ \ , \tag{4.1}$$

was used in the KFX-EXSIM code for no-slip wall condition, where u_1^+ and x_2^+ are the dimensionless mean velocity and distance from the well, respectively. The values of 0.42 and 9.0, respectively, used for the constant E and the von Kármán's constant κ.

4.2.2 XiFoam

The explosion experiment described in Section 4.1 was also numerically mimiced using XiFoam, which is a solver for the premixed and partial premixed combustion with turbulence modeling [51]. This code is a part of the OpenFOAM (open source Field Operation And Manipulation) toolbox, which is an open source package used to resolve CFD problems using finite volume discretization. In this code, the mass-weighted conservation equation of mass, momentum, and energy are solved in addition to the equation of state, i.e ideal gas law. The heat flux in the energy equation was modeled according to Fourier's law, i.e the Dufour effect is neglected.

The combustion model used was the Weller $b-\Xi$ flame surface wrinkling combustion model, Eq. (2.56) (see Section 2.3.4). Flame burning velocity, also known as the turbulence flame speed, was modeled as the product of the sub-grid flame wrinkling factor Ξ and the laminar flame speed S_L, which was modeled by Eq. (2.39), see Section 2.3.1. The unstrained flame speed, S_L^o, in Eq. (2.39) was calculated using the empirical expression proposed by Gülder [28], Eq. (2.40) with the Gülder coefficients for hydrogen

$$W = 2.094\mathrm{m\,s^{-1}} \ , \qquad \xi = 1.068 \ , \qquad \alpha = 2.9 \ , \quad and \qquad \beta = -0.04 \ . \tag{4.2}$$

The sub-grid flame surface wrinkling factor Ξ was computed using the transport equation given by Eq. (2.57), see Section 2.3.4. The viscosity of the mixture (in XiFoam, the fuel-air mixture considered as one species), which is used to calculates the turbulence Schmidt number in Eq. (2.56), was obtained by the Sutherland law and can be expressed as

$$\mu = A_s\frac{T^{1/2}}{1+T_s/T} \ , \tag{4.3}$$

where A_s and T_s are the Sutherland coefficients and have the values of 1.67212×10^{-6} and 170.672, respectively, for both the reactants and products.

The thermodynamic properties heat capacity and enthalpy are can be provided using NASA polynomials. In XiFoam, the NASA polynomials are represent the thermodynamics data for two temperature ranges, a lower and higher temperature range. In addition, the NASA polynomial in XiFoam represents the fuel and oxidizer mixture as one species, i.e as reactant, and the same for the combustion products as well, i.e they regarded as one species. The reactant and products heat capacity and enthalpy have the form
for lower temperature range ($T_i \le T \le T_c$):

$$\begin{aligned} \frac{C_p}{R} &= a_1 + a_2T + a_3T^2 + a_4T^3 + a_5T^4 \ , \\ \frac{H}{R} &= a_1 + \frac{a_2}{2}T + \frac{a_3}{3}T^2 + \frac{a_4}{4}T^3 + \frac{a_5}{5}T^4 + \frac{a_6}{T} \ , \end{aligned} \tag{4.4}$$

for higher temperature range ($T_c \geq T \geq T_m$):

$$\begin{aligned} \frac{C_p}{R} &= a_8 + a_9 T + a_{10} T^2 + a_{11} T^3 + a_{12} T^4 \ , \\ \frac{H}{R} &= a_8 + \frac{a_9}{2} T + \frac{a_{10}}{3} T^2 + \frac{a_{11}}{4} T^3 + \frac{a_{12}}{5} T^4 + \frac{a_{13}}{T} \ , \end{aligned} \tag{4.5}$$

where T_c is a common temperature as named in the `XiFoam` code, T_i is the lower temperature, and T_m is the higher temperature. The values of the coefficients were automatically generated using the `OpenFOAM` utility called "`adiabaticFlameT`" for equivalence ratio of 1.0. The values are based on the CHEMKIN thermodynamic data base.

The standard $k - \varepsilon$ model, Eq. (2.34) and Eq. (2.35) (see Section 2.2.5), with the model constants from Launder and Spalding [23], see Eq. (2.37), is implemented as a turbulence model. Among many numerical schemes for the time integration and convection term available in `OpenFOAM`, the first-order implicit bounded Euler is applied for the time integration and the 'Gauss limitedLinear 1' and/or 'Gauss limitedLinearV 1', as named in `OpenFOAM`, are implemented for the convection terms. These convection schemes are the second-order bounded Gauss method with a flux limiter function that limits towards upwind in the rapidly changing gradient regions [52]. The pressure and velocity coupling of the momentum and mass conservation equations were handled using PIMPLE algorithm, which is the combination of PISO (pressure-implicit split-operator) and SIMPLE algorithm.

The simulations were performed without considering the expansion that occurred outside the explosion tube. Hence, the mesh was only generated for the explosion tube using the `OpenFOAM` utility called "`BlockMesh`". The computational domain consists of 40, 200, and 40 cells in x, y, and z directions. The grids were distributed uniformly in the explosion tube giving Cartesian grids with a size of 2.5 mm. This gives 320,000 cells in total. The mesh distribution within the explosion tube is shown in Fig. 4.5.

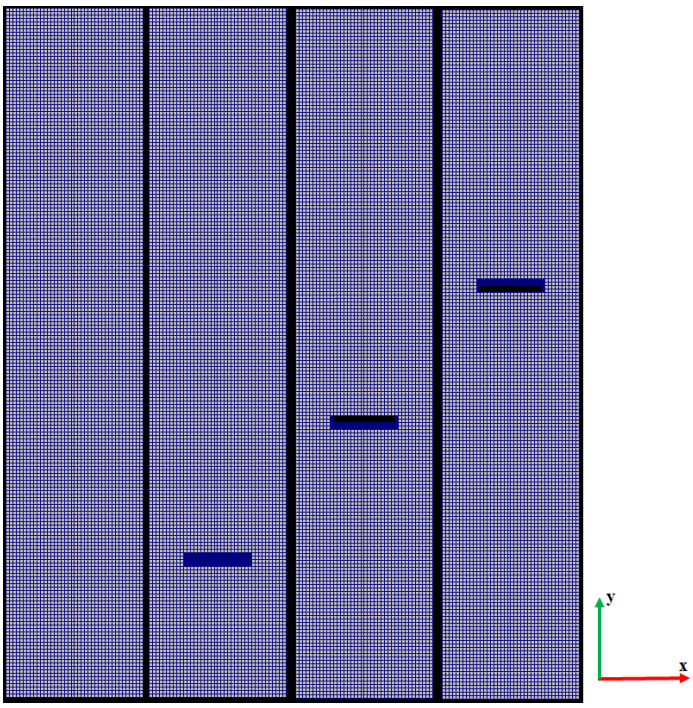

Figure 4.5: The mesh distribution inside the explosion chamber. left to right: Configurations 1–4. Positive z-direction is into the image plane.

The Courant number (C) of 0.2 was used in the simulation, and the time step is calculated based on the local flow velocity and grid size (δx), i.e. $\delta t = \mathrm{C} \cdot \delta x / U$. The computational domain has two boundaries (they are called "patches" in `OpenFOAM`), namely walls and open. For the walls, the non-slip velocity boundary condition was applied. In the `XiFoam`, the PVC membrane at the top side of the explosion chamber was modeled as fully open. At the open end of the tube, the '`totalPressure`' and '`inletOutlet`' boundary conditions were used for pressure and velocity, respectively. For the temperature, the '`zeroGradient`' and the '`inletOutlet`' with the value of 293 K were applied at the walls and the open end of the tube, respectively. The "epsilonWallFunction" with the values of 0.41 and 9.8 for Von Kármán constant κ and model coefficient *E* was applied for the rate of dissipation of turbulence kinetic energy, ε. While the "kqRWallFunction" was used for the turbulence kinetic energy k. The initial value of 0.001 $\mathrm{m^2\,s^{-2}}$ for k and 0.001 $\mathrm{m^2\,s^{-3}}$ for ε was used. The detailed boundary conditions selected for different variables at each boundary are presented in Table 4.2.

As described in the experiment, a stoichiometric premixed hydrogen-air mixture was used in the simulations. The initial laminar flame speed was 3.5 $\mathrm{m\,s^{-1}}$. Before ignition, all velocity components and turbulence parameters are assumed to be passive. Hence, the initial value of 0 $\mathrm{m\,s^{-1}}$ was used for the velocity components. The initial value of 293 K for the temperature and 1 bar for the pressure was used in the simulation. The "point source" ignition at the center of the bottom end of the tube with a diameter of 1 mm and the duration of 3 ms was applied.

Table 4.2: Boundary conditions, the values, i.e. inflow value for the case to return flow, for '`inletOulet`' boundary conditions are the same with the initial values of the variable.

Variable	walls	open
Dissipation rate of the turbulence energy, [$\mathrm{m^2\,s^{-3}}$]	`epsilonWallFunction`	`inletOutlet`
The turbulence kinetic energy, [$\mathrm{m^2\,s^{-2}}$]	`KqRWallFunction`	`inletOutlet`
Velocity, [$\mathrm{m\,s^{-1}}$]	`noslip`	`inletOutlet`
Temperature, [K]	`zeroGradient`	`inletOutlet`
Pressure, [$\mathrm{kg\,m^{-1}\,s^{-2}}$]	`zeroGradient`	`totalPressure`
Regress variable, [-]	`zeroGradient`	`zeroGradient`
Laminar flame speed, [$\mathrm{m\,s^{-1}}$]	`zeroGradient`	`inletOutlet`
The flame-wrinkling S_t/S_u, [-]	`zeroGradient`	`inletOutlet`

All the `XiFoam` simulations were performed in parallel on distributed processors using a supercomputer called '`Vilje`', using 4 nodes and 16 standard message passing interface (MPI) processors which gives a total of 64 processors. The supercomputer `Vilje` has 1404 nodes, 2 eight-core processor per node and 16 cores per node, which `OpenFOAM` installed on it [53]. In order to run the simulations on `vilje` in parallel, the mesh and associated fields must be broken into pieces and distributed to a number of processors using a domain decomposition method.

4.2.3 Sensitivity Analyses

To investigate the effect of grid size and Courant number on the simulation results, several simulations were performed using both KFX-EXSIM and XiFoam. To see the dependency of the simulation results on the grid size, simulations for finer and coarser meshes with cell sizes of 2.5 and 10 mm were performed in the XiFoam, while finer meshes with grid sizes of 5 and 2.5 mm were tested in KFX-EXSIM. The maximum Courant number of 0.2 and 1.0 was used in XiFoam and KFX-EXSIM, respectively. To investigate the effect of the Courant number (in other words, time steps), simulations were performed for the grid size of 2.5 mm in the XiFoam and 10 mm in the KFX-EXSIM for the maximum Courant numbers of 0.2–1.0. All the simulation setting, boundary conditions, and initial conditions are the same as mentioned earlier. The results of the simulations are presented in Section 4.3 and discussed in Section 4.4.

4.3 Results

This sub-section presents the numerical simulation results for the experimental case described in Section 4.1. The simulation focused mainly on the flame propagation speed, overpressure evolution, and the overpressure magnitude, i.e. the peak overpressure, inside the explosion chamber. The results of the simulations were compared with the experimental results to validate the simulation.

Figures 4.6–4.9 show the flame structure and flame propagation image inside the chamber for Configurations 1–4, respectively, as obtained from the experiment and the XiFoam simulations. The figures found from the simulation was made using the iso-surface value of 1500 K (the iso-surface values ranging from 1100–1800 K gives almost the same figures). Here, these figures only used for looking at the flame propagation. Because of the KFX-EXSIM post-processing problem, the results from the KFX-EXSIM simulations regarding the flame structure and flame propagation speed are not presented here. Although many tests were performed (in cooperation with the expert who works on this code at DNV GL - plant CFD solution AS), the problem was not known.

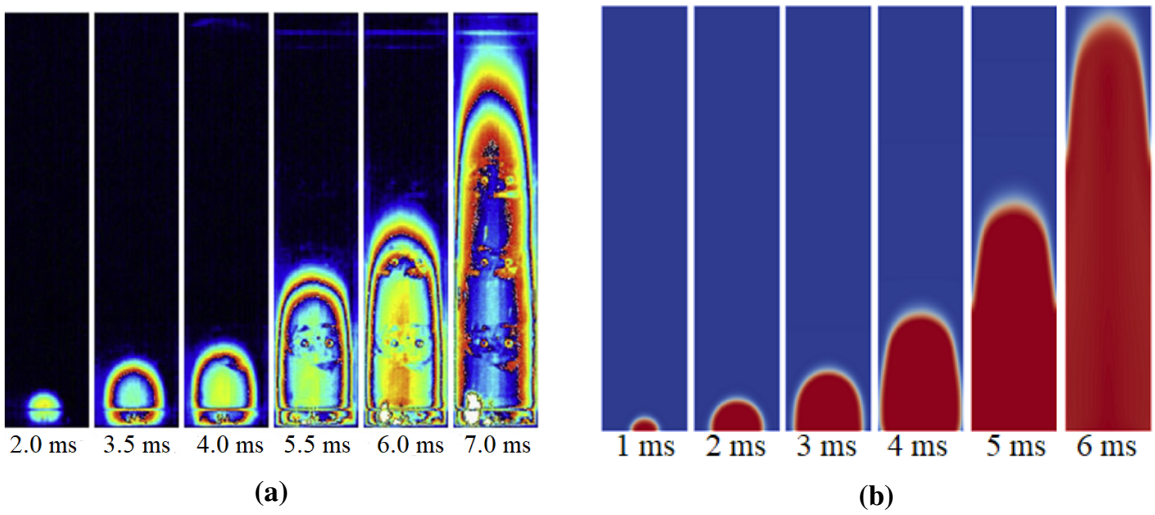

Figure 4.6: Flame structure and flame propagation in Configuration 1. (a) Experimental data [12] and (b) simulation result from XiFoam.

The figures show that the numerical results, which were obtained from the `XiFoam` simulations, are consistent with the experimental results. However, there was some time shift. Initially, the flame shape in all configurations was similar and changes differently during the explosion. It can be noticed that, from both experimental and numerical results, initially, the flame was laminar and hemispherical and even similar for all configurations. The structure of the flame was different for each configuration due to the presence of the obstacle at a different location. For Configuration 1, the flame propagates hemispherically and finger shape. While, because of the presence of an obstacle in Configurations 2–4, the flame front becomes slightly flat when moving closer to the obstacle and formed two symmetrical flames on both sides of the obstacle. For Configurations 2–4, according to the flame propagation images and the overpressure profiles, as presented in Fig. 4.12, the peak overpressure corresponds to the merging of the two symmetrical flames.

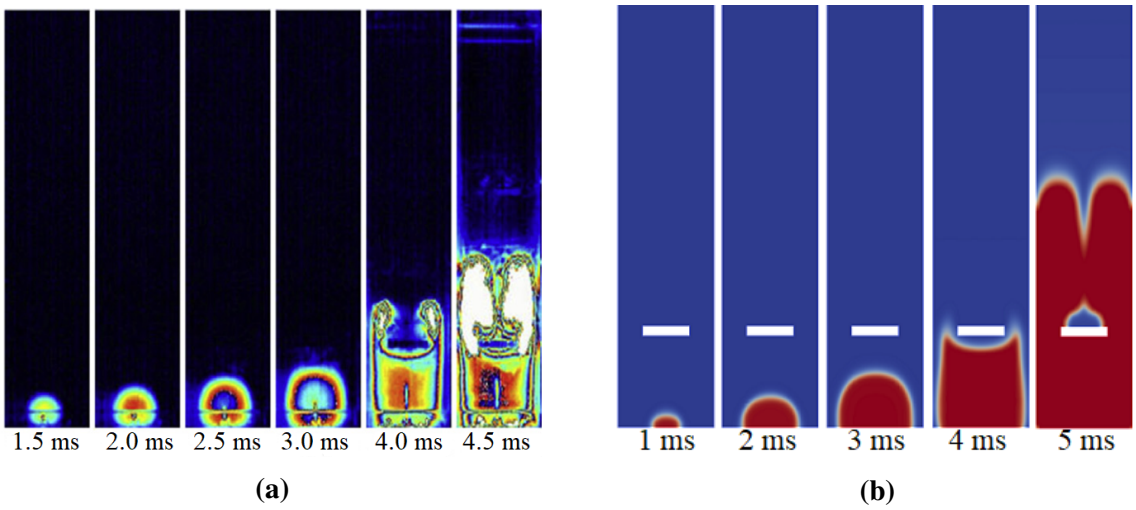

Figure 4.7: Flame structure and flame propagation in Configuration 2. (a) Experimental data [12] and (b) simulation result from `XiFoam`.

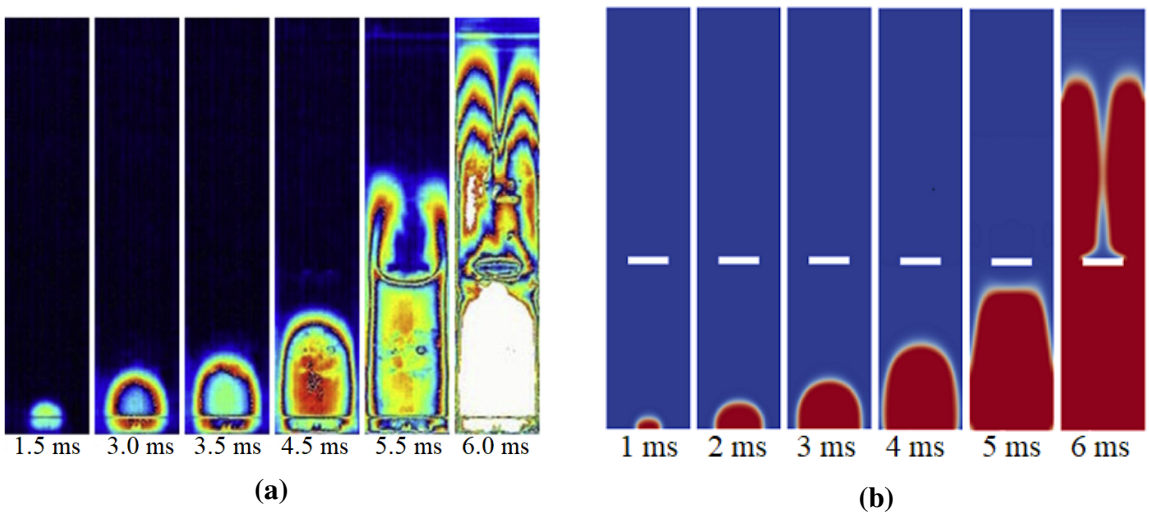

Figure 4.8: Flame structure and flame propagation in Configuration 3. (a) Experimental data [12] and (b) simulation result from `XiFoam`.

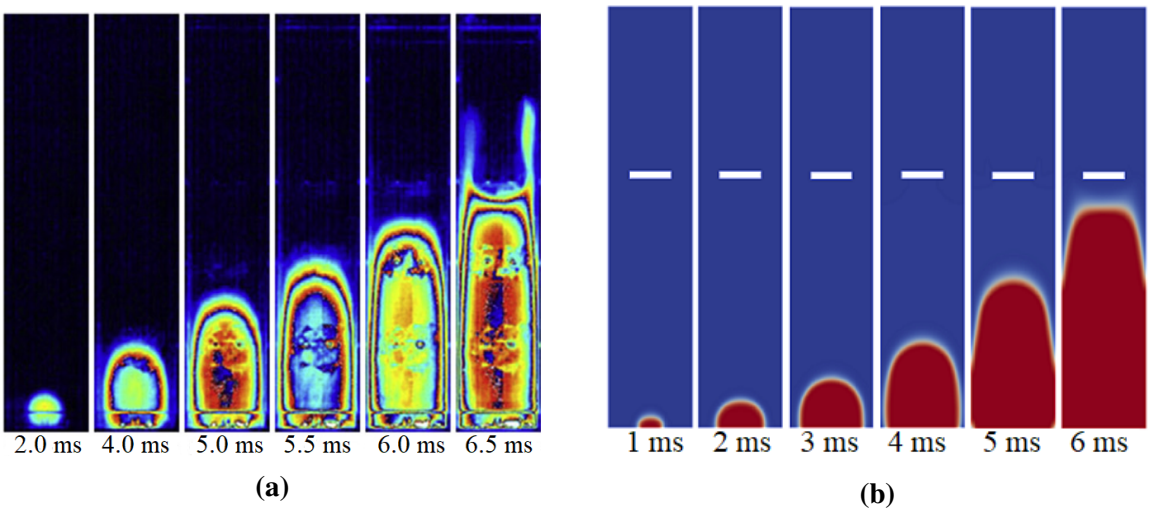

Figure 4.9: Flame structure and flame propagation in Configuration 4. (a) Experimental data [12] and (b) simulation result from `XiFoam`.

The flame front position and flame propagation speed (see Section 2.3.1) versus time, as obtained from the experiment and `XiFoam` simulations, are shown in Fig. 4.10 and Fig. 4.11, respectively. In the experiment, the flame front captured using the high-speed digital camera at different locations, while in the simulation, it was visualized manually using a post-processing tool of `OpenFOAM`. Comparing the `XiFoam` simulation results with the experimental data, it can be noticed that the simulations were in reasonably good agreement with experimental results except some time shift. The results also show that the flame propagated faster in the simulation than in the experiment for Configurations 2–4, while slower in the simulation compared to the experimental data for Configuration 1.

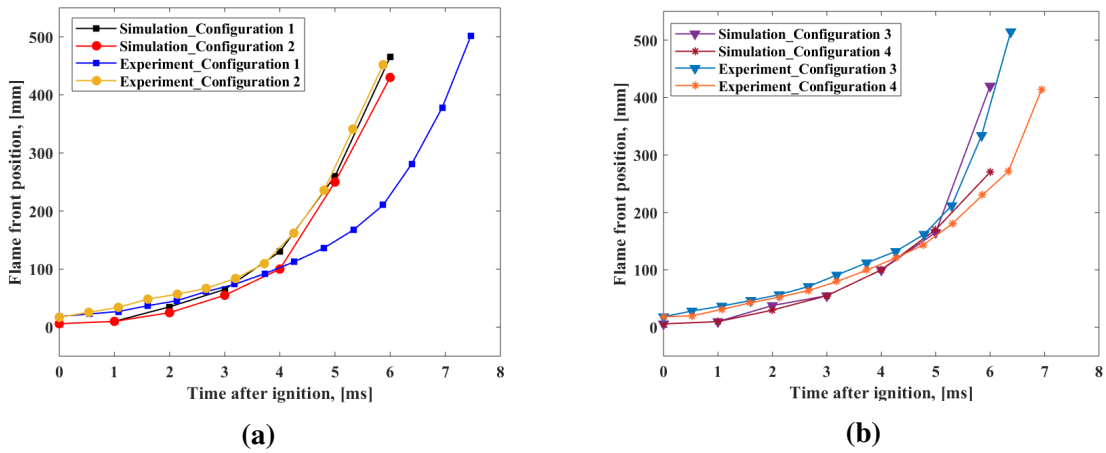

Figure 4.10: Flame front position versus time from experimental data [12] and `XiFoam` simulation. (a) Configurations 1 and 2; Configurations 3 and 4.

Regarding the flame propagation speed, the simulation results are consistent with the experimental data, as presented in Fig. 4.11. As shown in Fig. 4.11, for configuration 2-4, the flame propagation speed decreased first when the flame starts to feel the presence of the obstacle and start accelerated when the flame passed over the obstacle due to distortions and turbulence generated behind the obstacle. Thus, it can be concluded that the presence of the obstacle leads to

the increase of the flame speed, even if the flame speed slows down for a short while.

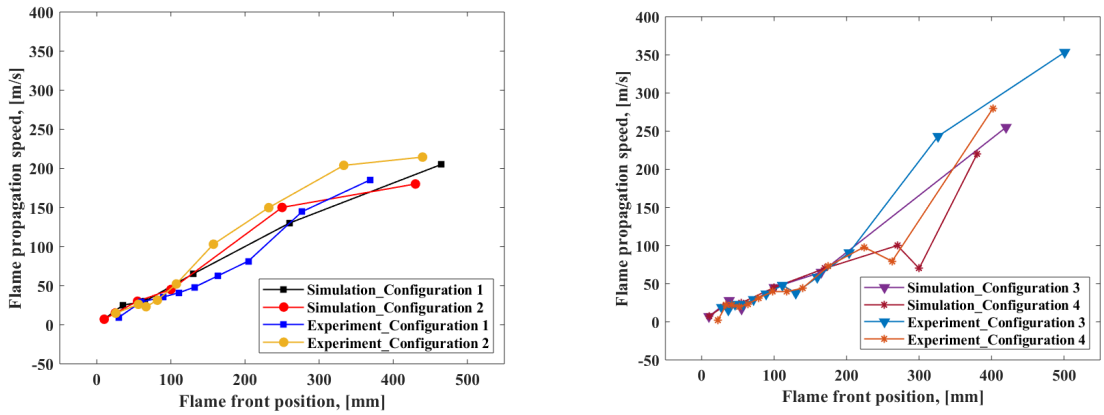

(a) **(b)**

Figure 4.11: Flame propagation speed as a function of position from the experimental data [12] and `XiFoam` simulation. (a) Configurations 1 and 2; (b) Configurations 3 and 4.

Fig. 4.12 shows the evolution of the overpressure inside the chamber for Configurations 1–4. These results were found for the grid size of 10 mm and Courant number of 1 in the `KFX-EXSIM` and the grid size of 2.5 mm and Courant number of 0.2 in the `XiFoam`.

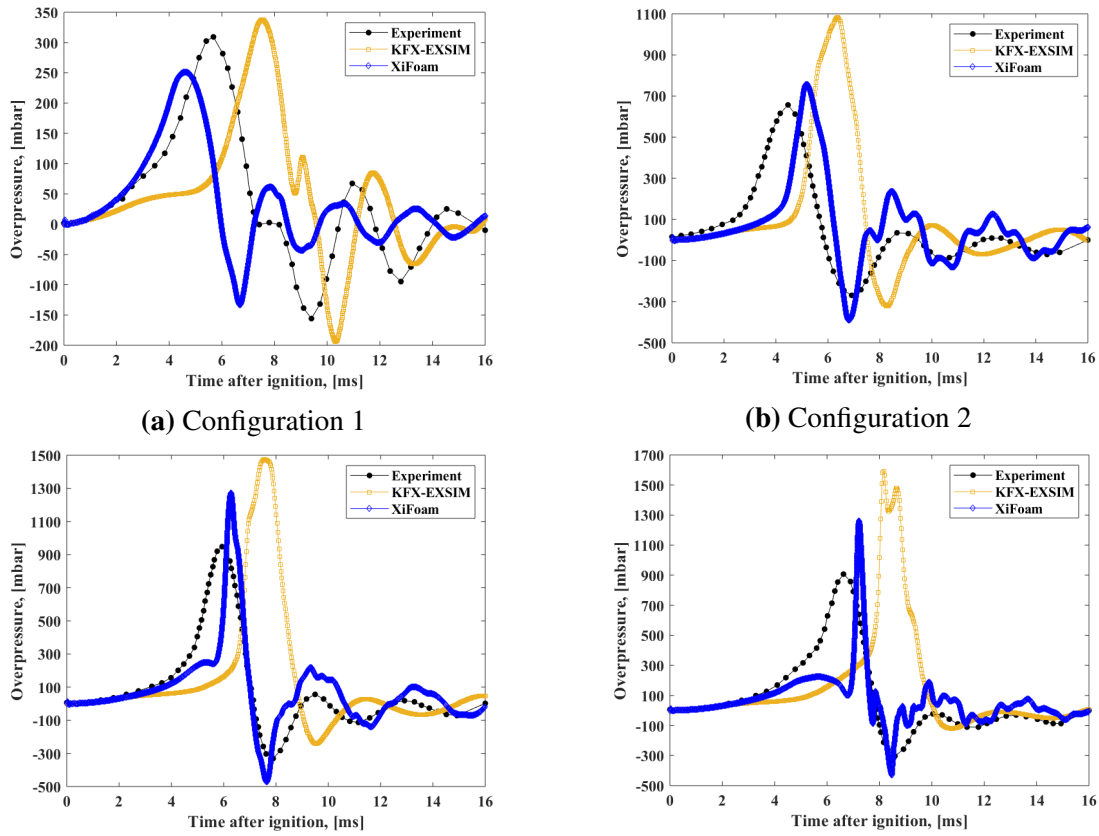

(a) Configuration 1 **(b)** Configuration 2

(c) Configuration 3 **(d)** Configuration 4

Figure 4.12: Overpressure in four configurations for the equivalence ratio $\phi = 1.0$.

As shown in Fig. 4.12a, regarding the peak overpressure, the simulations were in reasonably good agreement with the experimental data for configuration 1. The peak overpressure was underestimated by approximately 19% in the `XiFoam`, while overestimated by around 8.8% in the `KFX-EXSIM`. In the `XiFoam`, the peak overpressure was obtained at $t = 4.5$ ms which was occurred earlier, by 1.1 ms, compared to the experimental data. In contrarily, in the `KFX-EXSIM`, the occurrence time of the peak overpressure was delayed by 1.94 ms compared to the experimental data.

For Configuration 2, as shown in Fig. 4.12b, the peak overpressure was overestimated by around 11.9% and 64% in the `XiFoam` and `KFX-EXSIM`, respectively. Fig. 4.12b also shows that the occurrence time of the peak overpressure was delayed compared to the experimental data in both codes. The peak overpressure obtained in the simulation was delayed by approximately 0.58 ms in the `XiFoam`, while by around 1.83 ms in the `KFX-EXSIM`. For configuration 3, as seen in Fig. 4.12c, the simulation results obtained from both `XiFoam` and `KFX-EXSIM` gave an overestimation of the peak overpressure by around 31.2% and 55.4%, respectively. As shown in Fig. 4.12c, the occurrence time of the peak overpressures in the simulations was delayed by 0.33 ms in the `XiFoam` and 1.68 ms in the `KFX-EXSIM` as compared to the experimental data. For Configuration 4, as presented in Fig. 4.12d, the peak overpressures obtained in `XiFoam` and `KFX-EXSIM` simulations were overestimated by approximately 35.6% and 74.8%, respectively. In `XiFoam`, the peak overpressure was obtained at $t = 7.2$ ms which was delayed by 0.6ms from the experimental data, as described in Fig. 4.12d. While, the peak overpressure was obtained at $t = 8.14$ ms, which is delayed by around 1.54 ms as compared to the experimental data, in `KFX-EXSIM`.

Grids and Time steps Sensitivity Analysis Results:

The overpressure profiles inside the explosion tube for the grid sizes of 2.5, 5, and 10 mm in Configurations 1 and 2, as obtained from the `KFX-EXSIM`, are presented in Fig. 4.13 (Fig. 4.12a and Fig. 4.12b also shows the results for 10 mm). As shown in Fig. 4.13, with an increase in grid size, the peak overpressure tends to be decreased and delayed. It can be noticed that when the mesh becomes coarser, the simulation was in relatively good agreement with the experimental data regarding the peak overpressure for Configurations 1 and 2. However, the occurrence time of the peak overpressure tends to be delayed more.

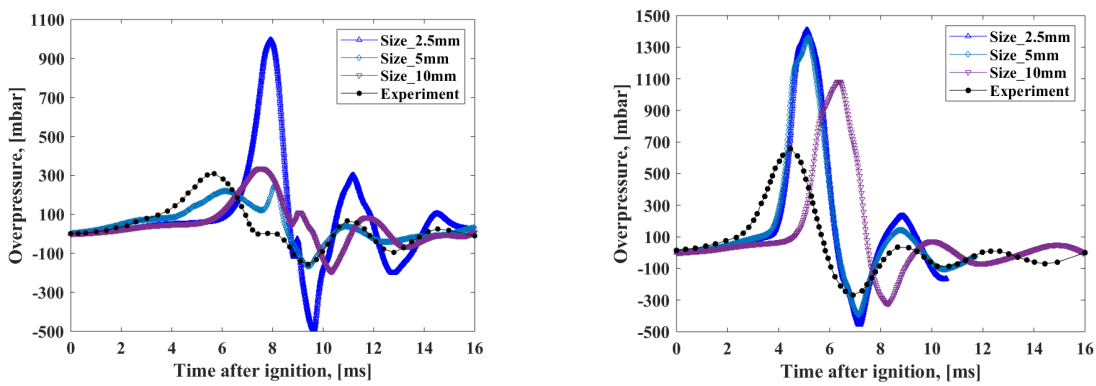

(a) Configuration 1 **(b)** Configuration 2

Figure 4.13: Overpressure in configuration 1 and configuration 2, which is obtained in `KFX-EXSIM`, for the grid size of 10, 5, and 2.5 mm

Fig. 4.14 shows the overpressure profiles inside the explosion tube for the grid sizes of 2.5, 5, and 10 mm in Configuration 1 and 2, as obtained from the XiFoam. As shown in Fig. 4.14, the peak overpressure tends to be increased and occurred earlier, when the grid size increased (i.e becomes coarser). Unlike the simulation results from KFX-EXSIM, where the numerical results relatively agreed with the experimental data for the coarser mesh, the XiFoam simulations results were in good agreement with the experimental results when the mesh becomes finer.

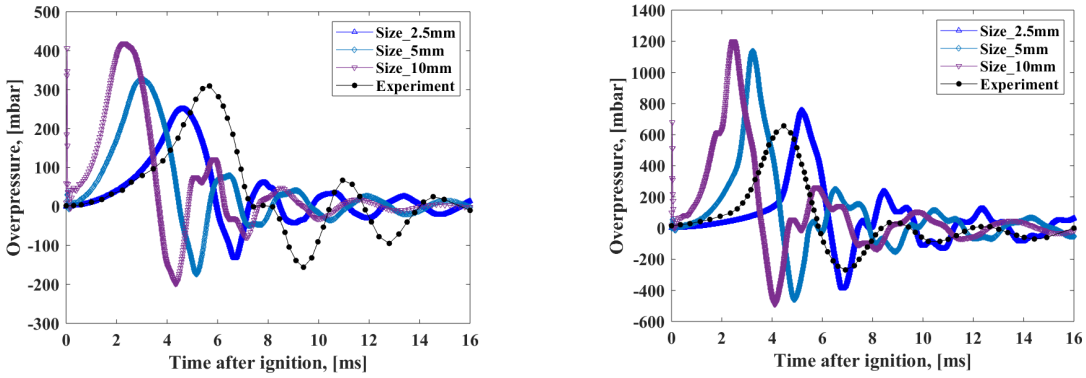

(a) Configuration 1 **(b)** Configuration 2

Figure 4.14: Overpressure versus time for Configuration 1 and 2, as obtained from XiFoam, for the grid sizes of 10, 5, and 2.5 mm

Fig. 4.15 shows the overpressure profiles inside the explosion tube for the grid sizes of 10 mm and for the various maximum Courant numbers ranging from 0.2–1.0 in Configurations 1 and 2, as obtained from the KFX-EXSIM. With increases the maximum Courant number from 0.2 to 1, the peak overpressure tends to be decreased and relatively agreed with the experimental results, as presented in Fig. 4.15. The figure also shows that the Courant number affected more the magnitude of peak overpressure than it's occurrence time, unlike the grid size, which affected both the magnitude and occurrence time of the peak overpressure.

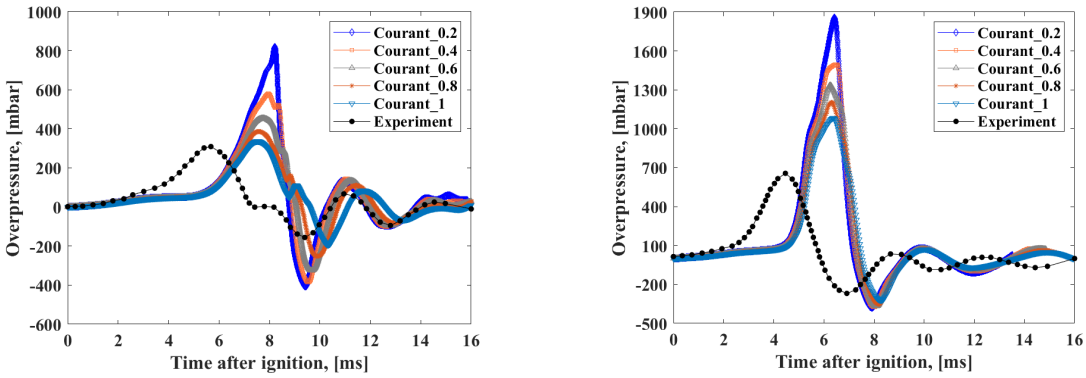

(a) Configuration 1 **(b)** Configuration 2

Figure 4.15: Overpressure versus time for Configurations 1 and 2, which is obtained in KFX-EXSIM, for the maximum Courant numbers of 0.2, 0.4, 0.6, 0.8, and 1.0.

The overpressure profiles inside the explosion tube for the grid sizes of 2.5 mm and the Courant numbers of 0.2, 0.4, 0.6, 0.8, and 1.0 in Configurations 1 and 2, as obtained from the XiFoam, are presented in Fig. 4.16.

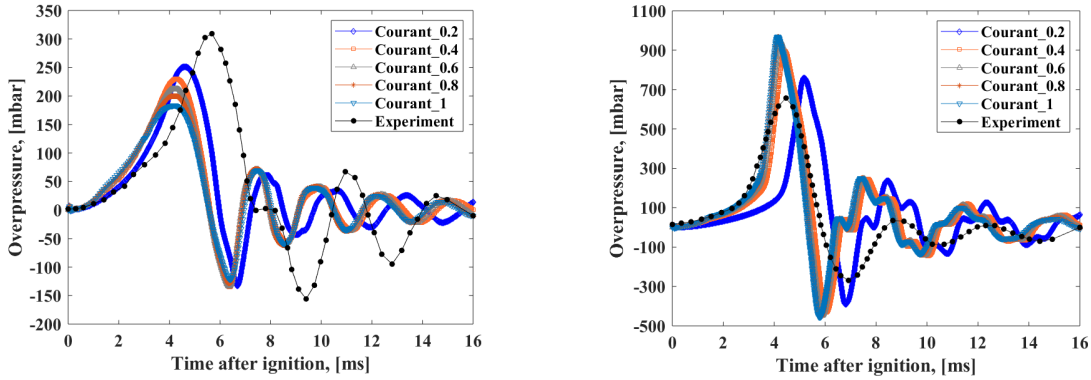

(a) Configuration 1 **(b)** Configuration 2

Figure 4.16: Overpressure in configuration 1 and configuration 2, which is obtained in `XiFoam`, for the Courant number of 0.2, 0.4, 0.6, 0.8, and 1.

For configuration 1, as shown in Fig. 4.16a, the peak overpressure tends to be decreased and occurred earlier with increases the maximum Courant number. While, for Configuration 2, the overpressure tends to be decreased and delayed with decreases the maximum Courant number, as presented in Fig. 4.16b. For both configurations, the numerical results which were obtained from the `XiFoam` simulations, were in relatively good agreement with the experimental data for the smaller Courant number (i.e. 0.2), unlike the simulation results from the `KFX-EXSIM`, where the higher maximum Courant number (i.e. 1.0) gave results which had relatively good agreements with the experimental results. The results of the grid dependency sensitivity analysis were summarized in Table 4.3 and Table 4.4 for Configurations 1 and 2, respectively.

Table 4.3: The peak overpressures (mbar), as obtained from `KFX-EXSIM` and `XiFoam` simulations, for the grid size 10, 5, and 2.5mm for Configuration 1.

	Grid size, [mm]			Relative discrepancy, [%]	
Code	10	5	2.5	10–5mm	5–2.5mm
`KFX-EXSIM`	360	210	1000	71	171
`XiFoam`	410	320	260	22	19

Table 4.4: The peak overpressures (mbar), as obtained from `KFX-EXSIM` and `XiFoam` simulations, for the grid size 10, 5, and 2.5mm for Configuration 2.

	Grid size, [mm]			Relative discrepancy, [%]	
Code	10	5	2.5	10–5mm	5–2.5mm
`KFX-EXSIM`	1100	1370	1400	25	2.2
`XiFoam`	1200	1170	790	2.5	31

As seen in Table 4.3, for Configuration 1, the numerical results from the `KFX-EXSIM` simulations were grid dependent. It can be noticed that also the numerical results from the

XiFoam simulations were grid dependent, but only with around 20% deviation. For Configuration 1, the results of the simulation obtained from grid size 5 and 2.5mm, as obtained from the KFX-EXSIM simulations, were consistent with each other as the relative discrepancy of the peak overpressure were smaller than 2.5%, as seen from Table 4.4. However, the results deviated from the experiment with more than 100%. The numerical results obtained from XiFoam simulations are again dependent on the grid size with the relative discrepancy of the peak overpressure increases from 2.5 to 30% when the grid size decreased by half.

In general, it can be observed that the grid size does not only affects the magnitude of the peak overpressure, it also affects the occurrence time of the peak overpressure. For both Configurations 1 and 2, the occurrence time of the peak overpressure shifts to the left of the plot for the KFX-EXSIM, as seen in Fig. 4.13, while shifts to the right for the XiFoam (see Fig. 4.14) as the grid size decreased by half.

4.4 Discussion

The profile of the overpressure time history, see Fig. 4.12, shows that the numerical results, which are obtained from KFX-EXSIM and XiFoam simulation, overestimates the peak overpressure for all configurations except for configuration 1 (in XiFoam simulation), which the peak overpressure was underestimated compared to the experimental results. However, the overestimation was much higher in KFX-EXSIM, with an average error of 51%, than in XiFoam (the average error was 26% for Configurations 2–4). The possible reason for the overestimation of the overpressure in the KFX-EXSIM simulations as compared to both the XiFoam and experimental results can be too high values of some of the constants used in the PDR formulation since they are calibrated for realistic scale geometries. The profile of the overpressure time history also shows that the overpressure curve obtained from the XiFoam simulation was much steeper as compared to the experimental results, especially for Configurations 3 and 4. This is might be due to modeling the top end of the tube as fully open, which is not a case in the experiment work (which was closed initial and open when the explosion pressure exceeds the minimum rupture pressure of the PVC membrane). It can be noticed that after some time from ignition occurred all curves reached to a maximum and immediately drop to a low value due to the release of the unburned gas to the atmosphere.

The results also show that the occurrence time of the peak overpressure was delayed for both configurations. However, the XiFoam simulations gave better results than the one obtained from the KFX-EXSIM as compared to the experimental results. The delay was between 1.54–1.94 ms in the KFX-EXSIM, while between 0.33–0.6 ms in the XiFoam. The reasons for the delay in the KFX-EXSIM can be a too slow flame acceleration in quasi-laminar combustion model, which was not investigated in this project since there was no access to the KFX-EXSIM source code.

From the sensitivity analysis results, it can be noticed that the numerical results from the KFX-EXSIM simulations for Configurations 1 and 2 were grid dependent. The main reason for the grid-dependent results is the PDR concept, that has constants which are changing every time when the grid changes, for example, area porosities and volume porosity. The numerical results obtained from the XiFoam simulations for both Configurations 1 and 2 were also grid dependent with the deviation between 2.5–30% as the grid size changed by half. However, it can be acceptable for industrial gas explosion simulations.

In general, the finer mesh with smaller Courant number (C = 0.2) gave results which were

in reasonably good agreement with the experimental data in the `XiFoam` simulation, while the coarser mesh with a higher maximum Courant number (C = 1.0) gave the results which were in relatively good agreement with the experiment. This is because of the PDR concept implemented in the `KFX-EXSIM` code. Where the effect of the sub-grid obstacle modeled as a source term in the conservation equations, hence, no need to use a finer mesh to capture the effect of the sub-grid obstacle.

Chapter 5

Simulation Case 2 - Effect of ignition position and vent size on overpressure and flame speed: premixed methane-air explosion

A stoichiometric premixed methane-air mixture gas explosion experiment at large scale FM Global's explosion test chamber was conducted by Bauwens et al. [13]. The objectives of the experiment were to examine the effect of the ignition location and vent size on the development of overpressure. Therefore, two ignition locations (back and center) and two different sizes of the square vent were used in the experiment. In this project, the experiment mentioned above was reproduced numerically using a CFD tool `KFX-EXSIM`. The details of the experimental and simulation setup, respectively, present in Section 5.1 and Section 5.2.

5.1 Experimental Details

The explosion test chamber had overall dimensions of $4.6 \times 4.6 \times 3.0$ m, which gives the inner volume of 63.7 m^3. A square vent with a cross-sectional area of 2.7 m^2, alternatively 5.4 m^2, located at the center of one of the vertical walls. The opening initially covered with a 0.02 mm thin sheet of polypropylene which destructed immediately after ignition occurs. The geometry of the chamber, including instrumentation is shown in Fig. 5.1. Four pressure transducers, which are used to measure the explosion overpressure-time histories inside the chamber, were mounted to the walls of the explosion chamber at different locations, named as P1–P4 in Fig. 5.1. Table 5.1 presents the coordinates of the pressure transducers used in the experiments. Two wave pressure transducers were installed outside the chamber at 1.17 and 3.45 m from the vent and 0.3 m above the ground. The flame front location is tracked using twenty thermocouples located at 1.4 m above the ground. They were placed inside the chamber at intervals of 0.5 m along two axes, while at intervals of 1 m along one axis outside the chamber as shown in Fig. 5.1. The thermocouples were used to measure the arrival time of the flame front at particular locations and to estimate the propagation flame speed both inside and outside the chamber.

The experiment was performed for 4 different tests as illustrated in Table 5.2. A stoichiometric methane-air mixture was used for all tests, however, there was slightly different in the actual concentration due to filling and sampling procedures. To create a uniform mixture within

the chamber, the methane-air mixture was mixed for some time using mixing fans. An Anarad infrared gas analyzer was used to sample the concentration of gas.

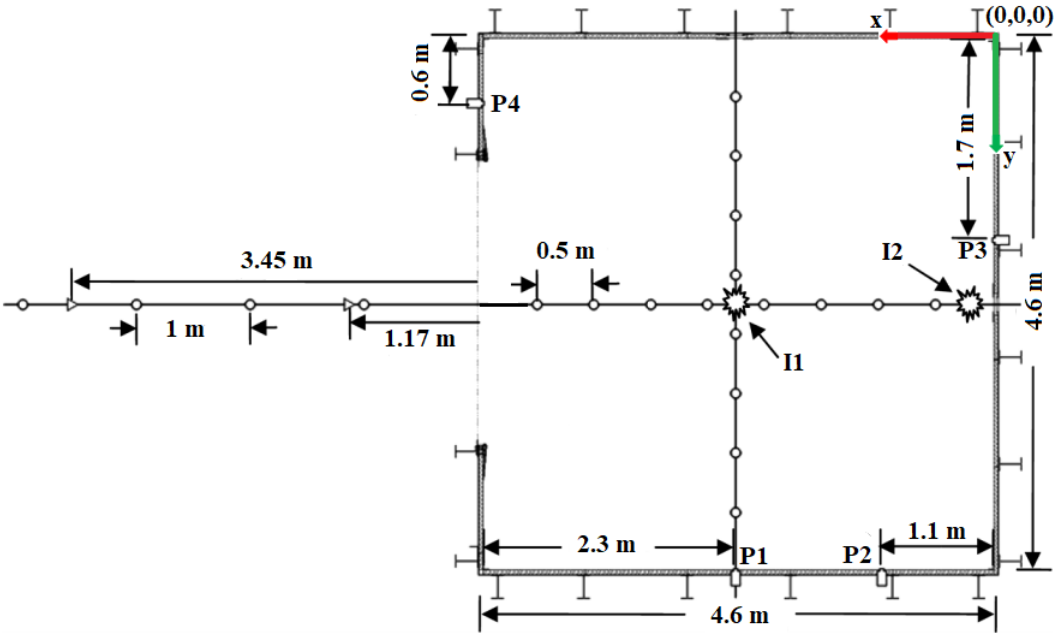

Figure 5.1: Top view of the test chamber including the location of the pressure transducers (rectangles), blast wave pressure transducers (triangles), flame arrival thermocouples (circles), and two ignition locations (I1 and I2), from [13].

Table 5.1: Coordinates of internal pressure transducers

Pressure Transducer	X Co-ord. [m]	Y Co-ord. [m]	Z Co-ord. [m]
P1	2.3	4.6	1.5
P2	1.1	4.6	1.5
P3	0.02	1.7	1.5
P4	4.6	0.6	1.5

Table 5.2: Experimental test programs

Test No.	Vent Size, [m^2]	Ignition Position
1	5.4	center (I1)
2	5.4	back (I2)
3	2.7	center (I1)
4	2.7	back (I2)

Ignition was performed using a carbon rod igniter at I1 and I2 locations. The center ignition, I1, and the back ignition, I2, were located at (2.3, 2.3, 1.5) and (0.25, 2.3, 1.5) m in the (x, y, z) coordinates, respectively. Information about the initial conditions, such as pressure and temperature, and air humidity was not given in the experiment [13].

5.2 Simulation Setup

For the experiment described in Section 5.1, numerical simulations were performed using the CFD tool `KFX-EXSIM`. The geometry of the explosion test chamber was created with the 3D-CAD tool, known as "`Doozer`", in `KFX-EXSIM` with sizes that matching with the experimental setup. To capture the venting of the unburnt gas and external explosion, the test chamber is enclosed by an external volume of $20 \times 16 \times 11\ \mathrm{m}^3$. The geometry of the test chamber together with the external volume is shown in Fig. 5.2.

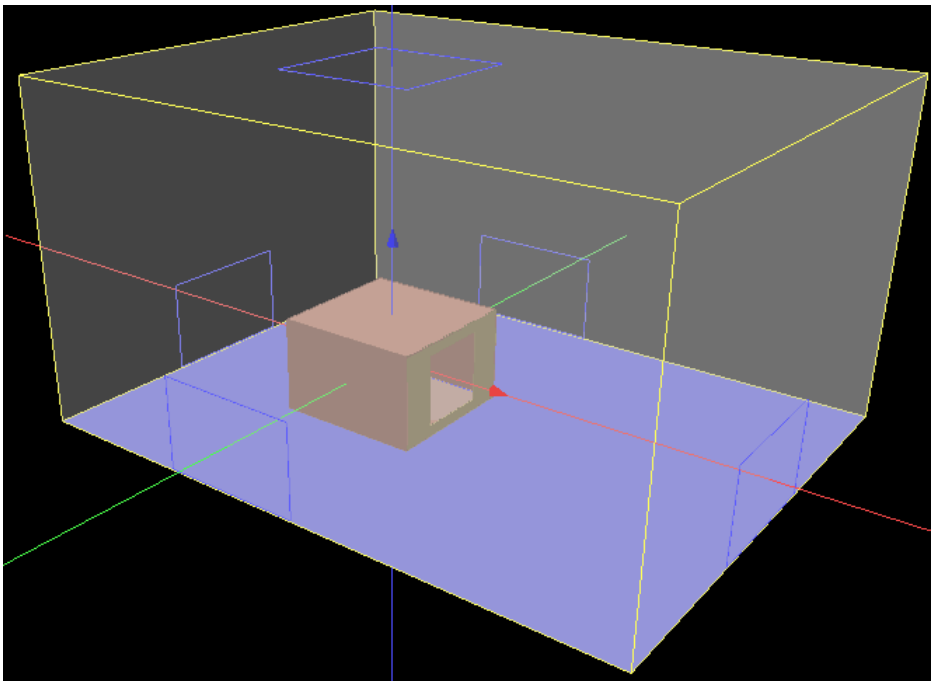

Figure 5.2: View of the explosion test chamber and the external volume.

First, the mesh is generated using the automatic grid generation option of `KFX-EXSIM`, then doubled the number of grids in each direction to get at least 10 cells in the smallest dimensions of the geometry (recommended in the `KFX-EXSIM` user manual [41]), giving 24 cells in x and y directions and 14 cells in the z direction. They are uniformly distributed inside the explosion test chamber giving a uniform Cartesian grid with a cell size of around 0.2 m. An expansion of 10% of the grid size towards the open boundaries from the test chamber in each direction was used. The computational mesh was approximately 8064 cells within the test chamber, while the total computational cells were 90272. The distribution of the computational mesh within the chamber and external volume is shown in Fig. 5.3.

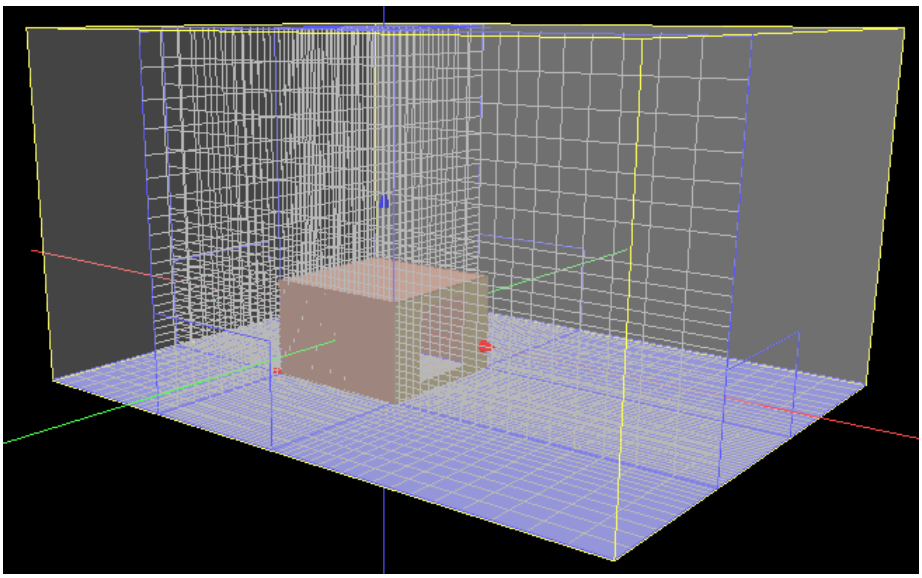

Figure 5.3: The mesh distribution within the chamber and external volume.

The initial gas composition was a stoichiometric methane-air mixture (9.5 % vol. methane) as outlined in the experiment. The back-wall ignition, I1, is located at 0.25, 2.3, and 1.5 m in x, y, and z directions, respectively, and modeled as "single wall" ignition. The center ignition, I2, is modeled as "point source" ignition and located at the center of the test chamber. The air was assumed to be composed of oxygen (21%) and nitrogen (79%) and was mixed perfectly with the fuel. Atmospheric pressure and 293 K were used as initial values of pressure and temperature, respectively. The initial values of 0 $\mathrm{m\,s^{-1}}$, 0.001 $\mathrm{m^2\,s^{-2}}$, 0.001 $\mathrm{m^2\,s^{-3}}$ were used for the velocity components, turbulence energy, and the dissipation rate of turbulence energy, respectively. The initial laminar burning velocity with the value of 0.38 $\mathrm{m\,s^{-1}}$ was used in the simulations.

The maximum Courant number, $C = U \cdot \delta t/\delta x$, based on the flow velocity and speed of sound were 1.5 and 15, respectively. It was created automatically. The time step, δt, was calculated based on the grid size, δx, Courant number, and local flow velocity at each iteration. For velocity components, the no-slip wall boundary condition with a logarithmic wall law, see Eq. (4.1), was used for both the walls of the test chamber and the bottom side of the external volume, i.e. ground. The fixed pressure boundary condition with the value of 1 bar was applied for the boundaries of the external volume (open boundaries). The value of 23.3×10^3 was used for the activation energy and universal gas constant ratio, i.e. E/R, and the value of the constant A_{ch} was 1.8×10^{-14}.

5.3 Results

The numerical simulation results, as obtained from `KFX-EXSIM`, for the experimental scenario outlined in Section 5.1 are presented in this section. The numerical results regarding the flame propagation speed and overpressure time-history were compared with the experimental data and LES simulation results obtained from [13]. The LES simulations were performed using a structural grid with a cell size of 7.5 cm which gives a computational mesh of approximately 10^6 cells. The combustion was modeled using a modified version of the Weller flame wrinkling combustion model, and a one-equation eddy viscosity model was used for the sub-grid

turbulence model.

As shown in Figures 5.4–5.7, it can be noticed that two large overpressure peaks appeared in the overpressure time-history of the experimental data for all tests. The first large peak associated with the Helmholtz oscillations and the external explosion. The Helmholtz oscillation is significantly enhanced by the introduction of Taylor instability when the less dense burned gas is accelerated toward the denser unburned fuel-air mixture. The external explosion occurs immediately after the Helmholtz oscillation when the hot vented products ignite the unburned methane-air mixture, which was previously vented. It raises the pressure outside the chamber and reduces the difference in pressure across the vent, which in turn reduces the venting process. If these two phenomena, i.e the Helmholtz oscillation and external explosion, are in phase, resulting relatively strong overpressure peak. However, the interaction between them most likely depends on some factors such as flame propagation speed, the location of ignition, and the chamber geometry. The second large overpressure peak associated with acoustics oscillation. The experimental data shows that for Tests 1, 2, and 4, the Helmholtz oscillations and external explosion were in phase, thus defining the maximum overpressure. While the Helmholtz oscillations and external explosion were out of phase in Test 3, the maximum overpressure is obtained from the acoustic oscillations. All the overpressure time-history presented below are filtered using an 80 Hz low pass filter. In the experiment, the flame propagation speeds were computed using the arrival time of the flame front from the line of thermocouples. The negative and positive values show the flame propagation towards the back wall and the vent, respectively. The value of 0 in the x coordinate indicates the position of the ignition source. Since the readings of all the pressure transducer gave almost the same overpressure time-history data for both the simulation and experiment, only the readings of the pressure transducer P1 are presented here.

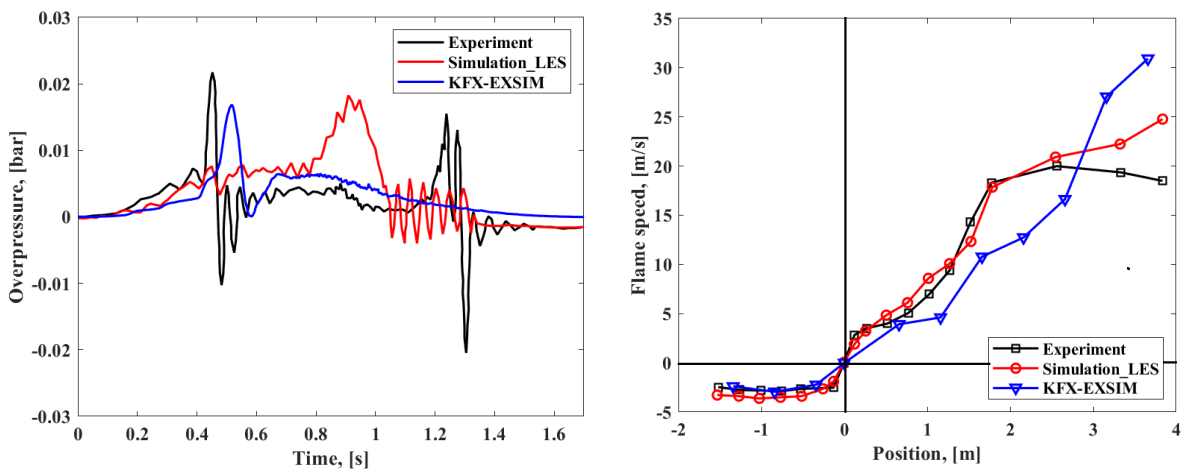

(a) Overpressure

(b) Flame speed

Figure 5.4: Overpressure time-history at position P1 and flame speed as a function of position for Test 1. The negative flame speed and position are shows the propagation of the flame from the ignition position (center ignition) towards the back wall of the chamber.

Fig. 5.4 shows the overpressure time-history and the flame speed as a function of position, as obtained from `KFX-EXSIM` simulation, in comparison with the experimental data and LES simulation for Test 1. As shown in Fig. 5.4a, with regard to the overpressure time-history, the prediction from the `KFX-EXSIM` simulation was in reasonably good agreement with the ex-

perimental data. Unlike the prediction from the LES simulation, which underestimates the first large peak with a large extent, the prediction obtained from KFX−EXSIM only underestimates the first peak overpressure by about 19%, however, the occurrence time of the first overpressure peak was delayed by 0.035 s. The figure also shows the KFX−EXSIM simulation completely damped the second large overpressure peak associated with acoustics oscillation, while the LES simulation overestimated it. Regarding the flame propagation speed as a function of position, as shown in Fig. 5.4b, the results of the KFX−EXSIM simulation shows relatively good agreement both with the experimental data and the results of the LES simulation.

The results of the KFX−EXSIM simulation compared to the experimental data and the LES simulation results for Test 2 are shown in Fig. 5.5. The prediction obtained from KFX−EXSIM simulation shows good agreement with the experimental data. As shown in Fig. 5.5a, in KFX−EXSIM, the first large overpressure peak was underestimated by approximately 10% and was obtained at $t = 0.623$s which was delayed by 0.123 s compared to the experimental data. While the first large overpressure peak was completely damped by the LES simulation. The figure also shows that the results of both the KFX−EXSIM and LES simulation were in reasonably good agreement with the experiment with regard to the second large overpressure peak. The predicted flame propagation speed obtained from both KFX−EXSIM and LES simulation are consistent with the experimental data as shown in Fig. 5.5b.

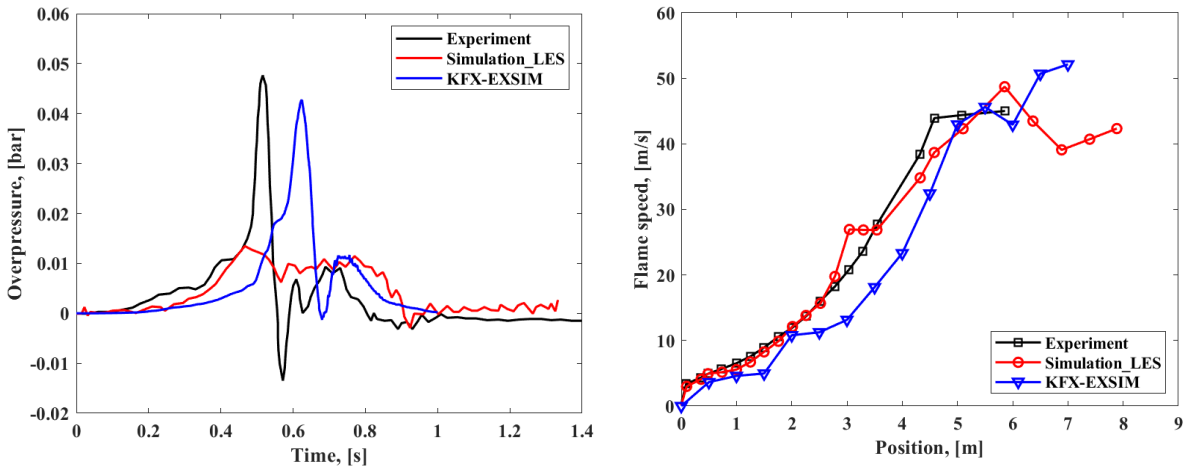

(a) Overpressure

(b) Flame speed

Figure 5.5: Overpressure time-history at position P1 and flame speed as a function of position for Test 2.

Fig. 5.6 illustrates the results of the KFX−EXSIM simulation together with the experimental data and the LES simulation results for Test 3. With regard to the first large overpressure peak, the KFX−EXSIM simulation was in good agreement with the experimental data with only a small time shift, as shown in Fig. 5.6a. However, the second large overpressure peak at $t = 1.2$s was totally damped by the KFX−EXSIM simulation. Unlike the KFX−EXSIM, the LES simulation shows good agreement with the experimental data with regard to acoustic-related second large overpressure peak, however, the predicted second large overpressure peak was overestimated and appears earlier than in the experiment. The flame propagation speed, as shown in Fig. 5.6b, obtained in both KFX−EXSIM and LES simulation, shows a relatively good agreement with the experimental data.

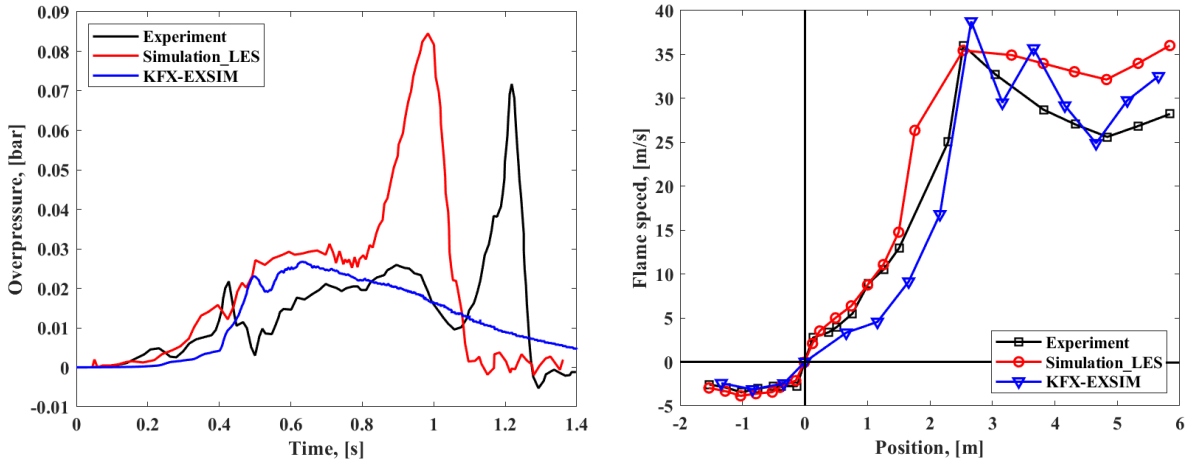

(a) Overpressure **(b)** Flame speed

Figure 5.6: Overpressure time-history at position P1 and flame speed as a function of position for Test 3. The negative flame speed and position are shows the propagation of the flame from the ignition position (center ignition) towards the back wall of the chamber.

The results of the `KFX-EXSIM` simulation in comparison with the experimental data and the results of the LES simulation for Test 4 are presented in Fig. 5.7. Similar to Test 1 and 2, the second large overpressure peak associated with acoustic oscillation was completely damped by the `KFX-EXSIM` simulation, as shown in Fig. 5.7a. The figure also demonstrates that, with regard to the first large overpressure peak associated with the Helmholtz oscillation and external explosion, the `KFX-EXSIM` simulation was in relatively good agreement with the experimental data compared to the LES simulation result. However, the first large overpressure peak was underestimated by approximately 12.5% and the occurrence time was delayed by 0.152 s. Similar to other tests, i.e Test 1–3, regarding the flame propagation speed, the `KFX-EXSIM`, and LES simulation results were in reasonably good agreement with the experimental data, as illustrated in Fig. 5.7b.

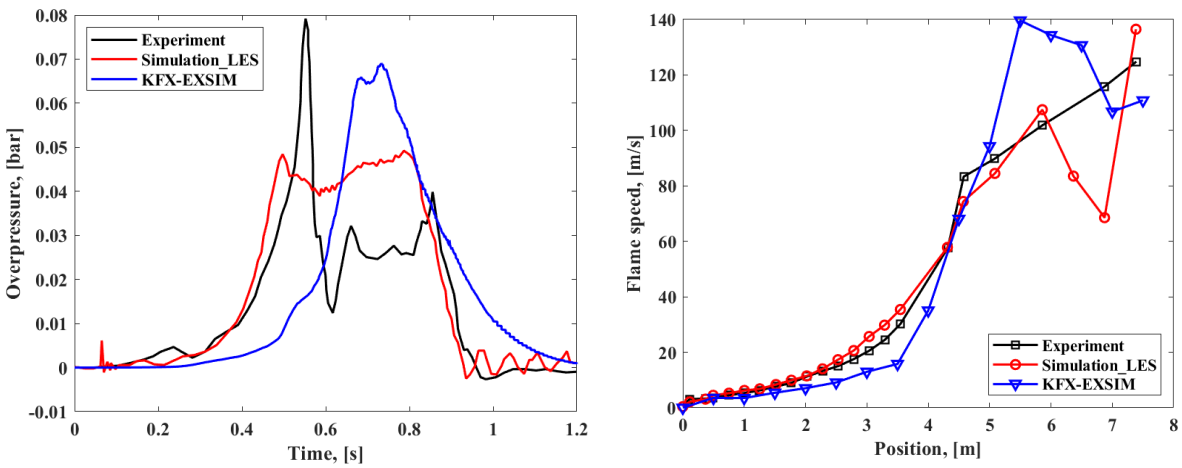

(a) Overpressure **(b)** Flame speed

Figure 5.7: Overpressure time-history at position P1 and flame speed as a function of position for Test 4.

5.4 Discussion

As seen from Figures 5.4b, 5.5b, 5.6b and 5.7b, both the KFX-EXSIM and LES simulations gave reasonably good predictions with regard to the flame propagation speed. However, the flame initially propagates a little slower in the KFX−EXSIM than in the experiment and the LES simulation. The possible reason can be a too small specified laminar burning velocity, which in quasi-laminar combustion model provides a slow acceleration of the flame.

Regarding the time-history of overpressure, see Figures 5.4a, 5.5a, 5.6a and 5.7a, both KFX-EXSIM and LES simulations captured the initial pressure build-up very well. However, the LES simulations completely damped the first large overpressure peak associated with both the Helmholtz oscillation and external pressure. The reasons for this may be the Taylor instability, caused by the effect of both Helmholtz oscillation and external explosion, cannot be captured sufficiently on the 7.5 cm mesh or the model is not well enough to capture the development of the external explosion and the resulting expansion. Unlike the LES simulations, the numerical results obtained from KFX−EXSIM show a good agreement with the experimental data regarding the first large overpressure peak. This implies that the KFX−EXSIM code sufficiently captured the Taylor instability and the development of the external explosion. The simulations, however, underestimated the first large overpressure peak with an average error about 15% and delayed the occurrence time within 0.035–0.152 s. The reason for the delay can be a too slow flame acceleration in quasi-laminar combustion model. The reason for underestimation of the first large overpressure in the KFX−EXSIM simulation may be the use of the first order accurate upwind scheme in the KFX−EXSIM code to discretized the convective term, which can give a numerical diffusion.

As seen from the time-history overpressure plots, the second large overpressure peaks associated with the acoustic oscillation were not well captured or completely damped by the KFX−EXSIM simulations. This was because the model did not satisfactorily capture the increase in sub-grid turbulence due to acoustics or there is acoustic damping in the model. Contrary, the second large overpressure peaks were captured by the LES simulation within 30% deviation. But, they appeared earlier compared to the experiment. This may be due to the lack of acoustic damping in the model.

Chapter 6

Simulation Case 3 - A premixed natural gas-air explosion in a test rig representing an offshore process module at a realistic scale

Premixed natural gas-air explosion experiments in a test rig representing at full scale an offshore module were conducted in the HSE-funded project [14]. 45 different experiments were performed, where each experiment was different in wall confinement configuration, ignition location, and equipment layout. In this project, Experiment 16 and 17, as named in the experiment report [14], were numerically reproduced using `KFX-EXSIM`. Both Experiments 16 and 17 had the same wall confinement configuration, equipment layout, and natural gas composition, however, they were different in the ignition location. The experimental details and the simulation setup, respectively, are presented in Section 6.1 and Section 6.2. Section 6.3 gives a brief overview of the findings of the simulation compared to the experimental data. The brief discussion of the simulation results outlined in Section 6.3 is presented in Section 6.4.

6.1 Experimental Details

The test rig used to perform the natural gas-air mixture explosion had overall dimensions of $28 \times 12 \times 8$ m and constructed using steel. To simulate typical process plant and pipework which would be found on an offshore installation, steel obstacles with different size and shapes were installed within the test rig. The experiments were performed for three different wall confinement configurations, however, Experiments 16 and 17 were performed using the same wall confinement configuration. In this configuration, the rig does not have the walls and one-third of the roof removed. The schematic view of the test rig with the wall confinement mentioned above is shown in Fig. 6.1. Thirty-five pressure transducers, which were used to measure the overpressure within the test rig, were installed inside the rig at different locations. Thirteen pressure transducers were used to measure the incident overpressure wave outside the test rig. They were located on radial lines from the test rig in different locations. The coordinates of both internal and external pressure transducers were not presented here since the experimental data are confidential. However, Fig. A.2 and Fig. A.3 shows the locations of some of the internal and external pressure transducers. The pressure transducers used were PCB 102A06 piezo-electric transducers for the internal overpressure measurement and either PCB 102A06

or 102A05 piezo-electric for the external pressure measurement, each with built-in F.E.T. amplifiers. The ignition was activated by a single low energy spark at a specified location. The ignition positions located at (13.5, 5.0, 4.3) and (9.0, 11.6, 0.4), respectively, were used for Experiment 16 and 17. Experiments 16 and 17 were conducted under the air temperature of 287 and 286 K, respectively. The relative air humidity (%) was 65 and 100, respectively, for Experiment 16 and 17.

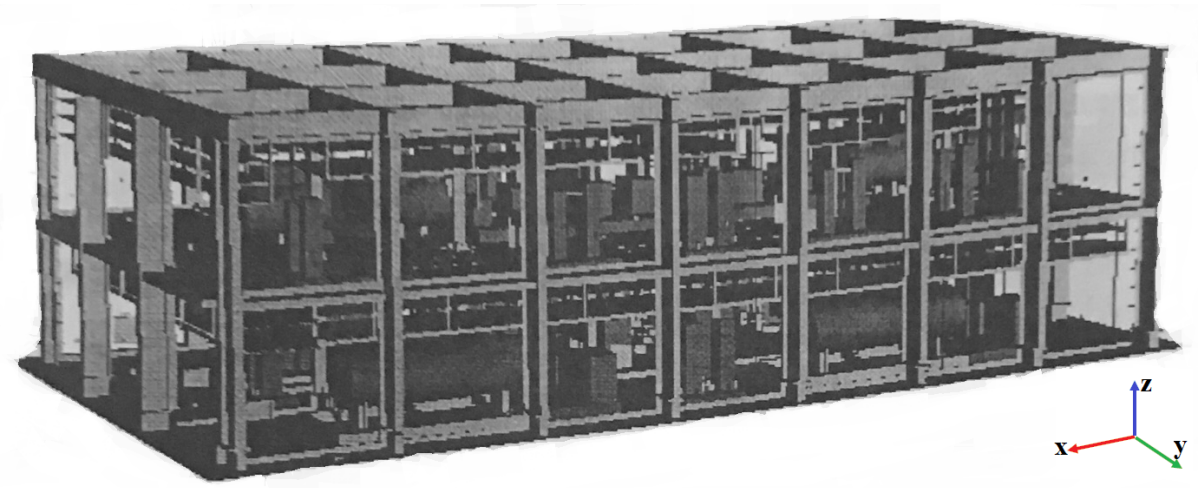

Figure 6.1: The schematic view of the test rig, taken from [14].

The natural gas was composed of methane (90.74% volume/volume), ethane (7.97%), propane (0.97%), butane (0.23%), and small amounts of higher hydrocarbons and nitrogen. The actual gas concentration measured at eight different locations inside the rig before ignition using an on-line gas analysis system. The average equivalence ratios (calculated based on the average concentration) of 1.10 and 1.11 were used in Experiment 16 and 17, respectively. To hold the natural gas-air mixture inside the test rig, all open faces of the rig were covered with 0.125 mm thick polythene sheet. For Experiment 17, where the ignition position was relatively close to the polythene sheet, low energy detonating cord was connected to the sheet and detonated immediately before ignition to cutting the polythene sheet.

6.2 Simulation Setup

Experiments 16 and 17 outlined in Section 6.1 were numerically reproduced using `KFX-EXSIM`. The geometry of the test rig for Experiments 16 and 17 was generated directly from CAD geometry data into the `KFX-EXSIM` geometry format. The test rig was enclosed by an external volume of $168 \times 152 \times 60\ \mathrm{m}^3$ to capture the venting of the unburnt gas and external explosion. Fig. 6.2 shows the geometry of the test rig that made with "Doozer". As recommended by the `KFX-EXSIM` manual [41] for the realistic scale geometry, the mesh was generated using the automatic grid generation options of `KFX-EXSIM` which gave 47, 20, 14 cells in x, y, and z directions, respectively. They were distributed uniformly in the inner volume of the test rig. This gave a uniform Cartesian grid with a cell size of around 0.6 m. This grid size gave a computational mesh of approximately 13160 cells for the inner volume of the rig. The grid was expanding by 10% towards the open boundaries, which are the boundaries of the external volume, from the test rig in each direction. Hence, the total number of computational cells was

284700. The distribution of the mesh within the test rig and the external volume is shown in Fig. 6.3.

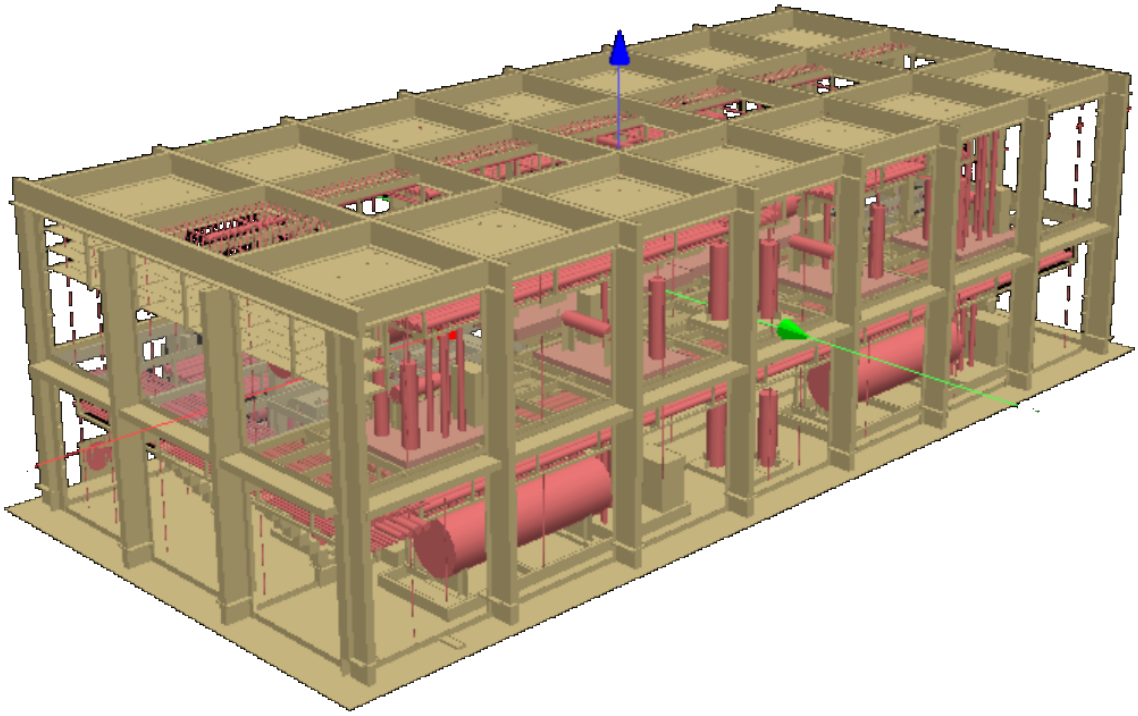

Figure 6.2: View of the geometry of the test rig.

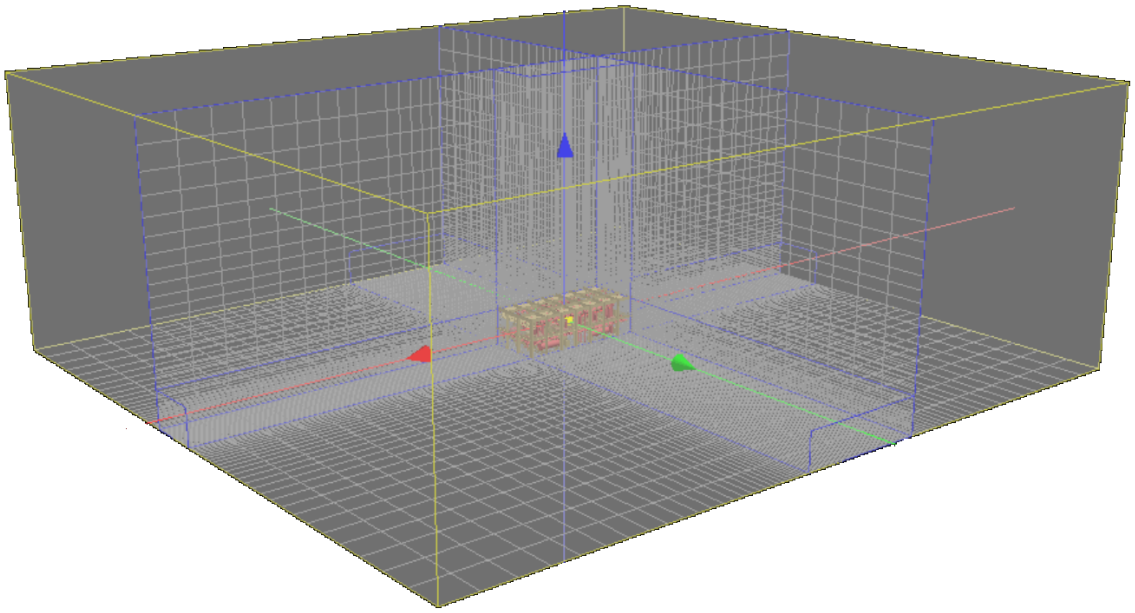

Figure 6.3: View of the mesh distributions with the rig and the external volume.

As described in Section 6.1, the natural gas used in the experiments was composed of methane, ethane, propane, butane, and small amounts of higher hydrocarbons and nitrogen, however, pure methane is used in the simulation. This is due to the options in the `KFX-EXSIM`

to use natural gas as either pure methane or the mixture of methane and propane. Both of the options were used in the simulations and gave an almost similar result, this is due to a small amount of the propane presented in the natural gas. The equivalence ratios of 1.10 and 1.11 were used for Experiments 16 and 17, respectively. The air assumed to be composed of 21% oxygen and 79% nitrogen and was perfectly mixed with the fuel. Both the ignitions were modeled as ”free space” type with the location matching with the experimental setup. The initial values of $1\ \mathrm{bar}$ and 293 K, respectively, for pressure and temperature, were used in the simulations. The initial value of the velocity components was 0. For turbulence energy and dissipation rate of turbulence energy, respectively, 0.001 $\mathrm{m^2\,s^{-2}}$ and 0.001 $\mathrm{m^2\,s^{-3}}$ were used as initial values. The initial laminar burning velocity was 0.38 $\mathrm{m\,s^{-1}}$.

The maximum Courant numbers were generated using the automatic grid generation option of `KFX-EXSIM` gave 0.5 and 5 based on the flow velocity and speed of sound, respectively. The velocity boundary condition applied to the walls and floor of the rig and the bottom side of the external volume, i.e ground, was a no-slip wall boundary condition with a logarithmic law, see Eq. (4.1). The fixed boundary condition with the value of $1\ \mathrm{bar}$ was used for the open boundaries. The values of the constant A_{ch} and the ratio of activation energy E to universal gas constant R were 23.3×10^{3} and 1.8×10^{-14}, respectively.

6.3 Results

The numerical results from the realistic scale experiments, which described in Section 6.1, simulation produced information about pressure time-history, the magnitude and occurrence time of the peak overpressure. Here, the results of the simulation with regard to the magnitude and occurrence time of the peak overpressure compared with the experimental data are presented. Due to the confidentiality of the experimental results, to give a global picture of the accuracy and the characteristics of the model, all predictions are compared to experimental data using a scatter plot as shown in Figures 6.4–6.7. The diagonal (Pred. = Obs.) shows a completely ideal simulation model. The upper diagonal (Pred. = 2*Obs.) and the bottom diagonal (Pred. = 0.5*Obs.) are called the lines for a band factor of 2.

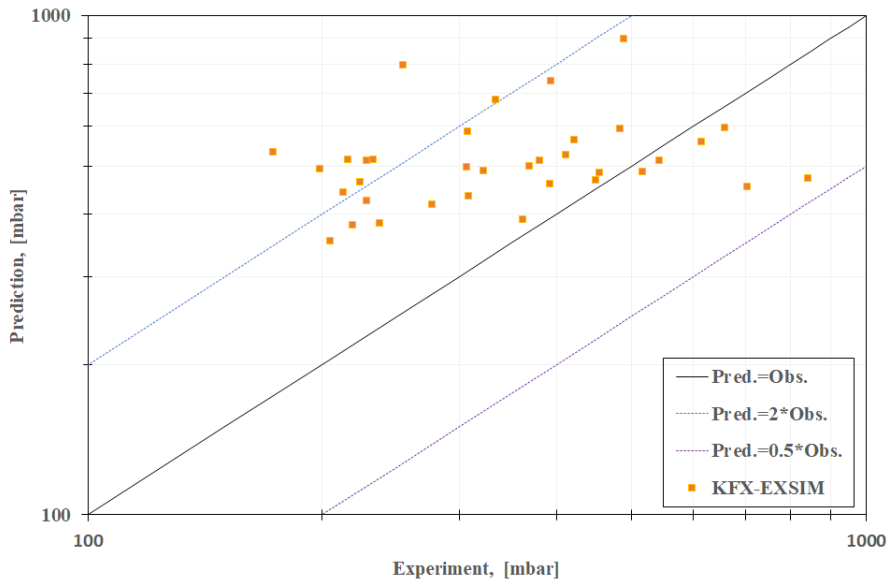

Figure 6.4: Predicted and experimental peak overpressure inside the test rig for the Experiment 16 case.

Fig. 6.4 shows the peak predicted overpressure in each internal pressure transducer as a function of the corresponding experimental overpressure, for Experiment 16 case. Most of the predictions are observed to fall within the band factor of 2 as shown in Fig. 6.4. It can be noticed that the prediction for lower overpressure fall outside the band of factor 2, which were overestimated by more than 100%. These values were readings from the internal pressure transducers which were installed very near to walls and obstacles.

Fig. 6.5 shows the peak predicted overpressure in each external pressure transducer as a function of the corresponding experimental overpressure, for Experiment 16 case. All the predictions fall within the band factor of 2.

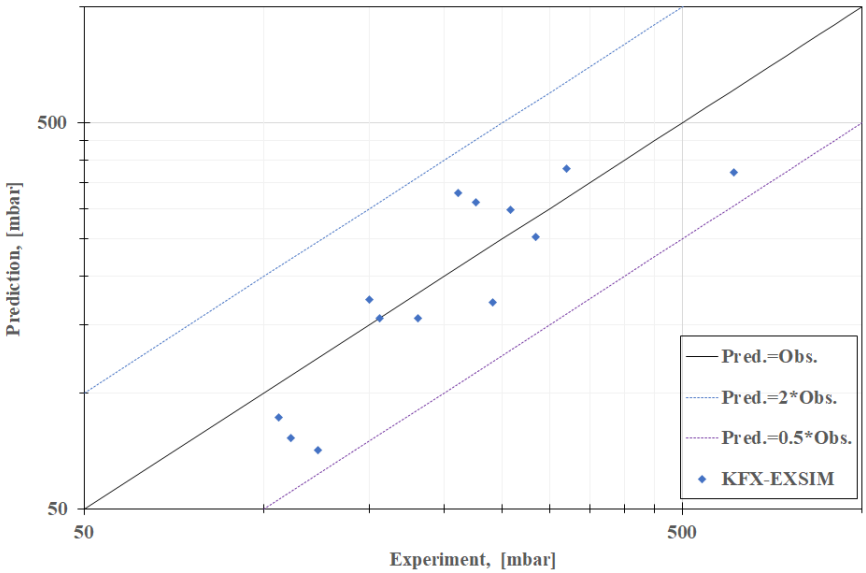

Figure 6.5: Predicted and experimental peak overpressure outside the test rig for the Experiment 16 case.

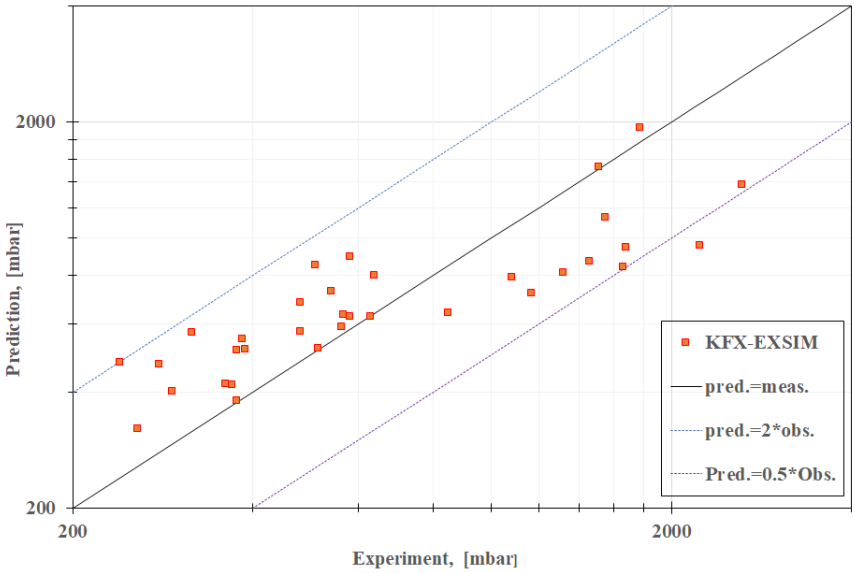

Figure 6.6: Predicted and experimental peak overpressure inside the test rig for the Experiment 17 case.

The peak predicted overpressure in each internal pressure transducers as a function of the corresponding experimental overpressure, for Experiment 17 case, is shown in Fig. 6.6. It can be observed that almost all the predictions fall within the band factor of 2.

The peak predicted overpressure in each external pressure transducer as a function of the corresponding experimental overpressure, for Experiment 17 case, is illustrated in Fig. 6.7. It can be noticed that the simulation overestimate the lower overpressure, which is reading from the external pressure transducer located near to the open boundary in the y-direction, more than 100%. And also can be observed that some of the higher peak overpressures are fall outside the band factor of 2.

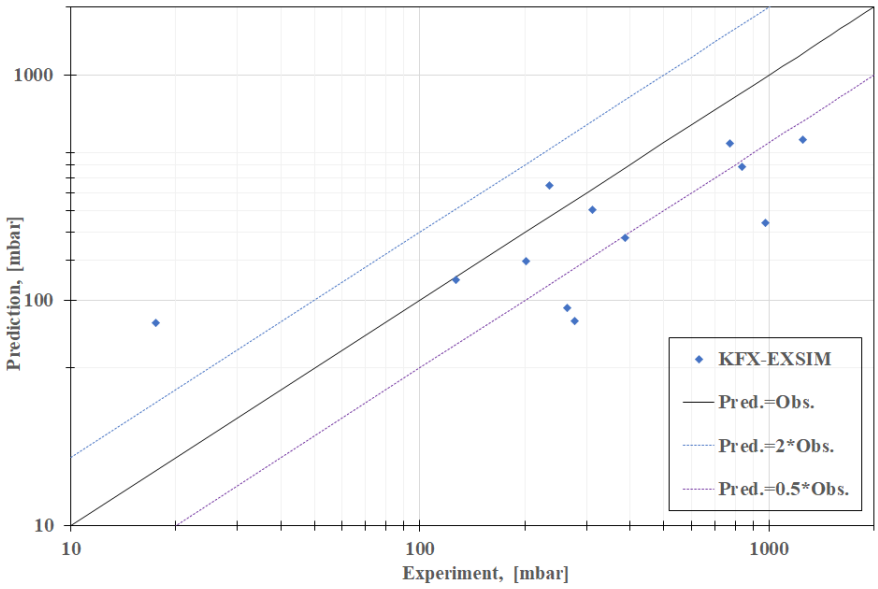

Figure 6.7: Predicted and experimental peak overpressure outside the test rig for the Experiment 17 case.

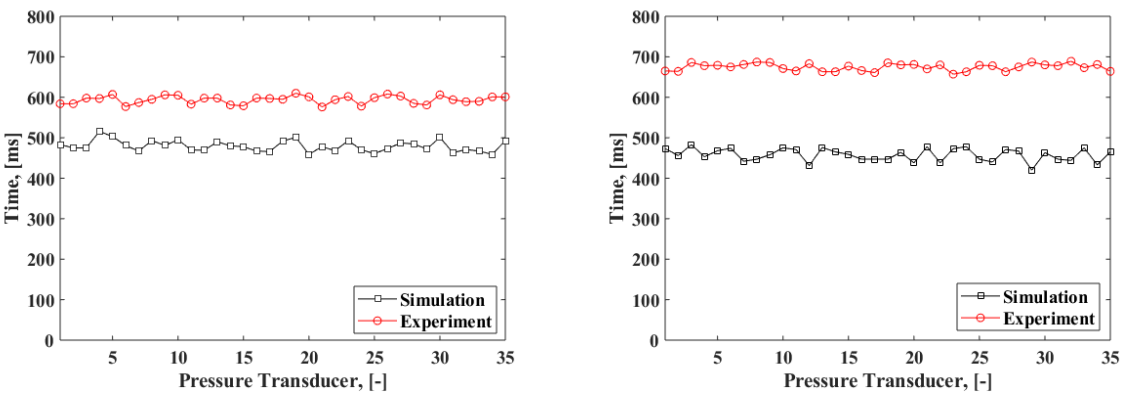

(a) Experiment 16 **(b)** Experiment 17

Figure 6.8: The occurrence time of the peak overpressure in each internal pressure transducers, as obtained from the `KFX-EXSIM` simulation and experiments.

Fig. 6.8 illustrates the occurrence time of the peak overpressure at each internal pressure transducers for both Experiments 16 and 17. As seen in Fig. 6.8, for both Experiments 16 and

17, the predicted peak overpressures appeared earlier than the experiments for each internal pressure transducers. The occurrence time was deviated by an average value of 0.2 s and 0.12 s in Experiment 16 and 17, respectively, compared to the experimental data.

6.4 Discussion

Several simulations were performed for the realistic scale experiments, Experiments 16 and 17, using the KFX-EXSIM CFD code to give a global picture of the accuracy and the characteristics of the model. The main difference between the two experiments is the location of the ignition. The ignition located around the center of the rig for Experiment 16, while it located at (9.0, 11.6, 0.4) (near one of the walls of the rig) for Experiment 17.

For Experiment 16, as seen from the plots of the internal overpressures, some of the predictions, where reading from the internal pressure transducers that were installed very close to the roof of the rig, obstacles, and ignition point, fall outside the band factor of 2. The reason for this can be the pressure reflections from obstacles and the roof of the rig may not be captured properly due to the coarse grid. Another reason can be the geometrical treatment by the PDR concept, which cannot represent all the details of the geometry as only cylindrical and rectangular shapes are used in KFX-EXSIM. As seen from the external overpressure plots, all predictions fall within the band factor of 2. This indicates that the model satisfactorily captured the development of the external explosion.

For Experiment 17, as seen from the internal overpressure plots, all the predictions, even readings from the internal pressure transducers located near to the roof of the rig and obstacles, fall within the band factor of 2. This can be due to the fact that the fully developed turbulent flames were reached to the internal pressure transducers located close to the roof and obstacles since they are located a little far from the ignition point. Some of the predictions fall outside the band factor of 2, as seen from the external overpressure plots. It can be observed that the overpressure reading from the external overpressure located close to the open boundary in the y-direction overestimated by the simulation within about 200%. The main reason for the overestimation can be the non-physical pressure reflection from the open boundary as the reading point was located close to both the ignition point, as compared to the center ignition in Experiment 16, and the open boundary. The figure also shows that some of the external overpressures were underestimated with deviations of around 50-60%. The reason for this can be the use of the courser mesh at the readings point, which cannot sufficiently resolve the external expansion since they are located a little far from the rig and 10% of grid expansion was used.

As seen from the peak overpressure occurrence time plots, for both Experiments 16 and 17, the predicted internal peak overpressures were appeared earlier compared to the experiment. The possible reason for the discrepancy may be the dynamic model constant in the laminar combustion model, see Section 3.5.1, gave a high laminar burning velocity. However, this required further investigation and was not performed in this work since the KFX-EXSIM source code was inaccessible.

Chapter 7

Conclusion

In this project, several simulations were performed in order to investigate the ability of the CFD code KFX-EXSIM to simulate gas explosions. Three experiments of the gas explosion of stoichiometric hydrogen-, methane-, and natural gas-air mixtures in small to realistic scale geometries were chosen. The XiFoam solver of the OpenFOAM toolbox was also used to simulate the small scale gas explosion experimental scenario. Based on the numerical results for all experimental scenarios the following are concluded:

- Both KFX-EXSIM and XiFoam codes can be used to simulate a gas explosion in a small-scale rectangular tube with and without the presence of obstacles. However, XiFoam gave better results compared to KFX-EXSIM. To increase the accuracy or capability of the KFX-EXSIM code to simulate small scale gas explosions, the values of some constants in the Porosity/Distributed Resistance (PDR) concept should be changed/modified since their values were found from calibration against realistic scale gas explosions. However, a parametrized study is needed to identify and quantify which constant affect the result the most.

- The KFX-EXSIM explosion model was grid dependent, this is because the values of some of the variables in the PDR formulation, e.g. area porosities and volume porosity, are changing with changing in grid size. The XiFoam was also found to be grid dependent, however, the relative discrepancy of the peak overpressure was 25–30% with decreases the grid size by half. This can be acceptable for industrial gas explosion simulations.

- The KFX-EXSIM code was found to be able to capture the overpressure associated with Helmholtz oscillations and external explosion without the need of the finer grid. However, it was not suitable for resolving acoustically derived overpressures.

- The KFX-EXSIM explosion model reproduces the realistic scale premixed natural-gas explosion experiments within a band factor of 2.

- Potential for improvement in KFX-EXSIM is the quasi-laminar combustion model. In all simulations for small scale and large scale vented gas explosion experimental cases, the occurrence time of the predicted peak overpressures was delayed compared to the experimental results. In all simulations for realistic scale gas explosion scenario, there was also a discrepancy between the simulations results and experimental data regarding the occurrence time of the peak overpressure.

Bibliography

[1] B. H. Hjertager. Influence of turbulence on gas explosions. *Journal of Hazardous Materials*, 9(3):315–346, 1984.

[2] I. O. Moen, M. Donato, R. Knystautas, and J. H. Lee. Flame acceleration due to turbulence produced by obstacles. *Combustion and Flame*, 39(1):21–32, 1980.

[3] B. H. Hjertager, K. Fuhre, and M. Bjørkhaug. Gas explosion experiments in 1:33 and 1:5 scale offshore separator and compressor modules using stoichiometric homogeneous fuel/air clouds. *Journal of loss prevention in the process industries*, 1:197–205, 1988.

[4] C. Chan, I. O. Moen, and J. H. S. Lee. Influence of confinement on flame acceleration due to repeated obstacles. *Combustion and Flame*, 49:27–39, 1983.

[5] B. H. Hjertager, K. Fuhre, S. J. Parker, and J. R. Bakke. Flame acceleration of propane-air in a large-scale obstructed tube. In *Progress in Astronautics and Aeronautics*, NewYork: AIAA Inc, 94: 504–522, 1984.

[6] I. O. Moen and J. H. S. Lee. Pressure development due to turbulent flame propagation in large-scale methane-air explosions. *Combustion and Flame*, 47:31–52, 1982.

[7] B. F. Magnussen, T. Evanger, B. E. Vembe, N. I. Lilleheie, B. Grimsmo, B. Velde, J. Holen, G. Linke, P. Genillon, H. Tonda, and P. Blotto. Kameleon fireex in saftey applications. In *SPE International conference on Health, Safety, and the Environment in Oil and Gas explosion and Production, SPE1451*, Stavanger, Norway, June 26–28 2000.

[8] B. F. Magnussen, B. Grimsmo K. E. Rian, N. I. Lilleheie, R. N. Kleiveland, and B. E. Vembe. Computational analysis of large-scale fires in complex geometries - a means to safeguard people and structural integrity in the oil and gas industry. *Chemical Engineering Transactions*, 31:793–798, 2013.

[9] B. H. Hjertager. Explosion in offshore modules. *Institution of Chemical Engineers Symposium Series*, 124:19–35, 1991.

[10] B. H. Hjertager. Computer modelling of turbulent gas explosions in complex 2d and 3d geometries. *Journal of Hazardous Materials*, 34(2):173–197, 1993.

[11] O. Sæter. *Modelling and simulation of gas explosions in complex geometries, Dr.ing. thesis*. Telemark college, Porsgrunn, Norway, 1998.

[12] X. Lv, L. Zheng, Y. Zhang, M. Yu, and Y. Su. Combined effects of obstacle position and equivalence ratio on overpressure of premixed hydrogen-air explosion. *International Journal of Hydrogen Energy*, 41(39):17740–17749, 2016.

[13] C. R. Bauwens, J. L. Chaffe, and S. Dorofeev. Experimental and numerical study of methane-air deflagrations in a vented enclosure. *Fire Safety Science*, 9:1043–1054, 2008.

[14] J. A: Evans, D. M. Johnson, and B. J. Lowesmith. Report on experimental programme on explosions in full-scale offshore module geometries - phase 3a. , UK Health and Safety Executive, England, 1999.

[15] J. D. Anderson. *Computational Fluid Dynamics: The Basics with Applications*. Mechanical Engineering Series. McGraw-Hill, Inc., New York, 1995.

[16] T. Poinsot and D. Veynante. *Theoretical and Numerical Combustion*. R.T. Edwards, Inc., USA, second edition, 2005.

[17] J. Blazek. *Computational Fluid Dynamics: Principles and Applications*. Elsevier, Amesterdam, 2001.

[18] I. S. Ertesvåg. *Turbulent Flow and Combustion: From turbulence theory to engineering tools*. Tapir Academic Publisher, Trondheim, 2000.

[19] J. Warnatz, U. Maas, and R. W. Dibble. *Combustion - Physical and Chemical Fundamentals, Modeling and Simulation, Experiments, Pollutant Formation*. Springer, Berlin, first edition, 1996.

[20] S. R. Turns. *An Introduction to Combustion: Concepts and Applications*. McGraw-Hill Companies, Inc., third edition, 2012.

[21] C. K. Law. *Combustion Physics*. Cambridge University Press, Cambridge, 2006.

[22] J. C. Tannehill, D. A. Anderson, and R. H. Pletcher. *Computational Fluid Mechanics And Heat Transfer, Series in Computational and Physical Processes in Mechanics and Thermal Sciences*. CRC press, third edition, 2013.

[23] B. E. Launder and D. B. Spalding. The numerical computation of turbulent flows. *Computer Methods In Applied Mechanics and Engineering*, 3:269–289, 1974.

[24] W. T. Sha and B. E. Launder. A model for turbulent momentum and heat transport in large rod bundles. [lmfbr]. Technical report, Argonne National Lab., IL (USA), 1979.

[25] N. Swamination and K. N. C. Bray. *Turbulent Premixed Flames*. Cambridge University Press, 2011.

[26] B. J. Arntzen. *Modelling of turbulence and combustion for simulation of gas explosions in complex geometries, Dr.Ing. thesis*. NTNU, Trondheim, Norway, 1998.

[27] R. Amirante, E. Distaso, P. Tamburrano, and R. D. Reitz. Laminar flame speed correlations for methane, ethane, propane and their mixtures, and natural gas and gasoline for spark-ignition engine simulations. *International of Engine Research*, 18(9):951–970, 2017.

[28] Ö. L. Gülder. Correlations of laminar combustion data for alternative s.i. engine fuels. *SAE Technical Paper 841000*, 1984.

[29] G. Z. Damköhler. Influence of turbulence on flame velocity in gaseous mixtures. *ZH Electrochem*, 46:601–626, 1940. (English translation, NACA TM 1112, 1947).

[30] P. Clavin and F. A. Williams. Theory of premixed-flame propagation in large-scale turbulence. *Joural of Fluid Mechanics*, 90(3):589–604, 1979.

[31] S. B. Pope and M. S. Anand. Flamelet and distributed combustion in premixed turbulent flames. *Symposium (International) on Combustion*, 20(1):403–410, 1985.

[32] Ö. L. Gülder. Turbulent premixed flame propagation models for different combustion regimes. *Symposium (International) on Combustion*, 23(1):743–750, 1990.

[33] R. Borghi. On the structure and morphology of turbulent premixed flames. *Recent Adv in the Aerosp Sci*, pages 117–138, 1985.

[34] N. Peters. Laminar flamelet concepts in turbulent combustion. *Symposium (International) on Combustion*, 21:1231–1250, 1986.

[35] F. A. Williams. Turbulent combustion. In J. Buckmaster, editor, *The Mathematics of Combustion*, chapter 3, pages 97–131. SIAM, 1985.

[36] N. Peters. The turbulent burning velocity for large-scale and small-scale turbulence. *Journal of Fluid Mechanics*, 384:107–132, 1999.

[37] H. G. Weller. The development of a new flame area combustion model using conditional averaging. Thermo-fluids section report **TF**/9307, Imperial College of Science, Technology and Medicine, 1993.

[38] B. F. Magnussen and B. H. Hjertager. On the mathematical modelling of turbulent combustion with special emphasis on soot formation and combustion. *Symposium (International) on combustion*, 16(1):719–729, 1976.

[39] I. S. Ertesvåg and B. F. Magnussen. The eddy dissipation turbulence energy cascade model. *Combustion Science and Technology*, 159(1–6):213–235, 2000.

[40] D. Bjerketvedt, J. R. Bakke, and K. V. Wingerden. Gas explosion handbook. *Journal of Hazardous Materials*, 52(1):1–150, 1997.

[41] B. E. Vembe, K. E. Rian, and K. Opstad. $KFX^{TM} - EXSIM$ *User Manual*. Trondheim, Norway, 2017.

[42] A. T. Mekonnen. Modelling and numerical simulation of gas explosions for industrial safety analyses. Project work, Norwegian University of Science and Technology, NTNU, 2018.

[43] B. H. Hjertager. Numerical simulation of flame and pressure development in gas explosions. *Studies Series - University of Waterloo, Solid Mechanics Division, SM Study*, 16:407–426, 1982.

[44] W. P. M. Mercx, A. C. Van den Berg, and Y. Mouilleau. Modelling and experimental research into gas explosions. *Overall report of the MERGE project, CEC contract: STEP-CT-0111 (SSMA)*, 1994.

[45] S. V. Patankar and D. B. Spalding. A calculation procedure for the transient and steady-state behavior of shell-and-tube heat exchangers. *Heat exchangers: design and theory sourcebook*, 1:155–176, 1974.

[46] W. T. Sha, C. I. Yang, T. T. Kao, and S. M. Cho. Multi-dimensional numerical modeling of heat exchangers. *Journal of Heat Transfer*, 104(3):417–425, 1982.

[47] B. H. Hjertager, T. Solberg, and K. O. Nymoen. Computer modelling of gas explosion propagation in offshore modules. *Journal of Loss Prevention in the Process Industries*, 5(3):165–174, 1992.

[48] H. K. Versteeg and W. Malalasekera. *An introduction to computational fluid dynamics: The finite volume method*. Pearson Education, Harlow, England, second edition, 2007.

[49] S. V. Patankar and D. B. Spalding. A calculation procedure for heat, mass, and momentum transfer in three dimensional parabolic flows. *International Journal of Heat and Mass Transfer*, 15(10):1787–1806, 1972.

[50] B. H. Hjertager. Simulation of transient compressible turbulent reactive flows. *Combustion Science and Technology*, 27(5–6):159–170, 1982.

[51] C. J. Greenshields. `OpenFOAM` *User Guide version 6. OpenFOAM Foundation Ltd*, 10th July 2018.

[52] P. K. Sweby. High resolution schemes using flux limiters for hyperbolic conservation laws. *SIAM J. Numer. Anal*, 21(5):995–1011, 1984.

[53] `https://www.hpc.ntnu.no/display/hpc/About+Vilje`, 2019. [accessed 21-May-2019].

Appendix A

Some pictures from Simulation Cases 1 and 3.

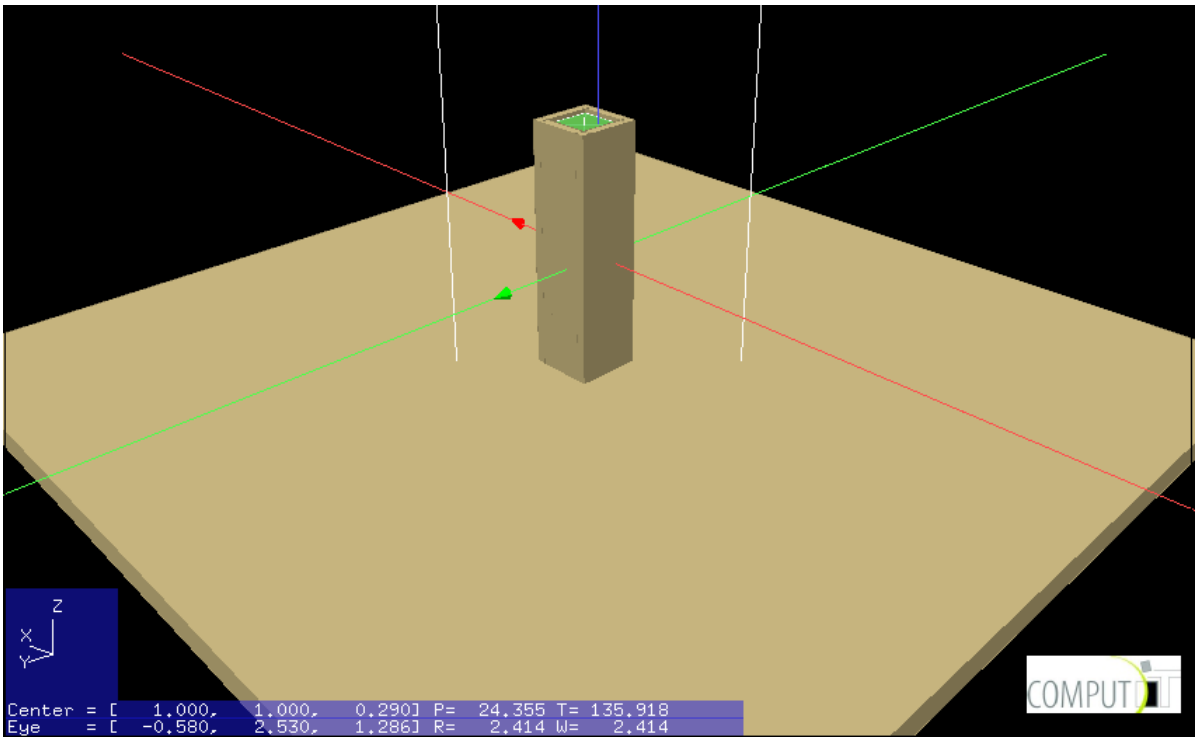

Figure A.1: closer view of the duct geometry including the ground for Simulation Case 1.

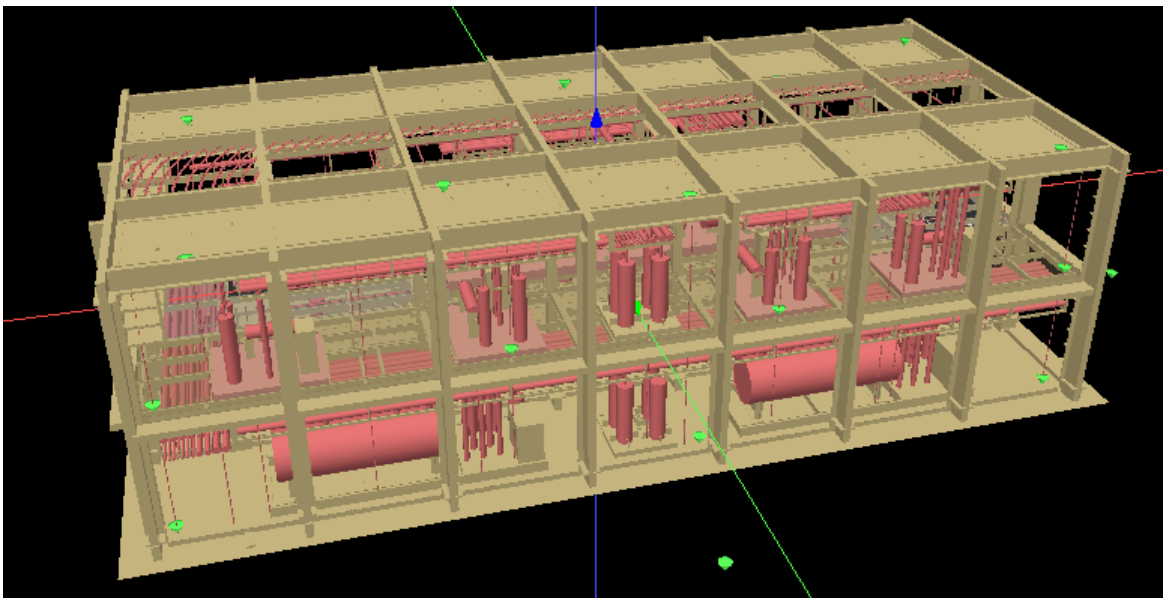

Figure A.2: View of the geometry of the test rig including some of the internal pressure transducers. The green cones show the location of the pressure transducer.

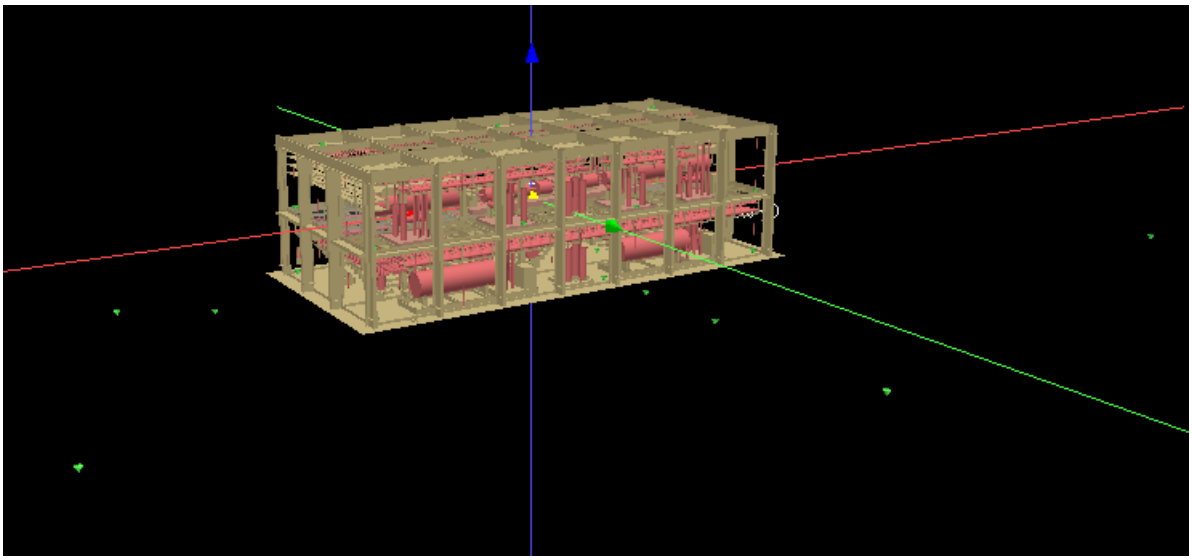

Figure A.3: View of the geometry of the test rig including some of the external pressure transducers. The green cones show the location of the pressure transducer.